

Thermodynamic and kinetic unfolding characterization of
therapeutic monoclonal antibodies using thermal analytics

Dissertation

zur Erlangung des Doktorgrades der Naturwissenschaften

(Dr. rer. nat.)

der

Naturwissenschaftlichen Fakultät II
Chemie, Physik und Mathematik

der Martin-Luther-Universität
Halle-Wittenberg

vorgelegt von

Herrn Richard Melien

geb. am 27.07.1990 in Fulda

Gutachter: Prof. Dr. Dariush Hinderberger
Prof. Dr. Patrick Garidel
Prof. Dr. Heiko Heerklotz

Datum der Verteidigung: 11.06.2021

Meiner Frau gewidmet

Eigenständigkeitserklärung

Hiermit erkläre ich, dass die vorliegende Arbeit selbständig und ohne fremde Hilfe verfasst, andere als die von mir angegebenen Quellen und Hilfsmittel nicht benutzt und die den benutzten Werken wörtlich oder inhaltlich entnommenen Stellen als solche kenntlich gemacht wurden.

(Ort, Datum)

(Unterschrift)

Table of content

Vorwort	1
Zusammenfassung	2
Abstract	4
Index of abbreviations	5
Chapter I – Introduction	7
1.1 Challenges in biopharmaceutical development	7
1.2 Aim of this study	8
Chapter II – Theory	9
2.1 Thermodynamics	9
2.2 Kinetics	10
2.3 Fluorescence spectroscopy	11
2.4 Differential scanning calorimetry	13
2.5 Classification and structure of monoclonal antibodies	13
Chapter III – Thermodynamic profiling	15
3.1 Abstract	15
3.2 Introduction	16
3.3 Material and methods	17
3.4 Results and discussion	23
3.5 Conclusion	38
Chapter IV – Kinetic profiling	40
4.1 Abstract	40
4.2 Introduction	41
4.3 Material and methods	43
4.4 Results	48
4.5 Discussion	66
4.6 Conclusion	71
Chapter V – Fab assignment	72
5.1 Abstract	72
5.2 Introduction	73
5.3 Material and methods	74
5.4 Results	75

5.5 Discussion	85
5.6 Conclusion	87
Chapter VI – Concluding remarks	89
6.1 Conclusion	89
6.2 Outlook	90
Chapter VII – Bibliography	92
7.1 Danksagungen	92
7.2 References	93
7.3 List of figures	98
7.4 List of tables	100
Appendix	101
Appendix of Chapter III	101
A.3.4 Results and discussion	101
Subtopic – Comparison of additional IF vs. DSC thermodynamics	104
Appendix of Chapter IV	107
A.4.3 Material and methods	107
A.4.4 Results	108
Appendix of Chapter V	140
A.5.4 Results	140
Lebenslauf	146

Vorwort

Die vorliegende Dissertationsschrift ist aufgeteilt in sechs eigenständige Kapitel. Die nachfolgende Arbeit ist in englischer Sprache verfasst, wobei auch eine Zusammenfassung der gesamten Arbeit in Deutsch geschrieben wurde. Im ersten Kapitel wird das Thema der Arbeit im Allgemeinen eingeleitet. Im zweiten Kapitel werden die Theorie und der Hintergrund rund um die wichtigsten Ansätze und Methoden der Arbeit kurz beschrieben. In den Kapiteln III bis V sind die drei Hauptteile der Arbeit zu finden. Diese sind jeweils als eigenständige Studien aufgebaut mit Zusammenfassung, Einleitung, Material und Methoden, Ergebnissen, Diskussion und Schlussfolgerung. Abschließend folgt eine Schlussfolgerung über die gesamte Arbeit und ein Ausblick. Der beschriebene Aufbau soll es dem Leser ermöglichen, gezielt einzelne Themengebiete lesen zu können und sich so eine bessere Übersicht zu verschaffen. Dies ist vor allem wichtig, wenn die vorliegende Dissertationsschrift herangezogen wird, um bestimmte einzelne Methoden und Theorien für die pharmazeutische Entwicklung zu nutzen und anzuwenden. Die nachfolgende Arbeit dient dem Zweck verschiedene prädiktive Parameter für thermische Stabilität von therapeutischen Antikörpern zu entwickeln, testen und bewerten. Dies soll es der pharmazeutischen Entwicklung ermöglichen schnell und gezielt die stabilsten Antikörper zu selektieren, um nur diese in weiteren zeitaufwendigeren Studien zu charakterisieren.

Zusammenfassung

Die komplexe Struktur eines therapeutischen monoklonalen Antikörpers (mAb) macht diesen anfällig für verschiedene physikalische und chemische Einflüsse, sodass der Antikörper seine pharmakologisch aktive Form verlieren kann. Zusätzlich kann es zur Partikelbildung kommen, welche ungewollte Immunreaktionen im Patienten auslösen können. Aus diesem Grund beschäftigt sich die vorliegende Arbeit mit der thermischen Stabilität von Antikörpern und deren Vorhersage. Dabei sollen die thermodynamischen und kinetischen Eigenschaften der Proteinentfaltung untersucht und beschrieben werden, um thermisch stabile Antikörper zu identifizieren. In dieser Studie werden van't Hoff Enthalpien (ΔH_{vh}) und Aktivierungsenergien (E_a) von Entfaltungsübergängen therapeutischer Antikörper bestimmt und diese mit etablierten Stabilitätsparametern wie Schmelztemperaturen (T_m) verglichen, um die prädiktive Aussagekraft der Parameter hinsichtlich thermischer Antikörperstabilitäten, ermittelt über Größenausschlusschromatographie (SEC), zu evaluieren. Dazu werden die intrinsische Fluoreszenz (IF) der Antikörper in Abhängigkeit der Temperatur aufgenommen und aus den jeweiligen Entfaltungsprofilen thermodynamische und kinetische Parameter mittels zweier verschiedener scheinbarer Drei-Zustands-Modelle bestimmt. Als prädiktiven Parameter, welcher die höchste Korrelation zu thermischer Stabilität von Antikörpern zeigt, wurde in dieser Studie die Aktivierungsenergie des Entfaltungsübergangs der CH₂-Domänen gefunden, wobei auch zu anderen prädiktiven Parametern wie Enthalpien und Schmelztemperaturen Korrelationen gefunden werden können. Im Vergleich zur Fluoreszenzmessung wurden thermodynamische Parameter auch direkt über Differenz-Scanning-Kalorimetrie (DSC) bestimmt und diese mit den aus den indirekten Fluoreszenzmessungen verglichen. Die mit den zwei unterschiedlichen Methoden bestimmten Enthalpien besitzen ähnliche Werte. Neben der direkten Bestimmung von Enthalpien wurden mit Hilfe von Kalorimetrie die verschiedenen Entfaltungsübergänge eines Antikörpers in den Fluoreszenzthermogrammen identifiziert. Zusätzlich wurden in dieser Arbeit zwei neue Methoden entwickelt, um Entfaltungsübergänge auch ohne kalorimetrische Messungen zuordnen zu können. Diese zwei neuen Methoden basieren auf der Auswertung der ersten Ableitung der jeweiligen Fluoreszenzthermogramme. Während bei der ersten Methode der Entfaltungsübergang des Antigen-bindenden Fragments (Fab) des Antikörpers das Signal mit der größten Asymmetrie der Signalform zeigt, wird

bei der zweiten Methode das Fab als das Signal identifiziert, welches den größten Anstieg der Amplitude bei ansteigenden Heizraten zeigt. Zusammenfassend lässt sich festhalten, dass die vorliegende Studie aufzeigt, welche prädiktiven Parameter für die thermische Stabilität von therapeutischen Antikörpern von den vorgestellten Methoden am besten geeignet sind. Zudem liefert die Studie Methoden, um die prädiktiven Parameter hinsichtlich der Antikörperstruktur bewerten und vergleichen zu können.

Abstract

Due to the complex structure of a therapeutic monoclonal antibody (mAb), the active conformation tends to degrade under stress conditions, which can lead to a loss of its therapeutic effect or even worse to the formation of particles. A high particle load can again lead to an unwanted immune response of the patient. For this purpose, the present study deals with the analysis of thermodynamics and kinetics of mAb unfolding in solution to estimate their thermal stability. Therefore, parameters like van't Hoff enthalpies (ΔH_{vh}) and activation energies (E_a) were tested to correlate with thermal stability analyzed by size exclusion chromatography (SEC) to investigate their predictive character. The newly evaluated predictive parameters were compared to commonly used parameters such as melting temperatures (T_m) to assess their capability to improve thermal stability prediction. For this purpose, temperature dependent intrinsic fluorescence (IF) thermograms were recorded and values of ΔH_{vh} and E_a were determined by applying appropriate fit functions based on two different apparent three-state models. As a comparative method and to interpret IF thermograms regarding the mAb domains involved in the unfolding transitions, differential scanning calorimetry (DSC) was performed. It is found that thermodynamic parameters derived from IF and DSC show similar values. For thermal stability prediction, E_a of the CH₂-domain is investigated to show strongest correlation with thermal stability. However, correlations can also be found for ΔH_{vh} and T_m values. Regarding the possibility of using DSC to assign unfolding transitions to certain mAb domains, two novel methods were developed and tested to assign transitions directly from IF thermograms without the need of DSC. Both methods are based on the analysis of the first derivative IF thermogram. The first method analyzes the asymmetry of the unfolding transition and assigns the antigen-binding fragment (Fab) unfolding to the most asymmetric signal. The second method determines the Fab transition to the signal showing the largest increase in the amplitude by performing IF experiments with ascending heating rates. In summary, this study introduces predictive parameters for thermal mAb stability and demonstrates possibilities to compare the parameters regarding the structural components of the mAb.

Index of abbreviations

α	degree of conversion
ΔC_p	change of heat capacity
ΔG	change of Gibbs energy
ΔH_{cal}	change of calorimetric enthalpy
ΔH_{vh}	change of van 't Hoff enthalpy
ΔS	change of entropy
A	frequency factor
ANOVA	analysis of variance
A_r	solution of the Arrhenius integral
ASF	Asymmetry Factor
B	heating rate
c	intercept of the irreversible three-state model
c.u.	cooperative unit
c_a	concentration of a
CH-domain	constant antibody domain of the heavy chain
CHO	Chinese hamster ovary
C_{p,T_m}	heat capacity of the melting temperature
D ₁	first denatured state
D ₂	second denatured state
DSC	differential scanning calorimetry
E	energy
E_a	activation energy
E_{kin}	kinetic energy
E_{pot}	potential energy
E_U	internal energy
F	folded state
f	state fraction
Fab	fragment antigen binding
Fc	fragment crystallizable
FE ₃₃₀	fluorescence emission at 330 nm
FE ₃₅₀	fluorescence emission at 350 nm

HP/UP-SEC	high performance / ultra performance size exclusion chromatography
I	intermediate state
IF	intrinsic fluorescence
IgG1	immunoglobulin type G isotype 1
K	equilibrium constant
LENP	Lumry-Eyring nucleated polymerization
m	linear slope of the irreversible three-state model
mAb	monoclonal antibody
mAU	milli arbitrary unit
MWCO	molecular weight cut-off
n	reaction order
NES	Novel Experimental Setup
p	pressure
Q	heat
R	gas constant
S	slope of the reversible three-state model
SEC	size exclusion chromatography
T	temperature
t	time
T _{agg}	aggregation onset temperature
t _{agg}	aggregation onset time
T _m	melting temperature
U	unfolded state
V	volume
W	thermodynamic work
y	signals of the IF thermograms
Y	single state signals
Y ₀	intercept of the reversible three-state model

Chapter I – Introduction

1.1 Challenges in biopharmaceutical development

In biopharmaceutical development, manufacturing, and storage of monoclonal antibodies (mAbs), challenges arise due to their tendency to degrade [1, 2]. The degradation of the intact, active structure of a mAb can lead to a reduced or non-therapeutic effect of the molecule or even worse to unwanted immune response due to the formation of insoluble aggregates and larger particles [3, 4]. The prevention of the mAb formulation for fast degradation is a major challenge for biopharmaceutical development [5]. Challenges can arise from two sides: first, complex and manifold mAb degradation mechanisms [6] and second, various methods to characterize mAb stability and degradation [7]. To only give a short overview, protein degradation can arise from unfolding and subsequent aggregation [8, 9], from fragmentation [10, 11], or degradation caused by high protein concentrations [12]. Methods and their limitations e.g. size exclusion chromatography (SEC), dynamic light scattering, temperature dependent unfolding experiments (differential scanning calorimetry (DSC), circular dichroism and fluorescence spectroscopy), and particle tracking methods such as light obscuration and micro flow imaging, are summarized in various publications [7, 13-16].

Strategies for prediction and prevention of protein degradation

Improvements of protein stability might be achieved using different buffers and excipients such as salts, sugars, amino acids, and surfactants [1, 17]. To characterize and predict stability of different proteins and formulations, several experimental approaches are commonly applied. E.g., characterization of thermal stability is often associated with recording melting temperatures (T_m) in DSC experiments [13, 18] or by fluorescence measurements [15, 19, 20]. Instead of increasing the temperature, an isothermal unfolding profile can be investigated by increasing the amount of chaotropic salts [20, 21]. Another approach to improve protein properties early in development is the use of *in-silico* methods to identify chemical modification sites, statistically unlikely amino acids, or sequence motifs for intermolecular cross-beta-sheets based on their

primary sequence of the polypeptide chain. Hence, rational sequence design can be employed to avoid such known motifs [22]. *In-silico* approaches were successfully used to improve protein properties, which allowed for concurrently diminishing protein aggregation by identification and reducing of aggregation-prone regions [23, 24]. Due to the complex mAb degradation mechanisms and limitation of detection methods, the biopharmaceutical development, especially the characterization of mAb stability, remains challenging. Therefore, the development of mAbs requires suitable methods describing their stability to develop a drug with a high amount of therapeutic active molecules ensuring patient safety.

1.2 Aim of this study

As mentioned above, biopharmaceuticals such as liquid formulated mAb formulations tend to degrade, which can lead to a loss of functionality and may compromise drug safety. Therefore, one main challenge in the development of biopharmaceutical drugs is to develop molecules and formulations that have a high intrinsic stability against various physical and chemical impacts leading to drug degradation. To contribute to this research field, this study aims to investigate thermal stability of liquid formulated therapeutic mAbs. Thus, temperature dependent unfolding experiments were performed to determine thermodynamic and kinetic parameters from unfolding transitions. These parameters will be tested to predict thermal stability of various mAb formulations. Therefore, intrinsic fluorescence (IF) spectroscopy and DSC will be used to investigate temperature dependent unfolding of mAbs. Moreover, this study will also focus on the different transitions appearing in an unfolding thermogram of a mAb. These transitions will be assigned to structural regions of the mAb. The goal will be to find parameters of the transitions that predict thermal stability of the mAbs.

Chapter II - Theory

2.1 Thermodynamics

The theory of thermodynamics describes the macroscopic physical properties of matter and chemical equilibria and can be used to describe energy changes of chemical reactions [25]. A central assumption in the theory of thermodynamics is that the energy of an isolated system is constant and this assumption constitutes the first fundamental law of thermodynamics [25]. The energy of a system (E) is constituted of the kinetic energy (E_{kin}), the potential energy (E_{pot}) and the internal energy (E_U) and can be described by Eq. 2.1 [25]:

$$E = E_{kin} + E_{pot} + E_U \quad (2.1).$$

For a constant E_{kin} and E_{pot} , the internal energy of an isolated system is constant. The internal energy can change if the system exchanges heat (Q) with its environment or if the system does thermodynamic work (W) or it is done to the system. This can be described by Eq. 2.2, which is also a commonly used expression for the first fundamental law of thermodynamics [25]:

$$\Delta E_U = Q + W \quad (2.2).$$

For pressure-volume work only, Eq. 2.2 can be expressed for very small changes as follows (Eq. 2.3) [25]:

$$dE_U = dQ - pdV \quad (2.3)$$

where the product of pressure (p) and volume (V) represents thermodynamic work.

An important thermodynamic parameter to describe chemical reactions is the enthalpy (H) which is defined as follows (Eq. 2.4) [25]:

$$H = E_U + pV \quad (2.4).$$

For enthalpy changes, Eq. 2.4 can be expressed by its differential (Eq. 2.5) [25]:

$$dH = dE_U + pdV + Vdp \quad (2.5).$$

By substituting dE_U in Eq. 2.5 with Eq. 2.3, dH can be expressed by Eq. 2.6 [25]:

$$dH = dQ + Vdp \quad (2.6).$$

Eq. 2.6 illustrates the meaning of the enthalpy, that for chemical reactions under constant pressure ($dp=0$), the enthalpy change is equal to the exchange of heat between the system and its environment [25]. The enthalpy change can also be expressed by its total differential dependent on the temperature (T) and pressure as [25]:

$$dH = \left(\frac{\delta H}{\delta T}\right)_p dT + \left(\frac{\delta H}{\delta p}\right)_T dp \quad (2.7).$$

In Eq. 2.7, $(\delta H/\delta p)_T$ is zero assuming no interaction between the molecules for an ideal gas, while the term $(\delta H/\delta T)_p$ is commonly expressed as heat capacity (c_p), so that the enthalpy change can be written as [25]:

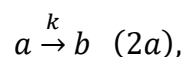
$$dH = c_p dT \quad (2.8).$$

Eq. 2.8 illustrates that the enthalpy change can be determined from the heat capacity and the change in temperature of the isolated system under constant pressure.

The first fundamental law of thermodynamics describes the changes of the internal energy dependent on heat and thermodynamic work (Eq. 2.2). Therefore, according to the first fundamental law of thermodynamics, thermodynamic work can be arbitrarily converted to heat and vice versa [25]. However, this cannot be observed in nature. The direction of a reaction is defined by the second fundamental law of thermodynamics, which introduces the entropy as a thermodynamic parameter. This law states that for an isolated system the entropy can only increase or stays constant [25].

2.2 Kinetics

Reaction kinetics deals with the rate, order and the mechanism of a chemical reaction [25]. Chemical reactions can be classified into different reaction orders such as zeroth order, first order, second order, or third order dependent on the number of molecules involved and the concentration dependence of the reaction. A first order reaction, which is relevant for this study, can be written as follows (Eq. 2a):



while the rate constant (k) can be described by Eq. 2.9 [25]:

$$-\frac{dc_a}{dt} = k \cdot c_a \quad (2.9).$$

Dependent on the start concentration (c_{a0}), the time (t), and the rate constant, c_a can be written by Eq. 2.10 [25]:

$$c_a = c_{a0} \cdot e^{-kt} \quad (2.10).$$

For most chemical reactions, the velocity of the reaction increases exponentially with increasing temperature [25]. Arrhenius and van't Hoff found that the temperature dependence of the rate constant k can be described by Eq. 2.11 [25]:

$$k = A \cdot e^{-\frac{E_a}{RT}} \quad (2.11)$$

where A is the preexponential factor, which is treated as temperature independent. R is the gas constant, while E_a is the activation energy, which is needed for the educts to react [25].

2.3 Fluorescence spectroscopy

Spectroscopy is an analytical method, which is based on interactions between a sample and electromagnetic radiation [26]. Depending on the wavelength of the radiation, different spectroscopic methods can be distinguished such as infrared (IR), UV/Vis and fluorescence spectroscopy to mention only a few. A main spectroscopic method in this study is fluorescence spectroscopy and its theory is briefly described in this section.

Fluorescence spectroscopic measurements are based on electromagnetic radiation, which excites a sample at a certain wavelength. The molecules of the sample are in an excited state and emit radiation by falling to their ground state. The emitted radiation has a longer wavelength than the absorbed wavelength so that the fluorescence spectrum is shifted towards longer wavelengths compared to the absorption spectrum [25]. This correlation was first observed by Sir. G. G. Stokes at the University of Cambridge in 1852 and the phenomenon is therefore known as "Stokes Shift" [27]. Typical characteristics of a fluorescence emission spectrum are its independence of

the excitation wavelength (exceptions are known), the fluorescence lifetime (generally about 10 ns), and the quantum yield [27].

Investigations of protein unfolding including mAbs are often performed by using IF spectroscopy [27]. Three of the 20 amino acids appearing in the amino acid sequence of proteins are fluorescent: phenylalanine, tyrosine, and tryptophan. The latter is the most dominant regarding the quantum yield of fluorescence emission [27]. The fluorescence emission of tryptophan is highly dependent on the polarity of its local environment so that conformational changes such as protein unfolding can be tracked [27].

The dependence of the fluorophores on the polarity of their local environment has therefore been used to investigate protein unfolding by detecting two different fluorescence emission wavelengths [15, 16]. This principle is also used by the fluorescence instruments used in this study to investigate temperature dependent protein unfolding. The instruments measure the intensity of two different fluorescence emission wavelengths illustrated in Fig. 2.1, which represent the fluorophores in a hydrophilic environment (emission maximum at about 350 nm) and in a hydrophobic environment (emission maximum at about 330 nm).

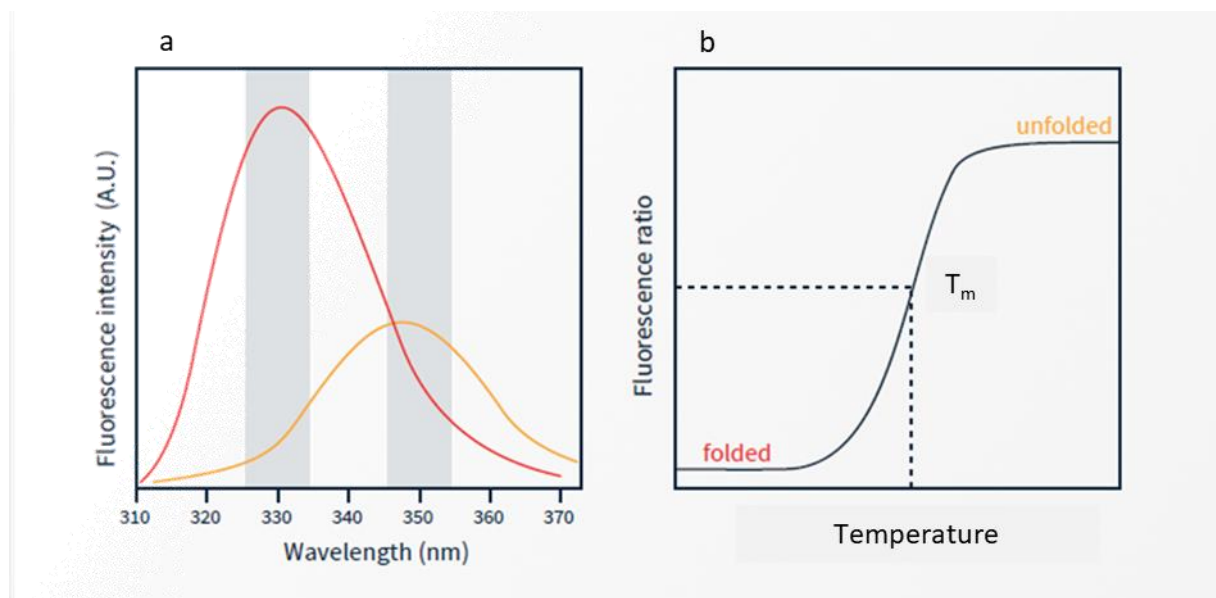


Fig. 2.1: Intrinsic fluorescence emission maxima of a protein. (a) Fluorescent amino acids like tryptophan or tyrosine in the protein sequence show an emission maximum at 330 nm in a hydrophobic environment (represents the folded protein state) and an emission maximum at 350 nm in a hydrophilic environment (represents the unfolded protein state). (b) By plotting the ratio of both wavelength (350 nm / 330 nm) against the temperature, the depicted protein unfolding profile can be obtained. The transition midpoint represents the apparent melting temperature (T_m). Adapted and modified from [28].

The fluorescence emission shifts from 330 nm to 350 nm during protein unfolding (Fig. 2.1). This fact can be interpreted that the nonpolar fluorophore amino acids of the protein, present in the nonpolar hydrophobic protein core, are exposed to a polar hydrophilic environment during unfolding. The change of the environment of the nonpolar fluorophores can be interpreted of a transition from a folded protein state (330 nm) to an unfolded protein state (350 nm) [21]. By plotting the ratio of both fluorescence emission wavelengths against the temperature, an unfolding profile of a protein can be obtained (illustrated in Fig. 2.1b).

2.4 Differential scanning calorimetry (DSC)

DSC can be used to detect enthalpy changes during transformation reactions [25]. Therefore, DSC can be applied to study temperature dependent protein unfolding. DSC is based on the principle that the temperature of a sample and a reference substance is kept constant during the measurement [25]. During transformation of a folded protein state to an unfolded one, the proteins need energy (endothermic processes). During transformation, more energy is required to heat the sample chamber to the same temperature than for heating the reference chamber. The difference in energy serves as a detection signal. By analyzing proteins, the detection signal is interpreted to indicate the unfolding transition from a folded to an unfolded protein state with ascending temperatures [29, 30].

2.5 Classification and structure of monoclonal antibodies

Immunoglobulins (Ig) are divided into five classes – IgM, IgG, IgA, IgD, and IgE – differing in the constant region of the heavy amino acid chain [31]. IgG is most relevant for pharmaceutical application [32] and can be divided into four subclasses (1 to 4), whereas IgG1 has the largest amount in human blood [33, 34] and is the relevant type of molecule for this study. The y-shaped structure of an IgG1 molecule is composed of two identical heavy amino acid chains and two identical light amino acid chains connected by disulfide bonds [35]. The amino acid chains are composed of four different constant domains (CH₁, CH₂, CH₃, and CL) and two variable domains (VH and VL) illustrated in Fig. 2.2.

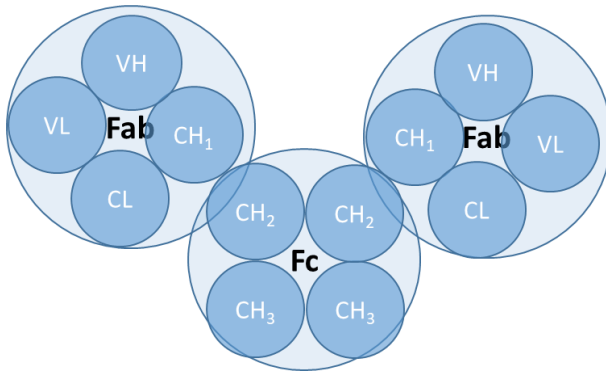


Fig. 2.2: Schematic structure and domains of an IgG1. The y-shaped structure of an IgG1 molecule is composed of two antigen binding fragments (Fab) and one crystallizable fragment (Fc). These fragments are composed of different variable and constant domains of the heavy (VH and CH-domains) and light amino acid chain (VL and CL-domains).

The different regions of an IgG1 molecule can also be classified by their biologic function. The antibody can be divided into two different regions, the antigen binding fragment (Fab) and the crystallizable fragment (Fc). The Fab region specifically binds to its antigen causing the biologic and the therapeutic effect of an IgG1 molecule, while the Fc region of the antibody is important for the conjunction to effector functions [31].

Chapter III – Thermodynamic profiling

The content of this chapter is reused with permission of Springer Nature and has already been published by Richard Melien, Patrick Garidel, Dariush Hinderberger, Michaela Blech [36].

Author contributions

R. Melien designed and M. Blech designed and supervised the study. Experimental research, data analysis, and evaluation was performed by R. Melien. All authors contributed to the data analysis. The first draft was written by R. Melien and was reviewed by P. Garidel, D. Hinderberger, and M. Blech.

3.1 Abstract

Purpose: Predicting thermal protein stability is of major interest in the development of protein-based biopharmaceuticals. Therefore, this study provides a predictive tool for determining transition enthalpies, which can be used for ranking different proteins according to their thermal stability.

Methods: Unfolding and aggregation profiles of eight different therapeutic monoclonal antibodies (mAbs) of type G, isotype 1 were investigated. The unfolding profiles were determined by intrinsic fluorescence (IF) spectroscopy and differential scanning calorimetry (DSC). A reversible three-state unfolding fitting model was used to determine thermodynamic parameters for macromolecular multi-domain mAbs in IF experiments, like the van 't Hoff enthalpy change (ΔH_{vh}) and the entropy change (ΔS) of the unfolding event. The derived values were compared to thermodynamic parameters obtained directly by calorimetry. Moreover, differences in the Fab enthalpies were used to predict aggregation behavior and protein thermal stability. To do so, the liquid-formulated mAbs were investigated exemplarily by size exclusion chromatography (SEC) after accelerated thermally induced stress conditions.

Results: Comparing the thermodynamic parameters derived from IF spectroscopy and DSC result in similar values. Data generated by thermally induced stress at 40 °C show similar stability ranking as postulated through the Fab enthalpies for mAbs in two

different formulations, while at 25 °C a meaningful ranking is not possible, because distinct differences in the thermal stability cannot be observed. The ranking according to the Fab enthalpies to describe the 40 °C SEC ranking seems to be more reliable compared to the use of melting temperatures (T_m) or aggregation onset temperatures (T_{agg}) and times (t_{agg}).

Conclusion: It is shown that thermodynamic profiling can help predicting unfolding and aggregation properties of therapeutic mAbs at 40 °C. Therefore, analyzing thermodynamic unfolding parameters is a useful and supportive tool discriminating thermal stability profiles of mAbs for further pharmaceutical development and clinical studies.

3.2 Introduction

During development of protein-based drugs, the prevention of particle formation resulting from protein aggregation is of crucial interest. Protein aggregates exhibit reduced or no biologic activity through loss of their intact, active structure. Hence, reducing and especially avoiding the formation of protein aggregates during manufacturing, purification, formulation, and storage of therapeutic protein products is of major concern, especially to avoid unwanted immune response for patients [3, 4, 14, 37].

Protein unfolding

The functional, intact conformation of a monoclonal antibody (mAb) is dependent on the molecule's three-dimensional structure. Besides its primary sequence, the structure of a mAb is composed of noncovalent interactions like hydrogen bonds, electrostatic interactions, hydrophobic contributions and covalent disulfide bonds [38]. However, during protein unfolding, these bonds can break and the equilibrium shifts from the folded to the unfolded state with a plethora of potential partially unfolded states. Dependent on the number of transitions, the unfolding process of a protein is often described in a first assumption by a two-state [39] or a three-state model [40, 41]. In the two-state model, the protein can exist in the folded and unfolded state, and the equilibrium within these two states depends on the respective temperature. In contrast,

the three-state unfolding model postulates an intermediate state during the unfolding process, and experimental unfolding profiles of mAbs often fall into this category and show two transitions [41]. In this case, the unfolding reaction is described by two equilibria: between the folded and the intermediate state and between the intermediate and the unfolded state, respectively [41]. Dependent on the apparent number of transitions, both models are used to describe the unfolding process as triggered by increasing temperature or chemical denaturation with chaotropic reagents [39, 41-44]. Another model based on the Zimm-Bragg theory, describing a helix-to-coil transition in polypeptides [45], postulates protein unfolding as a sequential, multistate process [46]. This model has recently been used to study protein unfolding [46, 47] and has been further applied to describe the thermal unfolding of a mAb [48].

In this chapter, the thermal unfolding processes of eight therapeutic mAbs are described to derive thermodynamic parameters of the unfolding process from a three-state fitting model using intrinsic fluorescence (IF) spectroscopy. The use of IF has two main advantages: (i) it can be run as a high throughput assay and (ii) the sample volume needed is in the range of a few microliters [19, 20, 49]. A reversible three-state model is used to describe and determine thermodynamics of the two experimentally observed unfolding transitions resulting in three apparent protein states for the mAbs. The determined thermodynamics from the three-state model are further compared to thermodynamic parameters derived from differential scanning calorimetry (DSC). In a second step, those thermodynamic parameters are tested for prediction of mAb thermal stability compared to commonly used predictive parameters. Understanding the energetic changes of the dynamic processes of the folding and unfolding equilibrium of the protein could help to support prediction and rank mAbs according to their thermal stability.

3.3 Material and methods

Antibodies

The used mAbs were provided by Boehringer Ingelheim Pharma GmbH & Co. KG (Biberach, Germany). mAb1 to mAb1e are type G, isotype 1 immunoglobulins (IgG1) and originate from one parent sequence, differing only in a maximum of six amino acids in the Fab region. Information of the six variants and their processing has been

reported in [22], where mAb1 refers to mAb1_Hv1_LWT, mAb1a to mAb1_Hv2_LWT, mAb1b to mAb1_Hv2_Lv3, mAb1c to mAb1_HWT_Lv1, mAb1d to mAb1_HWT_Lv2, and mAb1e to mAb1_HWT_Lv3. mAb2 and mAb3 are unrelated different IgG1 antibodies and were expressed by Chinese hamster ovary (CHO) cells and purified with several chromatography steps, including protein A and ion chromatography as described by Bergemann et al. [50].

Sample preparation

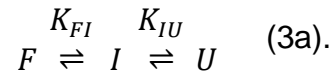
The mAbs in this chapter were formulated into either 10 mM sodium phosphate, 10 mM sodium chloride, pH 6.5 buffer, which is referred to as phosphate buffer or in 25 mM sodium citrate, 125 mM sodium chloride, pH 6.0 buffer, which will be further referred to as citrate buffer. mAb1 to mAb1e were formulated in citrate buffer, while mAb2 and mAb3 were formulated in phosphate buffer. The mAbs were transferred in the respective buffers by dialysis using 20 kDa molecular weight cut-off (MWCO) dialysis cassettes at room temperature (Slide-A-Lyzer™, Thermo Fisher Scientific Inc., Waltham, USA). Afterwards, the mAb solutions were concentrated at 5000 g and 20 °C to different concentrations using 30 kDa MWCO centrifugal filters (Amicon® Ultra-15, Merck Millipore Ltd., Burlington, USA) or diluted with the respective buffer generating samples with smaller protein concentrations. Protein concentrations were determined by UV/Vis absorbance measurements at a wavelength of 280 nm using a UV/Vis Lambda 35 photo spectrometer (Perkin Elmer Inc., Waltham, USA).

Intrinsic fluorescence (IF) spectroscopy

IF spectroscopy can be used to investigate protein conformational stability [16]. IF measurements were performed with the Prometheus NT.48 – nanoDSF (NanoTemper Technologies GmbH, Munich, Germany). The device was used for thermal unfolding experiments. All measurements were performed in triplicates at a mAb concentration of 1 mg·ml⁻¹ using standard glass capillaries (NanoTemper Technologies GmbH, Munich, Germany). For IF unfolding experiments, a start temperature of 20 °C and an end temperature of 95 °C with a heating rate of 1 K·min⁻¹ were chosen. The intensities of the fluorescence emission at 330 nm (FE₃₃₀) and 350 nm (FE₃₅₀) were recorded during the temperature ramp to track the population of folded and unfolded protein

states [15, 21]. For evaluation, the mean and standard deviation of a triplicate were determined and the FE_{350}/FE_{330} ratio was calculated and plotted as a function of temperature.

Since the respective experimental fluorescence thermograms clearly show two transitions, the measured fluorescence ratio was analyzed by fitting the resulting temperature dependent FE_{350}/FE_{330} -plot with an apparent reversible three-state unfolding model to derive thermodynamic parameters. The reversible three-state model was applied to characterize the folded/unfolded equilibrium of the two observed unfolding events of mAbs. Without making any assumptions on the structure of the three states, one can assume that during heating the equilibrium shifts from the folded (F, all domains are in the folded state) via an intermediate (I, folded and unfolded domains) to an unfolded state (U, all domains are in the unfolded state). This can be described by the following reaction (Eq. 3a):



As shown for chemical denaturation by Boehm et al. [41], the signals of the IF thermograms (y) can be described by the sum of the single state signals (Y_i) weighted with their state fractions (f_i) in equilibrium for the folded (F), intermediate (I), and unfolded (U) state:

$$y = f_F Y_F + f_I Y_I + f_U Y_U \quad (3.1).$$

In Eq. 3.1, every single state signal (Y_i) can be written by the following linear relation (Eq. 3.2) [41]:

$$Y_i = Y_{i0} + T \left(\frac{dY_i}{dT} \right) \quad (3.2).$$

Eq. 3.2 describes the single state signal through the initial signal of the state (Y_{i0}) and the temperature (T) dependent signal change. The fractions of the three different states in the reversible three-state unfolding model can be expressed by using the equations described in Boehm et al. [41]. Assuming that the system achieves thermodynamic equilibrium, Eq. 3.1 and 3.2 can be rewritten with the equilibrium constant (K_i) as Eq. 3.3:

$$y = \frac{Y_{F0} + S_F T}{1 + K_{FI}(1 + K_{IU})} + \frac{(Y_{I0} + S_I T) K_{FI}}{1 + K_{FI}(1 + K_{IU})} + \frac{(Y_{U0} + S_U T) K_{FI} K_{IU}}{1 + K_{FI}(1 + K_{IU})} \quad (3.3).$$

Eq. 3.3 describes the sigmoidal character of the IF thermogram of three states, where the curve is characterized by the initial state signals and the slopes of the signals (S_i) for the folded, intermediate, and unfolded state.

Investigations of thermodynamics can be achieved by expressing the equilibrium constant in Eq. 3.3 with the van't Hoff equation (Eq. 3.4):

$$K = \exp\left(-\frac{\Delta H_{vh}}{R}\left(\frac{1}{T} - \frac{1}{T_m}\right)\right) \quad (3.4)$$

where ΔH_{vh} is the van't Hoff enthalpy change at the melting temperature (T_m), at which 50 % of the protein domains are in the unfolded state, and R is the gas constant. For the evaluation of IF, the change in heat capacity (Δc_p) before and after transition was not considered, because Δc_p cannot be extracted from spectroscopic methods like IF [46]. However, the entropy change (ΔS) at the transition midpoint can simply be calculated from the determined enthalpy and the Gibbs energy change (ΔG) of the unfolding transition using Eq. 3.5:

$$\Delta S = \frac{\Delta H_{vh} - \Delta G}{T_m} \quad (3.5).$$

Eq. 3.3 was used to determine ΔH_{vh} and T_m by least-square fitting of IF thermograms using the software OriginPro 2017[®] (OriginLab Cooperation, Northampton, USA). To verify and compare the IF values, thermodynamic parameters were independently determined using DSC.

Differential scanning calorimetry (DSC)

DSC was used to determine thermodynamic parameters of the unfolding behavior of all mAbs in this chapter using an automated MicroCal PEAQ-DSC[®] (Differential scanning calorimeter, Malvern Instruments, Malvern, UK). Measurements were performed at a mAb concentration of 1 mg·ml⁻¹ analyzing unfolding from 25 °C to 95 °C. The heating rate was set to 1 K·min⁻¹. The thermogram of the respective buffer was subtracted from the sample thermogram. Due to the fact that the two transitions in the DSC thermograms are not fully separated and a baseline between the transitions cannot be detected, Δc_p can only be approximated over both transitions for the two unfolding events. To account for Δc_p by the determination of ΔH_{cal} , a baseline

subtraction was performed to obtain the DSC thermograms adjusting the baseline to zero.

In DSC thermograms, the enthalpy change (ΔH_{cal}) during the unfolding transition was determined by integrating the signal areas. Therefore, appropriate fit functions (Bigauss and PearsonVII) to determine the area under the DSC curve were applied to simulate the not fully separated DSC unfolding transitions (Fig. A.3.1, Appendix). The respective area of the fit function was determined to obtain ΔH_{cal} of the unfolding transition.

To compare calorimetric enthalpies analyzed by DSC to van't Hoff enthalpies determined by the three-state fit function plotting the IF unfolding traces, ΔH_{cal} can be transformed to give ΔH_{vh} for each transition using Eq. 3.6, as derived by Privalov and Potekhin [29]:

$$\Delta H_{vh} = \frac{(\sqrt{n+1})^2 RT_m^2 \left(c_{p,Tm} - \frac{\Delta c_p \sqrt{n}}{\sqrt{n+1}} \right)}{\Delta H_{cal}} \quad (3.6).$$

In Eq. 3.6, n describes the reaction order of the protein unfolding, which is 1 for each transition between two states [29]. $c_{p,Tm}$ is the heat capacity of the melting temperature and Δc_p is zero after baseline subtraction. ΔH_{vh} describes the theoretical enthalpy change derived from the van't Hoff equation between the two states for both transitions in the three-state model and is usually associated with the heat change of a single domain within the protein [51]. In contrast, ΔH_{cal} is the experimental enthalpy change, which represents the sum of effects like hydration, intermolecular interactions and especially the amount of additional transition states within in a single transition [29, 51, 52]. The ratio between the two enthalpies ($\Delta H_{cal}/\Delta H_{vh}$) gives the cooperative unit (c.u.) of the unfolding transition [51]. The cooperative unit can be associated to the amount of domains involved in the unfolding transition [51]. For small single domain proteins, the cooperative unit is usually close to one showing cooperative unfolding between two states, while the ratio of large proteins, like multi-domain antibodies, can clearly exceed one [29]. A ratio smaller than one indicates that the respective protein forms multimeric structures [51] or the transition is irreversible [29].

Aggregation assays

During recording of the fluorescence ratio from 20 °C to 95 °C with a heating rate of 1 K·min⁻¹, simultaneously the light scattering signal at 385 nm was monitored by the instrument (Prometheus NT.48) to analyze the onset temperature for the mAbs of this chapter at which the light scattering signal starts deviating from the baseline. This temperature is interpreted as temperature when the mAbs start to aggregate (T_{agg}). The scattering signal at 385 nm was also used to determine the aggregation onset times (t_{agg}) by isothermal measurements in this chapter. For the isothermal aggregation assays, samples were incubated at 65 °C and 75 °C until the onset of mAb aggregation can be observed. For the aggregation assays, the mAb concentration was adjusted to 1 mg·ml⁻¹.

Thermally induced stress studies

Thermally induced stress studies were performed at 25 °C and 40 °C to investigate the thermal mAb stability by size exclusion chromatography (SEC). While the aggregation assays were performed at 1 mg·ml⁻¹, the mAb concentration had to be increased to 10 mg·ml⁻¹ for thermally induced stress studies at 25 °C and 40 °C to observe stability changes in an appropriate time and using conditions more relevant for pharmaceutical applications. The solutions were filled into glass vials under laminar flow. mAb1 to mAb1e formulated in citrate buffer were stored at 25 °C for about 26 weeks and at 40 °C for about 14 weeks (study data of mAb1 to mAb1e was obtained from Boehringer Ingelheim). mAb2 and mAb3 in phosphate buffer were stored at 25 °C for 24 weeks and at 40 °C for 12 weeks. During the respective storage times, samples were analyzed at defined times. Stabilities were determined by analyzing the respective monomer, aggregate and fragment contents using SEC.

Size exclusion chromatography (SEC)

SEC analyses were performed to analyze the respective amounts of monomers, aggregates, and fragments in the mAb samples after storage of the mAb samples. For mAb1 to mAb1e in citrate buffer, HP-SEC measurements were conducted using an Alliance HPLC system (Waters, Milford, USA) (SEC data of mAb1 to mAb1e were

obtained from Boehringer Ingelheim). Samples were filtrated with a 0.2 μm filter and analyzed by injection of 10 μl protein solution with a concentration of 10 $\text{mg}\cdot\text{ml}^{-1}$. HP-SEC analyses were performed at a flow rate of 1 $\text{ml}\cdot\text{min}^{-1}$ with a 50 mM TRIS-HCl, 150 mM sodium chloride, pH 7.5 running buffer. A TSKgel[®] G3000 SWXL column (functional group: Diol, length: 300 mm, interior diameter: 7.8 mm, pore size: 25 nm, Tosoh Bioscience, Tokyo, Japan) was used to separate the samples at room temperature. For mAb2 and mAb3 formulated in phosphate buffer, UP-SEC analyses were performed using an Acquity UPLC H-class system (Waters, Milford, USA) at a protein concentration of 5 $\text{mg}\cdot\text{ml}^{-1}$ and an injection volume of 6 μl per sample. Samples were diluted with the mobile phase (200 mM L-arginine, 120 mM ammonium sulfate, 10 % (v/v) isopropanol, 32 mM phosphoric acid, pH 7.3) and filtrated with a 0.2 μm filter. UP-SEC analyses were performed at a flow rate of 0.2 $\text{ml}\cdot\text{min}^{-1}$ and an UP-SEC column (Acquity UPLC[®] BEH SEC 200 \AA , functional group: Diol, length: 300 mm, interior diameter: 4.6 mm, pore size: 20 nm, Waters) at room temperature. For both methods, detection occurs at 280 nm and monomer, aggregate, and fragment contents were analyzed as a proportion of the total peak area of the chromatograms. Each sample was measured as single value. The system suitability of the SEC analyses was verified by a functional protein standard (Boehringer Ingelheim Pharma GmbH & Co. KG), which was injected three times before and after the sample sets. Method uncertainties derived from the standard were analyzed to ± 0.05 % deviation in the determination of the area under the SEC curve for HP-SEC, while UP-SEC analysis showed a deviation of ± 0.02 %.

3.4 Results and discussion

Unfolding and thermodynamic profiling

Thermodynamic parameters describing the conformational properties of mAb1 to mAb1e, mAb2, and mAb3 were determined by fitting the IF unfolding traces (Fig. 3.1) with an apparent reversible three-state model (Eq. 3.3). The appropriate parameters from the fits are summarized in Tab. A.3.1 (Appendix).

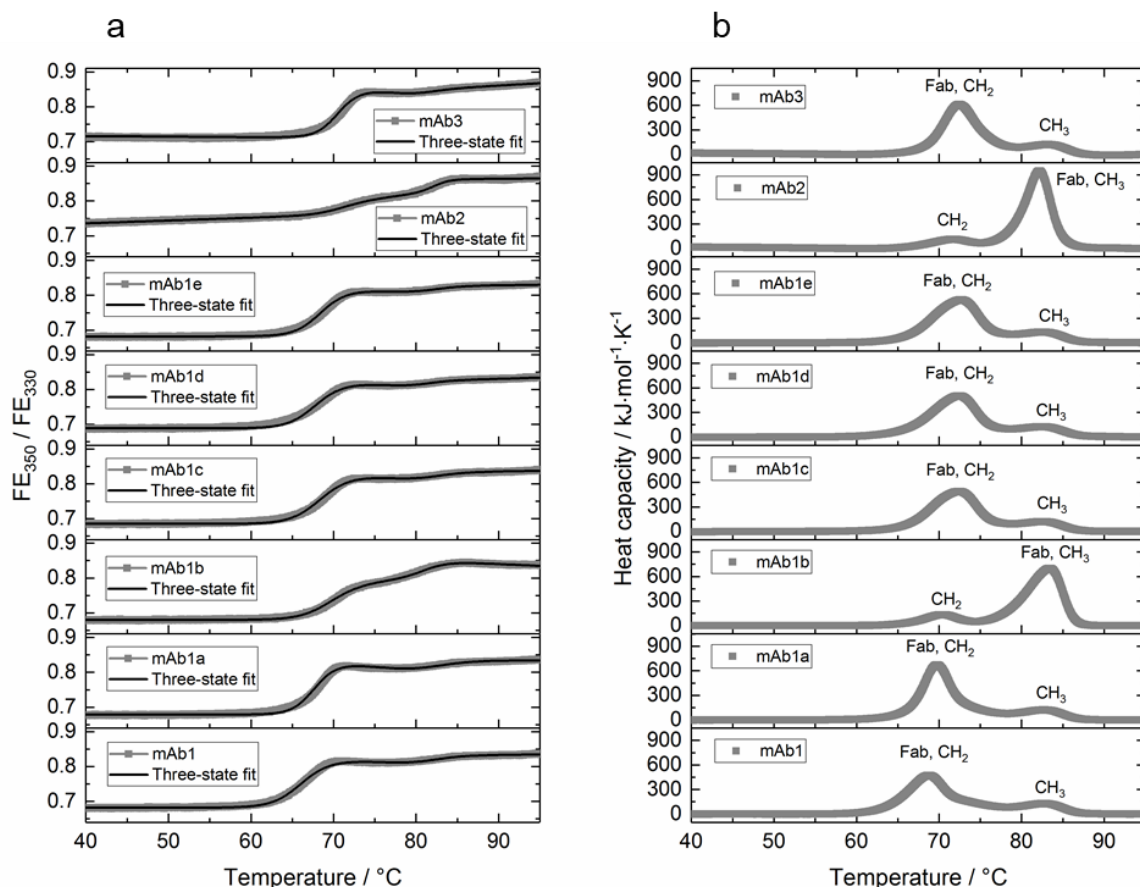


Fig. 3.1: IF (a) and DSC (b). (a) The mean and standard deviation of a triplicate of the FE_{350} / FE_{330} ratio are plotted against the temperature, shown as an envelope-curve from 40 °C to 95 °C including the standard deviations. The IF thermograms were fitted by the reversible three-state model (Eq. 3.3, black line). (b) The mean and standard deviation of a duplicate of the heat capacity are plotted against the temperature. Shown are the baseline subtracted DSC thermograms as an envelope-curve from 40 °C to 95 °C including the standard deviations.

In Fig. 3.1a, the IF unfolding profiles of the eight mAbs are illustrated. Eq. 3.3 was used to determine ΔH_{vh} at the transition midpoints of the unfolding curves of the mAbs. At the transition midpoint, where the two states of the equilibrium are populated equally, the change in Gibbs energy is zero ($\Delta G=0$) [18, 53]. This relation was used to calculate ΔS from the determined ΔH_{vh} values at the transition midpoint. The calculated thermodynamic parameters are summarized in Tab. 3.1.

Tab. 3.1: Thermodynamic and aggregation parameters derived from IF, DSC, and light scattering. Parameters of the Fab unfolding are highlighted in bold line width (Fab assignment by DSC, see text below). For IF, thermodynamic parameters were derived from the reversible three-state fit function (Eq. 3.3). The T_m and ΔH_{vh} values were directly obtained from fitting, with exception of $T_m(2)$ which was fixed to the transition midpoint for mAb1, mAb1a, mAb1c, mAb1d, mAb1e, and mAb3 to fit the small transition of these molecules. Therefore, an error of ± 0.5 °C was assumed. ΔS values were calculated using Eq. 3.5. For DSC, thermodynamic parameters were determined from a duplicate by applying appropriate fit functions (Bigauss and PearsonVII) to the DSC curves (Fig. A.3.1, Appendix). T_m , $c_{p, Tm}$, and ΔH_{cal} were directly derived from the fit functions. ΔH_{vh} values were calculated using Eq. 3.6 and ΔS was determined using Eq. 3.5. Δc_p values were determined from the DSC thermograms before baseline subtraction and were derived from the baseline before the first and after the second transition. Cooperative units (c.u.) were calculated from the ratio ($\Delta H_{cal}/\Delta H_{vh}$). For the total thermodynamics, $\Delta H_{vh}(\text{total})$ and $\Delta S(\text{total})$ values were calculated as sum of the enthalpies and entropies of the first and second transition to express changes in thermodynamics over the complete unfolding. Aggregation temperatures (T_{agg}) and time points (t_{agg}) at 65 °C and 75 °C were determined from the aggregation assays shown in Fig. 3.2.

Method	Parameter	mAb1	mAb1a	mAb1b	mAb1c	mAb1d	mAb1e	mAb2	mAb3
IF	$T_m(1)$ / °C	66.2 ± 0.0	67.8 ± 0.0	69.6 ± 0.1	68.6 ± 0.0	67.9 ± 0.0	68.5 ± 0.0	70.8 ± 0.2	70.6 ± 0.0
	$\Delta H_{vh}(1)$ / kJ·mol ⁻¹	544 ± 3.5	715 ± 5.5	505 ± 3.3	534 ± 2.3	571 ± 4.8	615 ± 3.9	528 ± 7.6	757 ± 5.7
	$\Delta S(1)$ / kJ·mol ⁻¹ ·K ⁻¹	1.60 ± 0.0	2.10 ± 0.0	1.47 ± 0.0	1.56 ± 0.0	1.67 ± 0.0	1.80 ± 0.0	1.54 ± 0.0	2.20 ± 0.0
	$T_m(2)$ / °C	81.9 ± 0.5	81.9 ± 0.5	81.3 ± 0.2	81.9 ± 0.5	80.9 ± 0.5	81.9 ± 0.5	82.3 ± 0.1	80.9 ± 0.5
	$\Delta H_{vh}(2)$ / kJ·mol ⁻¹	638 ± 34	504 ± 11	686 ± 46	608 ± 38	760 ± 24	617 ± 31	1050 ± 57	721 ± 26
	$\Delta S(2)$ / kJ·mol ⁻¹ ·K ⁻¹	1.80 ± 0.1	1.42 ± 0.0	1.94 ± 0.1	1.71 ± 0.11	2.15 ± 0.1	1.74 ± 0.1	2.95 ± 0.2	2.04 ± 0.1
	$\Delta H_{vh}(\text{total})$ / kJ·mol ⁻¹	1182 ± 34	1219 ± 12	1191 ± 46	1142 ± 38	1331 ± 25	1232 ± 31	1578 ± 57	1431 ± 51
	$\Delta S(\text{total})$ / kJ·mol ⁻¹ ·K ⁻¹	3.40 ± 0.1	3.52 ± 0.0	3.41 ± 0.1	3.27 ± 0.1	3.82 ± 0.1	3.54 ± 0.1	4.49 ± 0.2	4.11 ± 0.1
DSC	$T_m(1)$ / °C	68.8 ± 0.1	69.8 ± 0.1	70.4 ± 0.0	72.4 ± 0.0	72.4 ± 0.0	72.7 ± 0.0	71.7 ± 0.1	72.5 ± 0.1

$\Delta C_p(1) / \text{kJ}\cdot\text{mol}^{-1}\cdot\text{K}^{-1}$	18 ± 1	25 ± 1	17 ± 4	32 ± 1	32 ± 5	29 ± 1	35 ± 0	21 ± 4
$\Delta H_{\text{cal}}(1) / \text{kJ}\cdot\text{mol}^{-1}$	2972 ± 171	3824 ± 41	830 ± 55	3342 ± 102	3466 ± 101	3574 ± 106	876 ± 126	3626 ± 89
$\Delta H_{\text{vh}}(1) / \text{kJ}\cdot\text{mol}^{-1}$	595 ± 44	682 ± 29	575 ± 60	584 ± 15	570 ± 14	594 ± 7.6	486 ± 5	658 ± 15
$\Delta S(1) / \text{kJ}\cdot\text{mol}^{-1}\cdot\text{K}^{-1}$	1.74 ± 0.1	1.99 ± 0.1	1.67 ± 0.2	1.69 ± 0.0	1.65 ± 0.0	1.72 ± 0.0	1.41 ± 0.0	1.90 ± 0.0
$c_{p, T_m}(1) / \text{kJ}\cdot\text{mol}^{-1}\cdot\text{K}^{-1}$	454 ± 7.7	667 ± 20	121 ± 4.6	491 ± 2.8	497 ± 2.7	534 ± 9.0	108 ± 17	601 ± 28
c.u.(1)	5.0 ± 0.7	5.6 ± 0.3	1.5 ± 0.2	5.7 ± 0.3	6.1 ± 0.3	6.0 ± 0.3	1.8 ± 0.2	5.5 ± 0.0
$T_m(2) / ^\circ\text{C}$	82.7 ± 0.0	82.7 ± 0.0	83.4 ± 0.0	82.6 ± 0.0	82.5 ± 0.0	82.5 ± 0.2	82.2 ± 0.0	83.1 ± 0.1
$\Delta C_p(2) / \text{kJ}\cdot\text{mol}^{-1}\cdot\text{K}^{-1}$	20 ± 2	28 ± 11	27 ± 1	33 ± 1	32 ± 5	31 ± 9	52 ± 0	48 ± 17
$\Delta H_{\text{cal}}(2) / \text{kJ}\cdot\text{mol}^{-1}$	920 ± 137	894 ± 71	3835 ± 4	820 ± 52	846 ± 8.7	874 ± 83	3745 ± 4	732 ± 124
$\Delta H_{\text{vh}}(2) / \text{kJ}\cdot\text{mol}^{-1}$	641 ± 123	521 ± 13	754 ± 1	640 ± 0.5	673 ± 35	682 ± 111	1027 ± 36	648 ± 71
$\Delta S(2) / \text{kJ}\cdot\text{mol}^{-1}\cdot\text{K}^{-1}$	1.80 ± 0.3	1.46 ± 0.0	2.11 ± 0.0	1.80 ± 0.0	1.89 ± 0.1	1.92 ± 0.3	2.89 ± 0.1	1.82 ± 0.2
$c_{p, T_m}(2) / \text{kJ}\cdot\text{mol}^{-1}\cdot\text{K}^{-1}$	138 ± 6.0	110 ± 6.2	684 ± 0.3	125 ± 7.9	135 ± 5.6	140 ± 9.7	916 ± 33	111 ± 6.8
c.u.(2)	1.5 ± 0.5	1.7 ± 0.2	5.1 ± 0.0	1.3 ± 0.1	1.3 ± 0.1	1.3 ± 0.3	3.6 ± 0.1	1.1 ± 0.3
$\Delta H_{\text{vh}}(\text{total}) / \text{kJ}\cdot\text{mol}^{-1}$	1236 ± 131	1203 ± 31	1329 ± 60	1224 ± 15	1243 ± 38	1276 ± 111	1512 ± 36	1306 ± 72
$\Delta S(\text{total}) / \text{kJ}\cdot\text{mol}^{-1}\cdot\text{K}^{-1}$	3.54 ± 0.4	3.45 ± 0.1	3.79 ± 0.2	3.49 ± 0.0	3.54 ± 0.1	3.64 ± 0.3	4.30 ± 0.1	3.72 ± 0.2
$T_{\text{agg}} / ^\circ\text{C}$	67.0 ± 0.7	68.8 ± 0.1	81.8 ± 0.1	71.8 ± 0.1	71.9 ± 0.0	72.0 ± 0.0	80.3 ± 0.1	69.7 ± 0.1

Light scattering	t_{agg} at 65 °C / min	≤ 10	40 ± 5	> 900	40 ± 5	40 ± 5	40 ± 5	> 900	> 900
	t_{agg} at 75 °C / min	≤ 10 (both within temperature raise)	≤ 10 (within temperature raise)	70 ± 5	≤ 10 (within temperature raise)	≤ 10 (within temperature raise)	≤ 10 (within temperature raise)	90 ± 5	≤ 10 (within temperature raise)

The eight mAbs show positive values for $\Delta H_{vh}(1)$ and (2) (endothermal processes) analyzed by IF (Tab. 3.1) during the unfolding process, which can be attributed to the uptake of thermal energy during sample heating to break intramolecular bonds, like ionic, dipolar interactions (including hydrogen-bonds), disulfide bonds, and van-der-Waals interactions [38]. The entropy changes at the transition midpoints also show positive values showing that the unfolded mAb increases the entropy of the system, which could be explained with more degrees of freedom and a changed water structure and hydration properties for the unfolded mAb [54-57]. The increase in degrees of freedom ensues with the breaking and rearrangement of intramolecular interactions during the unfolding process of proteins. The analyzed van't Hoff enthalpies and entropies are in good agreement to reported values for other proteins [29, 56].

To compare the IF values determined by the reversible three-state model, DSC was performed as a control method. The DSC thermograms of the mAbs are illustrated in Fig. 3.1b (see above). The DSC thermograms of the mAbs show two transitions with positive enthalpy changes during the unfolding process. Thermodynamic parameters were derived from DSC thermograms by integrating the area under the curve using correlation functions, which fit the thermograms best (Fig. A.3.1, Appendix). Δc_p values were derived from the DSC thermograms before baseline subtraction. All derived thermodynamic parameters from DSC are summarized in Tab. 3.1. Similar to the investigated ΔH_{vh} derived from IF, the parameters derived from DSC show that ΔH_{vh} values for the eight mAbs were determined in a similar magnitude for both transitions, respectively. The DSC thermograms (Fig. 3.1b) show a larger transition and therefore a larger ΔH_{cal} (Tab. 3.1) during the first transition for mAb1, mAb1a, mAb1c, mAb1d, mAb1e, and mAb3. In contrast, for mAb1b and mAb2 the largest ΔH_{cal} in DSC is observed for the second transition. Previously, the largest signal in DSC has been associated with the Fab unfolding of IgG antibodies [17, 58-60]. Therefore, the Fab unfolding can occur in different temperature areas so that the second transition of mAb1b and mAb2 (Fab unfolding, largest DSC signal) has to be compared to the first transition of the remaining mAbs (Fab unfolding, largest DSC signal) to determine the respective Fab enthalpies. As other studies show, different mAb aggregation mechanisms could occur and it was assumed that aggregation is triggered by either the unfolding of the CH₂-domain [61] or by the Fab-region [9, 62]. More recently, a competing pathway of mAb aggregation triggered by both the Fab and Fc-fragment has been suggested [63]. However, the determined aggregation onset temperatures

(Tab. 3.1) are close to the melting temperatures of the Fab unfolding and the Fab T_m has been observed before to predict stability [64]. Due to these facts, the thermodynamics of the Fab unfolding was supposed and tested to predict the thermal stability of the used mAbs. A thermal stability ranking according to the Fab enthalpies and comparison to parameters like melting temperatures or aggregation temperatures is discussed later in this chapter.

Unfolding cooperativity

Determining the cooperative unit as the ratio of the two enthalpies ($\Delta H_{cal}/\Delta H_{vh}$) derived from DSC experiments provides information about the potential underlying unfolding mechanism of individual domains of the mAbs. In this case, the ratio between ΔH_{cal} and ΔH_{vh} reflects the amount of cooperative units within each individual transition involved during mAb unfolding. The cooperative units of the mAbs are summarized in Tab. 3.1. The first DSC transition of mAb1b and mAb2 (Fig. 3.1b) can be related to the CH₂-domain of the mAb, because the transition of the Fab is accompanied by the largest ΔH_{cal} as the second transition and the smaller DSC signal in front of the Fab has been assigned to the CH₂-domain for the respective temperature [17, 58]. Due to the large Fab transition, an overlap between CH₂-domain and the Fab is observed. Calculating the corresponding cooperative unit results in a ratio of 1.5 for mAb1b and 1.8 for mAb2 for the CH₂-domain. This behavior could stem from Fab transitions that partially overlap the CH₂-unfolding in the assessed DSC thermograms. In the case of the remaining mAbs, the unfolding of the CH₂-domain is most likely overlaid by the Fab unfolding, which occurs as the first transition showing the largest ΔH_{cal} . A strong indicator for this is that the cooperative units of these mAbs are between 5 and 6, which show that the Fab transition is not cooperative between two states. The ratio of about 5.5 can be related to the amount of domains involved in the Fab transition (four domains: variable and constant domains of the heavy and light chains, respectively), the overlaid CH₂-domain and the partially overlap of the CH₃-domain in the not fully separated DSC transitions. This correlation can also be applied to the Fab unfolding transitions of mAb1b (second transition cooperative unit is 5.1) and mAb2 (second transition, cooperative unit is 3.6), with the difference that the CH₃-domain is most likely overlaid by the Fab unfolding and a partially overlap to the CH₂-domain. The cooperative unit of mAb2 could indicate that different domains within the Fab show

cooperativity among each other and therefore reduce the value. The second transition of mAb1, mAb1a, mAb1c, mAb1d, mAb1e, and mAb3 can be attributed to the CH₃-domain, which yields cooperative units in a range of 1.1 to 1.7, which can also be associated with the partially overlap to the Fab transition. However, the single CH₃-domain of these mAbs, as well as the CH₂-domain for mAb1b and mAb2 are more likely to follow a cooperative transition as the Fabs. A cooperative unit of 1 is found for identical values of ΔH_{vh} and ΔH_{cal} , so that the theoretical ΔH_{vh} of the unfolding transitions equates to the experimental ΔH_{cal} . For the eight mAbs in this chapter, the CH₂-domain, CH₃-domain, and especially the Fabs show smaller ΔH_{vh} compared to ΔH_{cal} . Considering this, the calculated ΔH_{vh} for the transitions using DSC as well as using the reversible three-state fitting model yield a theoretical enthalpy for the unfolding transition that assumes the transition cooperative between two states.

Thermodynamics describing the complete unfolding

After investigation of the thermodynamics of the single transitions, the total thermodynamic parameters were determined over both transitions to describe the thermodynamic changes of the complete mAb (Tab. 3.1). It can be seen that mAb3 has a slightly lower $\Delta H_{vh}(\text{total})$ compared to mAb2 determined both with IF and DSC, which can be interpreted that the overall unfolding of mAb3 requires less energy compared to mAb2. The total thermodynamics for mAb1 to mAb1e show similar $\Delta H_{vh}(\text{total})$ among the mAbs and provide less differences in thermodynamics than determining $\Delta H_{vh}(\text{Fab})$ (Tab. 3.1) and a stability ranking according to $\Delta H_{vh}(\text{total})$ is not meaningful.

Aggregation assays as predictive tools

Following the investigations of the unfolding behavior, the aggregation onset temperatures (T_{agg}) of all mAbs were analyzed. Additionally, the aggregation onset times (t_{agg}) of the eight mAbs were investigated by isothermal measurements. For the first isothermal cycling experiment, the temperature was set to 65 °C for 900 min. This temperature is below the first melting temperature for all mAbs, where more than 50 % of the mAbs are in their folded states. For the second isothermal cycling experiment, the temperature was set to 75 °C for 160 min, due to the fact that this temperature lies

between $T_m(1)$ and $T_m(2)$ of all mAbs, and thus reflects the intermediate state for all mAbs. The temperature ramp and the isothermal cycling experiment at 65 °C and 75 °C are illustrated in Fig. 3.2.

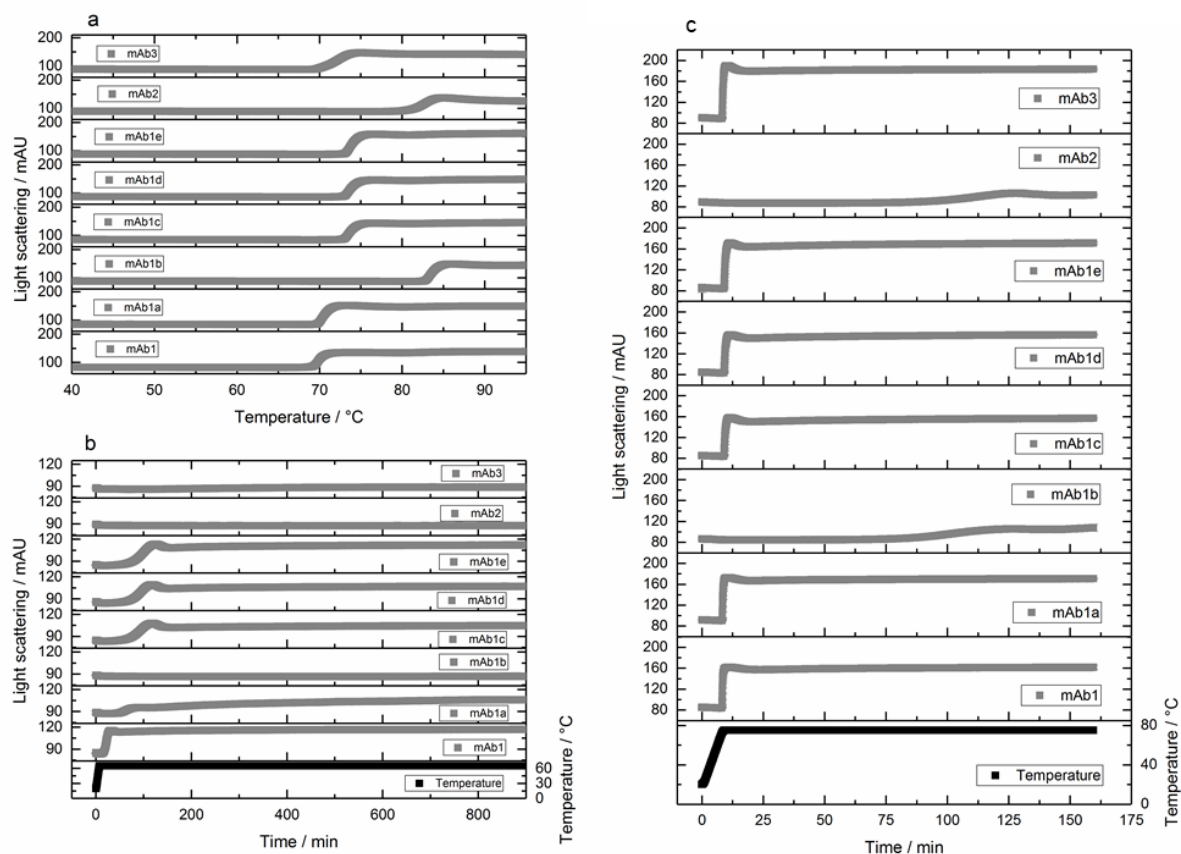


Fig. 3.2: Aggregation assay plots. The mean light scattering signals and standard deviation of a triplicate (exception mAb1b in (c) as a duplicate) are plotted against the temperature (a), the time (b), and (c). The plots are shown as an envelope-curve including the standard deviations. For the isothermal measurement at 65 °C (b), the samples were heated from 20 °C to 65 °C and the temperature was held for 900 min. For the isothermal measurement at 75 °C (c), the samples were heated from 20 °C to 75 °C and the temperature was held for 160 min. Aggregation is determined as the point at which the light scattering signal starts to increase.

Values of T_{agg} and t_{agg} are summarized for each mAb in Tab. 3.1. For mAb1 to mAb1e, the T_{agg} s show distinct differences of about 15 K between the highest T_{agg} (mAb1b) and the lowest (mAb1), while mAb1a shows the second lowest T_{agg} and mAb1c, mAb1d, and mAb1e show equal values (Fig. 3.2a). The determination of T_{agg} shows a 10 K higher T_{agg} for mAb2 compared to mAb3. The investigated t_{agg} at 65 °C (Fig. 3.2b) show distinct differences between mAb1b and the remaining mAb variants, while mAb2 and mAb3 show a similar profile with no distinct t_{agg} at 65 °C. At 75 °C (Fig. 3.2c), all

mAbs start to aggregate during the temperature ramp, with exception of mAb2 and mAb1b.

Thermally induced stress studies

To assess the different rankings to thermal stability of the mAbs, thermally induced stress studies at temperatures of 25 °C and 40 °C were performed (Fig. 3.3).

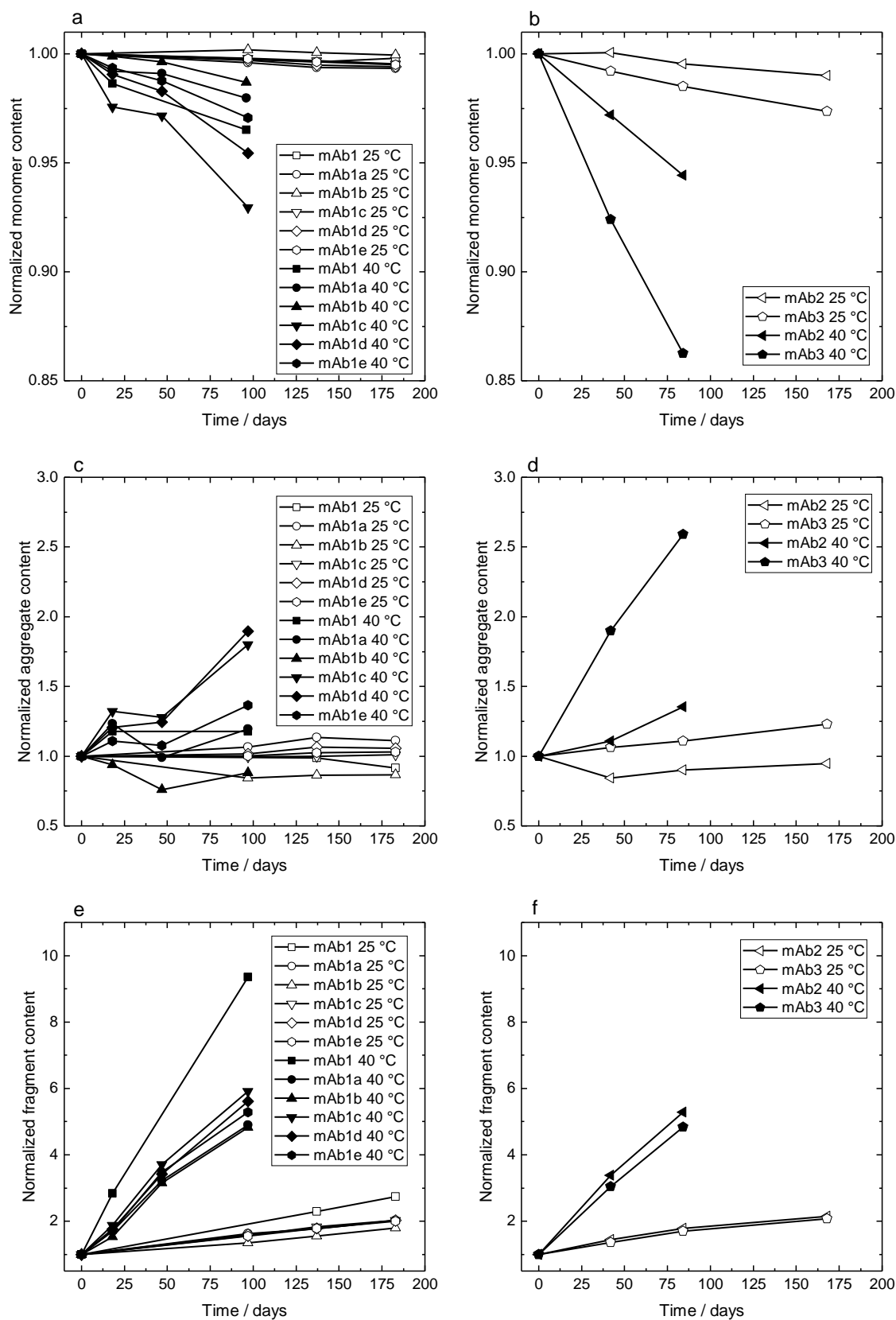


Fig. 3.3: Thermal stability derived from SEC of the mAbs at 40 °C and 25 °C. (a, b) normalized monomer, (c, d) normalized aggregate, and (e, f) normalized fragment content against the time.

Thermal stability is investigated by analyzing the monomer, aggregate, and fragment contents from analytical SEC (Fig. 3.3). Comparing mAb1 to mAb1e, the mAbs show a comparable trend in the monomer, aggregate, and fragment content at 25 °C, with a slightly higher fragment content increase for mAb1. Therefore, a clear differentiation between mAb1 to mAb1e at 25 °C is not obvious. For 40 °C, differences between these mAbs are more pronounced. According to the monomer content, the following thermal stability ranking can be observed: mAb1b > mAb1a > mAb1e > mAb1 ~ mAb1d > mAb1c. Comparing the aggregate content of these mAbs shows that mAb1d and mAb1c have a higher and mAb1b a lower aggregate content increase at 40 °C compared to the remaining mAbs. The fragment content increase at 40 °C shows a comparable trend for these mAbs, with exception of mAb1 showing an increased fragmentation. Comparing mAb2 with mAb3 at 25 °C (Fig. 3.3), a higher decrease in monomer content and a slightly higher increase in aggregate content and a comparable trend in the fragment content increase can be observed for mAb3. At 40 °C, mAb3 shows a distinct decrease in monomer content and a pronounced increase in aggregate content compared to mAb2. Only the increase of the fragment content is nearly the same at 40 °C for the two mAbs, which indicates that mAb3 shows a faster aggregation behavior than decomposition into fragments. This is in contrast to mAb2, which shows faster increase in the fragment content and a slower increase in aggregation formation. This observation underlines a pronounced aggregation behavior of mAb3 compared to mAb2.

Predictive ranking of different parameters

After investigating the thermal stability of the mAbs, the predictive character of the different investigated parameters can now be evaluated. To account for different colloidal influences from the two used buffers, thermal stability was only compared between the mAbs in the same buffer to rank the mAbs according to their conformational stability, described by the investigated predictive parameters in this chapter. The predicted stability deduced from the different parameters are compared to the ranking according to the outcome of the thermally induced stress studies. The results are summarized in Tab. 3.2.

Tab. 3.2: Thermal stability ranking deduced from different parameters. The different rankings of the parameters are deduced from Tab. 3.1. For SEC, the symbol (>) stands for a mAb with a higher stability regarding to monomer loss (Fig. 3.3a), while (~) stands for a comparable stability. For the predictive parameter, the symbol (>) stands for a value of the mAb larger than the following mAb outside of the margin of errors, while (\geq) refers to a value within the margin of errors. The symbol (=) stands for a parameter, which is identical in the precision of the parameter listed in Tab. 3.1. mAbs highlighted in bold letters show a strong discrepancy to the SEC ranking, meaning for mAb1 to mAb1e that the mAb deviates from the SEC ranking in three or more positions or that three or more mAbs show identical values. For mAb2 and mAb3, each deviation in the position and identical values are interpreted as a strong discrepancy to SEC, because differences between mAb2 and mAb3 are more pronounced in SEC than for mAb1 to mAb1e.

SEC(monomer)	mAb1b	>mAb1a	>mAb1e	>mAb1	~mAb1d	>mAb1c	mAb2	>mAb3
at 40°C								
$\Delta H_{vh}(\text{Fab, IF})$	mAb1a	\geq mAb1b	>mAb1e	>mAb1d	>mAb1	>mAb1c	mAb2	>mAb3
$\Delta H_{vh}(\text{Fab, DSC})$	mAb1b	>mAb1a	>mAb1	\geq mAb1e	\geq mAb1c	\geq mAb1d	mAb2	>mAb3
$\Delta H_{cal}(\text{Fab, DSC})$	mAb1b	\geq mAb1a	>mAb1e	\geq mAb1d	\geq mAb1c	>mAb1	mAb2	>mAb3
$T_m(\text{Fab, IF})$	mAb1b	>mAb1c	>mAb1e	>mAb1d	>mAb1a	>mAb1	mAb2	>mAb3
$T_m(\text{Fab, DSC})$	mAb1b	>mAb1e	>mAb1c	=mAb1d	>mAb1a	>mAb1	mAb2	>mAb3
$T_m(1, \text{IF})$	mAb1b	>mAb1c	>mAb1e	>mAb1d	>mAb1a	>mAb1	mAb2	\geq mAb3
$T_m(1, \text{DSC})$	mAb1e	>mAb1c	=mAb1d	>mAb1b	>mAb1a	>mAb1	mAb3	>mAb2
T_{agg}	mAb1b	>mAb1e	>mAb1d	\geq mAb1c	>mAb1a	>mAb1	mAb2	>mAb3
t_{agg} at 65 °C	mAb1b	>mAb1a	=mAb1c	=mAb1d	=mAb1e	>mAb1	mAb2	=mAb3
t_{agg} at 75 °C	mAb1b	>mAb1a	=mAb1c	=mAb1d	=mAb1e	=mAb1	mAb2	>mAb3

Comparing the ranking based on $\Delta H_{vh}(\text{Fab})$ analyzed both with IF and DSC and ΔH_{cal} determined with DSC to a commonly used method determining T_m values [15], give other rankings predicting the stability of the mAbs (Tab. 3.2). By ranking mAb1 to mAb1e according to $T_m(1)$, without assigning the T_m to a certain mAb-region, would predict mAb1c as the mAb showing the second highest stability. This discrepancy can also be observed by ranking the mAbs according to $T_m(\text{Fab})$. The second highest stability was detected for mAb1a by SEC, which would be ranked according to T_m values to a mAb with a lower stability. Comparing $T_m(1)$ of mAb2 with mAb3, nearly the same stability for the mAbs is expected, whereas $T_m(1)$ analyzed by DSC predicts

mAb3 with a higher stability than mAb2. Analyzing the $T_m(\text{Fab})$ of mAb2 and mAb3 give the correct ranking according to SEC. Analyzing the stability rankings based on T_{agg} and t_{agg} do not provide high differences between mAb1 to mAb1e, with exception of mAb1b. As Tab. 3.2 illustrates, the derived enthalpies from the Fab predict the thermal stability of the tested mAbs better than the other parameters. By comparing the rankings of $\Delta H_{\text{vh}}(\text{Fab})$ and $\Delta H_{\text{cal}}(\text{Fab})$ determined by DSC, differences in the rankings can be observed. The differences of the two enthalpies derived from DSC can be explained by the fact that according to Eq. 3.6 ΔH_{vh} is not only determined by ΔH_{cal} , but also determined by the heat capacity of the transition (c_p, T_m). Another fact that influences the discrimination of mAbs using ΔH_{vh} and ΔH_{cal} of the Fabs are differences in T_m , which can also lead to different domains involved in the Fab transition. This can be observed for mAb1b and mAb2, showing a Fab transition, which overlays the CH₃-domain. For the remaining mAbs, the Fab unfolds within the first transition and overlays the CH₂-domain. These differences in the unfolding mechanism can also lead to different outcomes in the ranking between ΔH_{vh} and ΔH_{cal} . In summary, the three determined enthalpy values of the Fab indeed do not match exactly to the SEC ranking at 40 °C in every case for mAb1 to mAb1e. However, the rankings of the Fab thermodynamics give a higher accordance to the investigated 40 °C stability than T_m , T_{agg} , and t_{agg} . Therefore, the investigated mAbs in this chapter indicate that the determination of Fab thermodynamic parameters from unfolding experiments gives a closer insight into mAb thermal stability than just using melting temperatures and aggregation onset temperatures and times as commonly used parameters. Therefore, the Fab thermodynamics should be considered, besides to the commonly used parameters, by predicting the thermal stability of mAbs.

Application and deviations between intrinsic fluorescence (IF) and differential scanning calorimetry (DSC)

The IF and DSC calculations are based on the assumption that a thermodynamic equilibrium exists between the folded, intermediate and unfolded state during the thermal unfolding reaction, as described by the Lumry-Eyring Nucleated Polymerization (LENP) model [8, 65]. In the LENP-model, reversible unfolding occurs faster than irreversible aggregation so that a folding-unfolding equilibrium between the folded, intermediate, and unfolded state is reached [6]. The LENP-model describes

aggregation as the rate-limiting step in the unfolding/aggregation reaction and was found to be valid for a wide range of proteins and polypeptides [8]. The accuracy of the LENP-model describing the aggregation mechanism for therapeutic mAbs has been shown by Singla et al. by comparing aggregate generation to different aggregation mechanism models finding best fits to the LENP-model [66]. Additionally, an important prerequisite for the exact determination of thermodynamics is the reversibility of the reaction. Indeed, during heating the mAbs start to aggregate, which can be concluded from the aggregation onset temperatures. In this case, the folded/unfolded equilibrium is partially shifted to irreversible aggregation and the reaction is not fully reversible at higher temperatures. Therefore, the disruption of the equilibrium can influence the outcome of the calculated values and all thermodynamic parameters should be treated as apparent values. However, the agreement of the thermodynamics by two independent methods implemented through a reversible three-state fitting model for IF and DSC, as a direct, model independent method, indicates a sufficient accuracy discriminating different mAbs by calculating thermodynamic parameters. The accordance of ΔH_{vh} values from IF and DSC is visualized in Fig. 3.4.

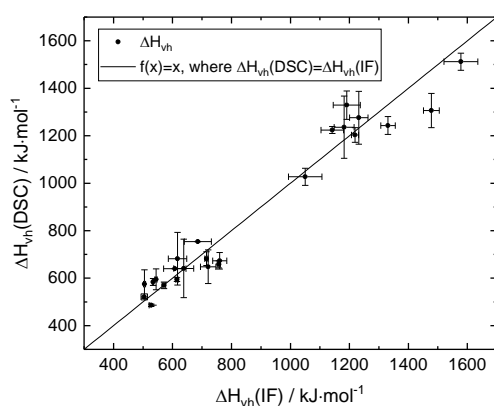


Fig. 3.4: Thermodynamics derived from IF and DSC. $\Delta H_{vh}(DSC)$ against $\Delta H_{vh}(IF)$. Enthalpies of the mAb unfolding are plotted for DSC and IF, illustrating the accordance of the values. The black solid line illustrates the ideal function ($f(x)=x$), where $\Delta H_{vh}(DSC)$ equals $\Delta H_{vh}(IF)$.

The total thermodynamic parameters ($\Delta H_{vh}(\text{total})$) of IF fitting and DSC show similar values with deviations between 1 % and 10 % for the eight mAbs, which confirm the applicability of the introduced approaches for IF and DSC. The deviations for the van't Hoff enthalpies of the single transitions between IF and DSC analysis were observed for the investigated eight mAbs in a range of ≤ 13 %. The observed deviations can be

explained with not completely resolved transitions both in IF and DSC and with neglected Δc_p in IF. Moreover, in IF analyses only changes of fluorophores like tryptophan and tyrosine can be detected, while DSC can detect the heat capacity of all amino acids. This could also lead to differences detecting and analyzing parameters of the unfolding transitions. Higher agreement in the determination of thermodynamic unfolding parameters between spectroscopic methods and DSC has been observed by Seelig et al., using a sequential unfolding model, based on the Zimm-Bragg theory for thermal and chemical unfolding [46, 67]. For single domain proteins, they determined higher accordance of the sequential unfolding model to DSC compared to a two-state model [46]. However, this chapter shows the applicability of a reversible three-state model describing the thermodynamics of multi-domain antibodies. The applied reversible three-state fitting model shows predictive character of the calculated thermodynamic parameters and the agreement to experimental characterization via SEC of the therapeutic mAbs. In summary, the reversible three-state fitting model was used to investigate unfolding thermodynamic parameters from antibodies of the detected fluorescence emission ratio (FE_{350} / FE_{330}) in IF applications and those values are comparable to thermodynamic parameters derived from DSC experiments. This chapter also shows predictive character of the obtained thermodynamic parameters of the Fab region in a sense that a lower enthalpy is connected to higher monomer loss within the tested mAbs in thermally induced stress studies. These findings indicate that the introduced theoretical thermodynamic model is sufficient and can be used to calculate thermodynamic parameters for mAbs, which predict the observed thermal stabilities best under the investigated methods.

3.5 Conclusion

In this chapter, unfolding thermodynamics and aggregation profiles of eight mAbs were investigated. The mAbs show differences in the unfolding and aggregation properties regarding melting temperatures, aggregation temperatures, aggregation time, and thermodynamic parameters. The results show that thermodynamic parameters, derived from a reversible three-state fitting model of IF unfolding traces, show similar values to those values directly obtained from DSC. The investigated Fab enthalpies can predict and explain thermal stability at 40 °C of the assessed mAbs better than the investigated T_m s and aggregation properties, while at 25 °C no distinct changes for

mAb1 to mAb1e can be observed so that a meaningful ranking cannot be made. Thermodynamic parameters derived by temperature dependent unfolding experiments can be used to improve protein engineering by selecting most promising mAb candidates and identify and sort the most unstable out. In practice, this means that different mAb candidates in a certain formulation can be rapidly analyzed by thermal techniques like IF spectroscopy and DSC by investigating their individual thermodynamic parameters. Dependent on the outcome and evaluation of the thermodynamic parameters, the most promising candidates can be selected for further investigations and more time intensive long-term stability studies finding the most appropriate mAb candidate. Therefore, this chapter shows that thermodynamic characterization can provide information, which can be used to support the prediction of stability rankings.

Chapter IV – Kinetic profiling

Parts of this chapter have been submitted for publication by Richard Melien, Nuska Tschammer, Dariush Hinderberger, Patrick Garidel, Michaela Blech.

Author contributions

R. Melien, N. Tschammer, and M. Blech designed the study. M. Blech and P. Garidel supervised the study. Experimental research, data analysis, and evaluation was performed by R. Melien. The first draft was written by R. Melien and was reviewed by N. Tschammer and D. Hinderberger.

4.1 Abstract

Purpose: The complex multi-domain structure of therapeutic monoclonal antibodies (mAbs) and the various mechanisms leading to degradation of their pharmaceutically active conformation provide major challenges in the prediction of their thermal stability. Although several assays and parameters have been developed for characterizing and predicting protein stability, there is need for new approaches with predictive power.

Methods: This chapter introduces activation energy (E_a) as a kinetic parameter determined from intrinsic fluorescence (IF) unfolding thermograms recorded by a newly developed experimental device (called: “Novel Experimental Setup” (NES)). An apparent irreversible three-state fit model based on the Arrhenius integral was used to determine activation energies of the respective unfolding transitions. 34 mAbs could such be classified in four different categories regarding their respective IF unfolding profile. For those mAbs, which can be analyzed by the irreversible three-state model, E_a values were determined and compared to van't Hoff enthalpies (ΔH_{vh}) as a thermodynamic parameter determined by a reversible three-state model (introduced in Chapter III). Subsequently, the thermodynamic and kinetic parameters were tested to correlate with mAb thermal stability at 25 °C and/or 40 °C analyzed by size exclusion chromatography (SEC) and the predictive character of these parameters was compared to melting temperatures (T_m) of the IF unfolding transitions.

Results: An overall trend of increasing E_a values by increasing ΔH_{vh} is observed for the CH₂-domain and the Fab unfolding transition, showing different values for various mAbs. Hence, thermodynamic and kinetic characterization of these unfolding transitions can be used to discriminate mAbs. By doing so, it is found that the activation energy of the CH₂ transition ($E_a(\text{CH}_2)$) shows strongest correlations with thermal stability at 25 °C and 40 °C compared to ΔH_{vh} and T_m of CH₂ transition. Moreover, the predictive parameters determined for the CH₂-domain show stronger correlations with thermal stability than those parameters derived for the Fab region.

Conclusion: This chapter provides a toolbox for different predictive parameters for thermal stability of mAbs. Determining activation energies from IF unfolding transitions can be used as a supportive tool to discriminate and characterize thermal stability of different mAbs. For that reason, activation energies should be considered to describe thermal stability of mAbs, in addition to other predictive parameters.

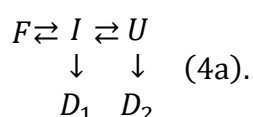
4.2 Introduction

The increasing number of protein-based biopharmaceuticals and its relevance for treating various diseases underlines the need for suitable methods to characterize the biophysical properties of these products [7, 32, 68]. However, the complexity of the biologic structure, such as a monoclonal antibody (mAb), necessitates the use of various experimental and theoretical methods to describe the properties of the molecule [7, 14]. Regarding therapeutic mAbs, one major challenge is the tendency for degradation of the therapeutic active monomer structure [17]. As degradation mechanisms, the formation of aggregates [6] or the decomposition into fragments [11] can be mentioned. Both mechanisms lead to a decreased monomer content within the drug solution and therefore, a decreased activity and a possible reduction of the therapeutic effect. Moreover, the formed aggregates can cause an unwanted immune response after application to a patient [4, 37]. Therefore, evaluating parameters describing the mAb stability can help to find appropriate drug substances and optimized formulation conditions for prevention of fast degradation of the therapeutic molecule [69]. For this purpose, thermal stability of various mAb formulations were tested to correlate with activation energies (E_a) determined from IF unfolding

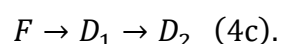
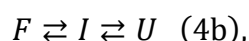
experiments and were compared to melting temperatures (T_m) and van't Hoff enthalpies (ΔH_{vh}) to define predictive parameters for thermal stability of mAbs.

Protein denaturation

Irreversible protein denaturation may occur from a reversible equilibrium between a folded and an unfolded protein state [5, 29, 65]. For two apparent unfolding transitions, as they are often observable in intrinsic fluorescence (IF) mAb thermograms, the denaturation model can be interpreted and schematically described by the following reactions (Eq. 4a):



From a reversible equilibrium between three protein states (folded (F), intermediate (I), and unfolded (U)), irreversible denaturation can occur to a first denatured state (D_1) from the intermediate state and to a second denatured state (D_2) from the unfolded state. Consequently, two different irreversible reactions can be described. However, a mathematical description according to Eq. 4a would be very complex and the five different states cannot be mapped directly onto two apparent transitions that are often observable in IF thermograms of mAbs. Different other models, e.g. the Zimm-Bragg theory [45], describing protein unfolding induced by temperature or chemical denaturation are of current interest [46, 48, 67]. The different views related to thermodynamic and/or kinetic protein stability are still under investigation [70-72]. To describe the apparent transitions according to a three-state model in this chapter (see Material and methods), the reactions have to be separated into reversible reactions for thermodynamics (Eq. 4b) and irreversible reactions for kinetics (Eq. 4c):



4.3 Material and methods

Antibody formulations

In this chapter, 34 therapeutic immunoglobulins type G, isotype 1 (IgG1) mAbs provided by Boehringer Ingelheim Pharma GmbH & Co. KG (Biberach, Germany) were examined. Regarding the mAb amino acid sequence, 12 mAbs are unrelated among each other (mAb_a to mAb_h and mAb₂ to mAb₈), whereof three mAbs are variants of a parent mAb sequence (mAb_c and mAb_f; mAb₇ and mAb_g; mAb_d and mAb_e). These mAbs were expressed by Chinese hamster ovary (CHO) cells and purified according to Bergemann et al. [50] using several purification steps including protein A and ion chromatography. Processing and information of additional six mAb variants (mAb₁ variants) are reported in [22] and Chapter III, while information of the ten used mAb variants (mAb₁₀ variants) can be found in [23], where it was denoted as mAb₂. Finally, three different variants (mAb₉ variants) were used in this chapter.

All mAbs were analyzed in up to four different formulations. The first formulation, F1, is a 10 mM histidine buffer at pH 6.0, the second formulation (F2) is a 10 mM histidine buffer, 150 mM NaCl at pH 6.0, while the third formulation (F3) is a 10 mM histidine buffer at pH 6.0 containing 220 mM trehalose. A fourth formulation contain 25 mM sodium citrate, 125 mM NaCl at pH 6.0. This buffer is referred to as "citrate buffer". All mAbs were transferred to the plane histidine formulation (F1) and in citrate buffer with exception of the mAb₁₀ variants, which were only analyzed in citrate buffer and mAb_e only formulated in the three different histidine formulations. The mAbs were transferred to the respective buffers by dialysis using 20 kDa molecular weight cut-off (MWCO) dialysis cassettes (Slide-A-Lyzer™, Thermo Fisher Scientific Inc., Waltham, USA) and diluted to the needed mAb concentration. The excipients of formulation F2 (NaCl) and F3 (trehalose) were added to the mAb solutions after dialysis using suitable spike solutions. Protein concentrations were determined by UV/Vis absorbance measurements at a wavelength of 280 nm using a UV/Vis Lambda 35 photo spectrometer (Perkin Elmer Inc., Waltham, USA).

Thermally induced stress studies

For the investigation of thermal stability, three different thermally induced stress studies were performed (data of all three stress studies were obtained from Boehringer

Ingelheim). For the first thermally induced stress study in this chapter, nine mAbs (mAb_a to mAb_g, mAb₄, and mAb₅) at a concentration of 50 mg·ml⁻¹ dissolved in formulation F1, F2, and F3 were incubated at a temperature of 25 °C and 40 °C for four weeks. The mAb formulations were filled under laminar flow into glass vials and incubated for the respective time and temperatures. Thermal stability was assessed by size exclusion chromatography (SEC) analyses. For a second thermally induced stress study, the analysis for the mAb₁₀ variants was performed according to [23]. Briefly, the mAb₁₀ variants were incubated for about 26 weeks at 40 °C containing a mAb concentration of 5 mg·ml⁻¹ formulated in citrate buffer and thermal stability was investigated by SEC. The analysis and data of the thermally induced stress study of the mAb₁ variants in citrate buffer is reported in Chapter III.

Size exclusion chromatography (SEC)

To analyze the first thermally induced stress study in this chapter, SEC analyses were performed by using an Acquity UPLC H-class system (Waters, Milford, USA) with an injection volume of 6 µl sample at a protein concentration of 5 mg·ml⁻¹ (data were obtained from Boehringer Ingelheim). UP-SEC analyses were performed at room temperature with a flow rate of 0.2 ml·min⁻¹ of a solution containing 200 mM L-arginine, 120 mM ammonium sulfate, 10 % (v/v) isopropanol, 32 mM phosphoric acid, pH 7.3 as mobile phase. For separation, an UP-SEC column (Acquity UPLC® BEH SEC 200Å, functional group: diol, length: 30 cm, interior diameter: 4.6 mm, pore size: 20 nm, Waters) was used. Monomer, aggregate, and fragment contents were detected at 280 nm as a proportion of the total signal area of the chromatogram.

Intrinsic fluorescence (IF) analyses

For the recording of temperature dependent unfolding experiments, two different devices measuring IF were used in this study: a commercially available device, which was also used in Chapter III called as “Prometheus” and a newly developed experimental device, named as “Novel Experimental Setup” (NES). All measurements were performed in duplicates at a mAb concentration of 1 mg·ml⁻¹ using high sensitivity glass capillaries or standard glass capillaries (NanoTemper Technologies GmbH, Munich, Germany). Temperature ramps were performed from 35 °C to 95 °C at a

heating rate of 1 K·min⁻¹. These conditions were used for both the Prometheus instrument and the NES to provide comparable results and represent data for a commonly used heating rate.

Prometheus instrument

The Prometheus NT.48 - nanoDSF instrument (NanoTemper Technologies GmbH, Munich, Germany) was used to detect temperature dependent IF unfolding profiles, as described in Chapter III. The reversible three-state model (Eq. 3.3, Chapter III) was used to determine values of ΔH_{vh} . In this chapter, thermodynamics were determined as average values from two independent fits of a duplicate measurement and errors are reported as standard deviations.

Novel Experimental Setup (NES)

The NES, which is based on the nanoDSF technology (NanoTemper Technologies GmbH, Munich, Germany) tracks fluorescence emission at the same wavelengths as the Prometheus and can be used to perform heating rate dependent thermal unfolding experiments. The NES has new high power heating elements and can thus enable high speed heating rates spanning from 1 K·min⁻¹ up to 30 K·min⁻¹ up to 95 °C, keeping the heating rate constant over the full temperature range. Besides a heating rate of 1 K·min⁻¹, values of E_a were also determined at faster heating rates of 18 K·min⁻¹ and 30 K·min⁻¹. A Python based evaluation script (programmed by NanoTemper Technologies), exclusively developed for IF profiles recorded by the NES, was used to determine values of E_a .

The determination of activation energies is based on an irreversible unfolding model between a folded (F), a first denatured (D₁), and a second denatured protein state (D₂) according to Eq. 4c. For a constant heating rate (B), the irreversible reaction can be described by the degree of conversion (α) on the temperature (T) based on the Arrhenius equation as Eq. 4.1 for the two apparent IF transitions, respectively, where R is the gas constant and A the frequency factor [73]:

$$\frac{d\alpha}{dT} = \frac{A}{B} \exp\left(-\frac{E_a}{RT}\right) \quad (4.1).$$

By partial integration, Eq. 4.1 can be rewritten as Eq. 4.2 [73], where $g(\alpha)$ is the integral conversion function. The frequency factor (A) is assumed temperature independent:

$$g(\alpha) = \frac{A}{B} \int_{T_0}^{T_{end}} \exp\left(-\frac{E_a}{RT}\right) dT \quad (4.2).$$

The integral in Eq. 4.2, also known as Arrhenius integral, cannot be solved analytically so that an approximation has to be used. One suitable approximation for the Arrhenius integral A_r is shown in Eq. 4.3 [74]:

$$\begin{aligned} & \frac{A}{B} \int_{T_0}^{T_{end}} \exp\left(-\frac{E_a}{RT}\right) dT \\ &= \frac{A}{B} \left(\frac{RT^2}{E_a} \exp\left(-\frac{E_a}{RT}\right) \frac{0.999940083636437E_a + 0.278603058646963RT \ln\left(\frac{E_a}{RT}\right) + 0.367233903690375RT}{E_a + 0.264770161932887RT \ln\left(\frac{E_a}{RT}\right) + 2.43832629069336RT}\right) \\ &= \frac{A}{B} A_r \quad (4.3). \end{aligned}$$

For the described irreversible three-state unfolding model (Eq. 4c), the signal (y) of the IF thermogram can be described by the single state signals (Y_i) and their respective protein state fractions (f_i) (Eq. 4.4) for the three states F, D_1 , and D_2 [41]:

$$y = f_F Y_F + f_{D_1} Y_{D_1} + f_{D_2} Y_{D_2} \quad (4.4).$$

The amount protein state fraction (f_i , Eq. 4.5 to 4.7) can be described for the three individual states using the solution of the integral conversion function (Eq. 4.3) to describe the respective two transitions (1) and (2) in IF thermograms. The fractions for the F, the D_1 , and the D_2 state can thus be expressed by Eq. 4.5, Eq. 4.6, and Eq. 4.7, at which the exponential functions model the relative amount of the protein state fraction at the begin of the transition. The respective deviation from one then represents the amount of the denatured protein state:

$$f_F = \exp\left(-\frac{A(1)}{B} A_r(1)\right) \quad (4.5),$$

$$f_{D_1} = 1 - \exp\left(-\frac{A(1)}{B} A_r(1)\right) - \left(1 - \exp\left(-\frac{A(2)}{B} A_r(2)\right)\right) \quad (4.6),$$

$$f_{D_2} = 1 - \exp\left(-\frac{A(2)}{B} A_r(2)\right) \quad (4.7).$$

The linear regions for the three states of the sigmoidal curve can be described by Eq. 4.8, where m_i is the slope and c_{i0} the initial state signal of the linear equation for the F, D_1 , and D_2 state:

$$Y_i = m_i T + c_{i0} \quad (4.8).$$

The resulting fitting function describing the two apparent transitions of mAb unfolding as irreversible reactions is given in Eq. 4.9:

$$\begin{aligned} y = & \exp\left(-\frac{A(1)}{B}A_r(1)\right)(T \cdot m_F + c_{F0}) \\ & + \left(1 - \exp\left(-\frac{A(1)}{B}A_r(1)\right) - \left(1 - \exp\left(-\frac{A(2)}{B}A_r(2)\right)\right)\right)(T \cdot m_{D_1} + c_{D_10}) \\ & + \left(1 - \exp\left(-\frac{A(2)}{B}A_r(2)\right)\right)(T \cdot m_{D_2} + c_{D_20}) \quad (4.9). \end{aligned}$$

Eq. 4.9 was used to fit the IF unfolding profiles of the mAb samples recorded by the NES. These fits yield to the respective apparent E_a value from the mAb transitions. The E_a values were determined from two independent fits of a duplicate measurement as an average value. Errors are reported as standard deviations.

Differential scanning calorimetry (DSC)

To determine unfolding profiles and assign IF unfolding transitions to certain domains of the mAb, DSC measurements were performed on either capillary based devices (automated MicroCal PEAQ-DSC[®] and automated MicroCal VP-capillary-DSC[®], Malvern Instruments, Malvern, UK) or with a DSC device based on a measuring cell (MicroCal VP-DSC[®], Malvern Instruments, Malvern, UK). Analyses were performed at a heating rate of 1 K·min⁻¹ and a mAb concentration of about 1 mg·ml⁻¹ to 2 mg·ml⁻¹ and subsequently evaluated with the exact concentration. After subtracting the thermogram of the respective formulation from the sample thermogram and performing baseline subtraction, the DSC thermogram was generated. Due to a low sample throughput of DSC, measurements were only performed for one buffer for each mAb (mAb1 variants, mAb2 to mAb8, mAba to mAbh, mAb9 variants in F1, and mAb10 variants in citrate buffer). The measuring cell based VP-DSC was used for the six mAb1 variants, mAb2, mAb3, the three mAb9 variants and mAbf for comparison to a capillary based DSC method. For mAb8 and the mAb10 variants, the capillary based VP-capillary-DSC device was used (DSC data obtained from Boehringer Ingelheim). For the remaining mAbs formulated in F1 the capillary based PEAQ-DSC device was

used (DSC data of mAb4 and mAb5 obtained from Boehringer Ingelheim). A comparison and compilation of the DSC thermodynamics can be found under the subtopic of Chapter III in the Appendix.

4.4 Results

Kinetic and thermodynamic characterization of various mAb formulations

To determine kinetic and thermodynamic parameters from the IF thermograms using the apparent three-state models, the individual unfolding profiles of various mAbs in the four different formulations (F1, F2, F3, and citrate buffer) were measured by the Prometheus and the NES. As control and to classify certain IF unfolding profiles to clusters, DSC was performed. According to the IF profile and the mAb domains involved in transitions, it is possible to cluster them in four IF unfolding clusters. For each cluster, an exemplary IF unfolding profile of a mAb in F1 formulation is shown Fig. 4.1.

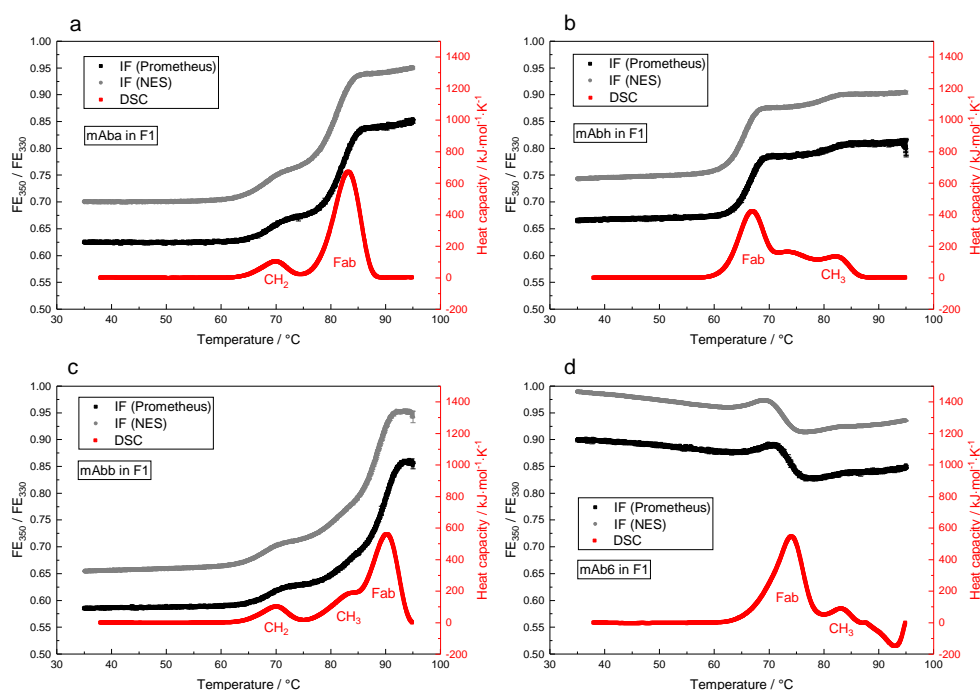


Fig. 4.1: IF and DSC unfolding profiles of the four unfolding clusters. Temperature dependent IF unfolding profiles were both determined in duplicate using the NES (gray) and the Prometheus instrument (black) at a heating rate of $1 \text{ K} \cdot \text{min}^{-1}$. The profiles are classified into four categories. Examples for the different types of unfolding profiles appearing for the mAbs used in this study are shown. For comparison and to assign the IF transitions to certain mAb domains, DSC, as single determination, are shown (red).

The IF thermograms of four different IgG1 molecules (Fig. 4.1) are recorded with the Prometheus instrument (black profile) or the NES (gray profile). When comparing the two unfolding profiles for each mAb, it can be observed that the curves are similar in their shape. However, the profiles recorded by the NES show an offset in the FE_{350}/FE_{330} ratio compared to the IF profiles recorded by the Prometheus. Nonetheless, the presented four different types of IF unfolding profiles can be categorized by taking the profiles to DSC thermograms in account (red profile). The two apparent IF transitions of mAb_a in F1 (Fig. 4.1a) can be assigned to the CH₂-domain (first transition) and the Fab (second transition). For IgG1 molecules, the largest signal in DSC thermograms stems from the unfolding of the Fab and the CH₂-domain unfolding process can be assigned by means of the respective temperature [17, 58, 60]. In contrast, mAb_b in F1 (Fig. 4.1b) shows Fab unfolding within the first transition concluded from DSC, while the transition above 80 °C can be assigned to the CH₃-domain [58]. The IF profiles of mAb_a and mAb_b have in common that two transitions are clearly discernible, while for mAb_b in DSC an additional shoulder after the Fab transition can be observed. However, this transition is not resolved in the IF profiles, so that a three-state model can be applied to fit the IF profile both for mAb_a and mAb_b. In Fig. 4.1c, three transitions can be observed both in IF and DSC thermograms so that mAb_b seems to show an unfolding behavior according to a four-state model. By comparing the IF profile of mAb_b to the DSC measurement, the third transition at about 90 °C can be assigned to the Fab unfolding. Such a DSC profile has also been reported in [17]. The first transition can be assigned to the CH₂-domain and the second one to the CH₃-domain due to the fact that usually in IgG1 molecules the CH₂-domain shows a transition at a lower temperature than the CH₃-domain [58]. The IF unfolding profile in Fig. 4.1d does not show a sigmoidal character of the unfolding transitions. In the case of mAb₆ in F1, the IF thermogram shows a wave-shaped profile, showing the Fab unfolding at about 74 °C deduced from the largest signal in DSC. The second transition above 80 °C can be assigned to the CH₃-domain. The four different IF profiles shown in Fig. 4.1 are examples for all used mAbs in this chapter and the remaining mAbs in the four different formulations can be classified accordingly (Tab. 4.1).

Tab. 4.1: mAb IF profiles classified according to category 1 to 4. The various mAbs are categorized based on their appearing IF unfolding profile, recorded at $1 \text{ K}\cdot\text{min}^{-1}$, into one of the four categories (exemplarily shown for one mAb from each category in Fig. 1). For mAb formulations shown in brackets classified to category 2, a reliable kinetic and/or thermodynamic three-state fit was not possible, because of the presence of a very small second transition. Therefore, these mAb formulations as well as those assigned to category 4 are not further considered in this chapter.

Category 1: profile like mAb _a -F1 (Fig. 4.1a)	mAb _a , mAb _c , mAb _d , mAb _f , mAb _g , mAb _{1b} , mAb ₂ , mAb ₄ , mAb ₅ in F1, F2, F3, and citrate buffer, respectively. mAb _e in F1, F2, and F3. mAb _{10a} , mAb _{10h} , mAb _{10b} and mAb _{10d} in citrate buffer.
Category 2: profile like mAb _h -F1 (Fig. 4.1b)	mAb _h , mAb ₁ , mAb _{1a} , mAb _{1c} , mAb _{1d} , mAb _{1e} in F1, F2, F3, and citrate buffer, respectively. mAb ₃ in F2 and citrate buffer; mAb _{9b} in F1, F3, and citrate buffer and mAb _{9a} in citrate buffer. (mAb ₇ in F1, F2, F3, and citrate buffer; mAb ₃ in F1 and F3; mAb _{9b} in F2)
Category 3: profile like mAb _b -F1 (Fig. 4.1c)	mAb _b in F1, F2, F3 and citrate buffer. mAb ₁₀ , mAb _{10c} , mAb _{10e} , mAb _{10f} , mAb _{10g} and mAb _{10i} in citrate buffer
Category 4: profile like mAb ₆ -F1 (Fig. 4.1d)	mAb ₆ and mAb ₈ in F1, F2, F3, and citrate buffer. mAb ₉ in F1, F2, F3, and citrate buffer and mAb _{9a} in F1, F2, and F3.

The apparent irreversible three-state function determining activation energies (Eq. 4.9) as well as the apparent reversible three-state function (Eq. 3.3 (Chapter III)) determining van't Hoff enthalpies, can be used to fit the apparent two transitions in the IF unfolding profiles of category 1 and 2. The three-state models have to be used two times to fit the three transitions of the four-state IF unfolding profiles in category 3. The IF unfolding profiles of category 4 do not match the sigmoidal character of the three-state fit function and cannot be used for a reliable characterization of those wave-shaped IF thermograms. The fits of the first three categories are exemplarily presented for formulation F1 in Fig. 4.2 using the reversible three-state model (Eq. 3.3 (Chapter III)). The fits of all four formulations for these mAbs can be found in Fig. A.4.1 in the Appendix.

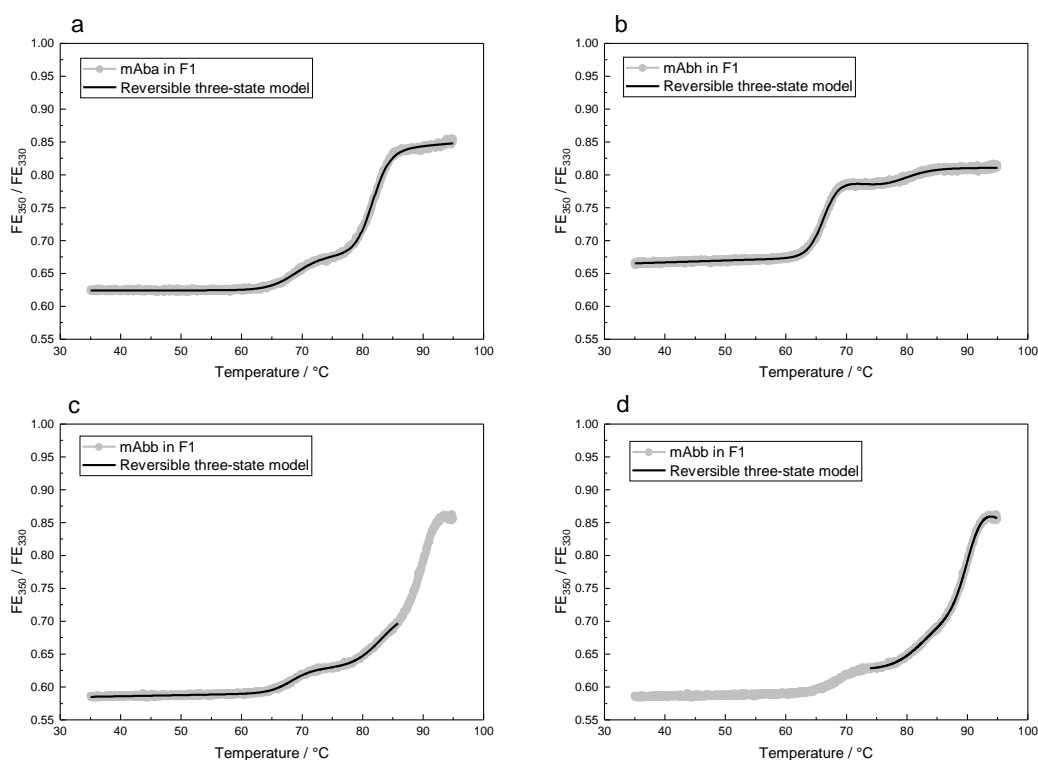


Fig. 4.2: IF unfolding profiles recorded by the Prometheus instrument. The apparent reversible three-state model (Eq. 3.3 (Chapter III)) was used to fit mAba as an example of category 1 (a) and mAbh exemplarily for category 2 (b). For category 3 (mAbb), two three-state fits were used to determine the unfolding thermodynamics (c and d). All respective variables of the fits are depicted in Tab. A.4.2 (Appendix). IF profiles were recorded at $1 \text{ K}\cdot\text{min}^{-1}$.

The reversible three-state model (Eq. 3.3 (Chapter III)) was used to fit the apparent two transitions of mAba and mAbh both in F1 formulation (Fig. 4.2a and b). For most mAbs of category 1 that show Fab unfolding within the second transition, the slope of the linear region of the intermediate state was fixed to zero to have a consistent fitting of the two slightly overlapping transitions. For the mAbs assigned to category 2, showing Fab unfolding within the first transition, T_m values for the second transition often had to be fixed to the transition midpoint to obtain best fitting. Finally, mAbs are categorized into category 3 showing a four-state unfolding behavior with three sigmoidal transitions. To account for such an unfolding profile and determine thermodynamic parameters, the three-state model was applied twice consecutively to fit the first and second transition within the lower temperature range (Fig. 4.2c) and the second and third transition at increased temperatures (Fig. 4.2d). To have a consistent approach for this approximation, the slopes of the linear region separating the first and

second as well as the second and third transition were fixed to zero. This approach accounts for the incompletely separated transitions. All assumptions made for thermodynamic fitting are summarized in Tab. A.4.1 and for each mAb an IF thermogram in one formulation is exemplarily depicted in Fig. A.4.3 to Fig. A.4.8 (Appendix).

The irreversible three-state fits (Eq. 4.9) applied to the mAbs are exemplarily shown for the mAbs in F1 of category 1, 2, and 3 in Fig. 4.3. For these mAbs, the IF thermograms, recorded at $1 \text{ K}\cdot\text{min}^{-1}$, and the fit functions of the irreversible three-state model are shown for all four formulations in Fig. A.4.2 (Appendix).

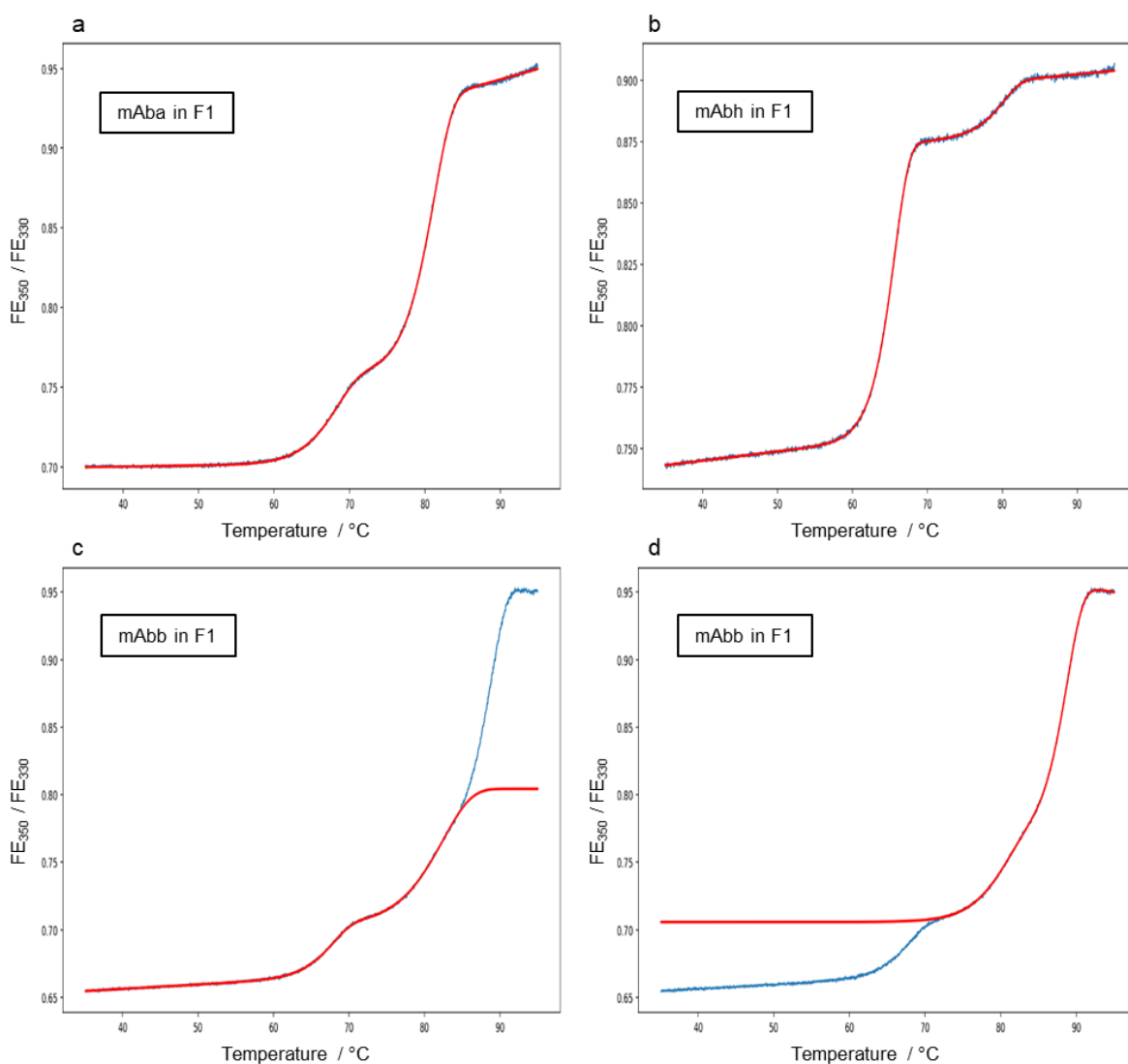


Fig. 4.3: IF unfolding profiles recorded by the NES. The apparent irreversible three-state model (Eq. 4.9, red line) was used to fit mAba as an example of category 1 (a) and mAbh exemplarily for category 2 (b). For category 3 (mAbb) (c, d), two three-state fits were used to determine the unfolding kinetics. All respective variables of the fits are depicted in Tab. A.4.2 (Appendix). IF profiles (blue curve) were recorded at $1 \text{ K}\cdot\text{min}^{-1}$.

The three categories were fitted in a similar manner as described for the reversible fitting model, with exception of category 2 (Fig. 4.3b). Profiles of this category can often be fitted with no fixed variables. All assumptions made are summarized in Tab. A.4.1 and one IF thermogram and the respective irreversible three-state fit function of each mAb is shown in Fig. A.4.9 to Fig. A.4.15 (Appendix).

The different mAb formulations following an IF unfolding profile assigned to category 1, 2, and 3 were investigated regarding their thermodynamic and kinetic properties. Therefore, the reversible three-state fitting model (Eq. 3.3 (Chapter III)) was used to determine ΔH_{vh} from IF unfolding profiles recorded by the Prometheus device. To investigate activation energies, IF unfolding profiles recorded by the NES were fitted using the irreversible three-state model (Eq. 4.9). E_a and ΔH_{vh} values for the different mAb formulations are illustrated in Fig. 4.4, where the three different domains of the mAbs (CH₂, CH₃, and Fab) appear in their IF unfolding profile. All values of E_a and ΔH_{vh} are summarized in Tab. A.4.3 (Appendix).

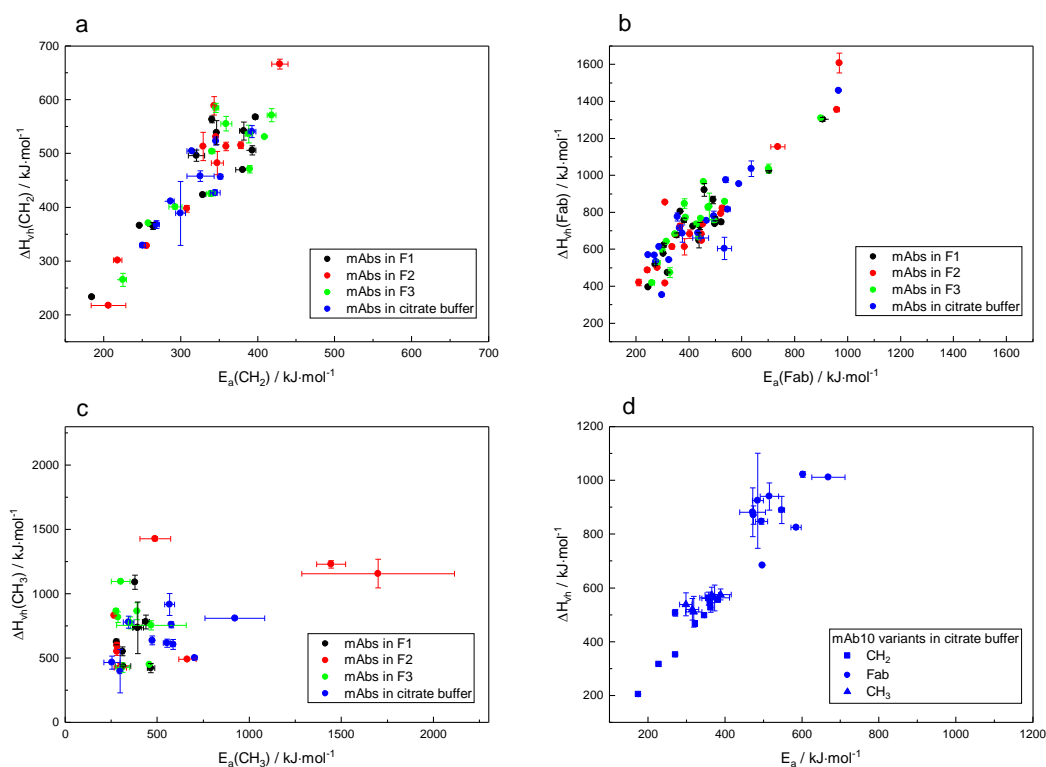


Fig. 4.4: ΔH_{vh} against E_a . For the CH₂-domain (a), Fab (b), CH₃-domain (c), ΔH_{vh} is plotted against E_a . The different formulations are illustrated in black (F1), red (F2), green (F3), and blue (citrate buffer). In plot (d), the thermodynamics and kinetics of the mAb10 variants in citrate buffer are illustrated. ΔH_{vh} values of the mAb1 variants in citrate buffer were adapted from Chapter III. All values were determined from IF thermograms at a heating rate of 1 K·min⁻¹.

In Fig. 4.4, ΔH_{vh} and E_a values are illustrated for the three different domains of the mAbs. From Fig. 4.4a and b, it can be concluded that ΔH_{vh} as well as E_a values for the CH₂-domain and for the Fab are different between different mAbs within one formulation. Therefore, E_a and ΔH_{vh} can be used to discriminate thermodynamic and kinetic properties of different mAbs. Moreover, in Fig. 4.4a and b one can see that ΔH_{vh} is generally larger than the respective E_a value and a linear increase of ΔH_{vh} with rising E_a . Analyzing the impact of the four different formulations on the mAbs, no unique trend can be observed for the CH₂-domain, which can be concluded that no formulation is clustered in a certain area in Fig. 4.4a. Therefore, the four formulations cannot be discriminated when inspecting the CH₂-domain transition. In contrast, a trend for higher $E_a(\text{Fab})$ and $\Delta H_{vh}(\text{Fab})$ values for F1 and F3 formulation compared to F2 and the citrate buffer can be observed for most of the mAbs (Fig. 4.4b). Therefore regarding Fab unfolding, formulation F1 and F3 differ from formulation F2 and citrate buffer in their impacts on the thermodynamic and kinetic properties of the different mAbs. For the CH₃-domain shown in Fig. 4.4c, the mAbs show clustered values and a linearly increasing trend between ΔH_{vh} and E_a cannot be observed. In Fig. 4.4d, the ΔH_{vh} and E_a values from the ten mAb10 variants in citrate buffer are illustrated. The differences in the CH₂-domain between the variants are more pronounced than those values determined from the CH₃-domain, which show no large differences. For the Fab of the mAb10 variants, differences between ΔH_{vh} and E_a can be observed for the variants but are not as pronounced as for the CH₂-domain. The determination of ΔH_{vh} and E_a for the CH₂- and CH₃-domain and for the Fab illustrates that the variants of mAb10 within one formulation can be discriminated by their thermodynamic and kinetic parameters of the CH₂-domain and the Fab, while the parameters of the CH₃-domain show similar values.

In summary, the reversible and irreversible three-state models can be used to fit the IF unfolding profile of mAbs showing two sigmoidal unfolding transitions. For mAbs showing three IF transitions in their unfolding profiles with a sigmoidal shape, the three-state models can be used two times to describe the transitions consecutively. A wave-shaped profile shown for mAb6 is not described by the two fit functions. The thermodynamic and kinetic parameters are considered as unreliable because the used fit functions do not mirror the shape of those profiles. The determination of E_a and ΔH_{vh} values for the IF unfolding transitions results in different magnitudes for the CH₂-domain and the Fab unfolding, with a general trend that a larger ΔH_{vh} is connected

to a larger E_a . For the CH₃-domain, a clustering of the thermodynamic and kinetic parameters can be observed with higher uncertainties of the values and with no clear trend for the different mAbs.

Predicting thermal stability via thermodynamic and kinetic parameters

Following the investigation on the general trend of thermodynamic and kinetic parameters for several mAb formulations, the determined ΔH_{vh} and E_a values from the IF profiles were tested to correlate with thermal stability. For comparison, the correlation between thermal stability and T_m values, determined as inflection points of the IF unfolding transitions, were investigated. The parameters used as well as thermal stability of the mAbs are summarized in Tab. A.4.3 (Appendix).

Hence, for mAba to mAbg, mAb4, and mAb5 in F1, F2, and F3 formulation, the monomer loss, the aggregate content increase, and the fragment content increase after four weeks of thermal incubation at 25 °C and 40 °C were investigated by SEC analyses and tested to correlate with the determined E_a , ΔH_{vh} , and T_m values. All investigated mAbs show the CH₂-domain unfolding within the first transition, while the Fab unfolds within the second transition (category 1), with exception of mAbb which shows the Fab unfolding during the third transition (category 3). For the thermal induced stress at 25 °C, the correlation plots are presented in Fig. 4.5.

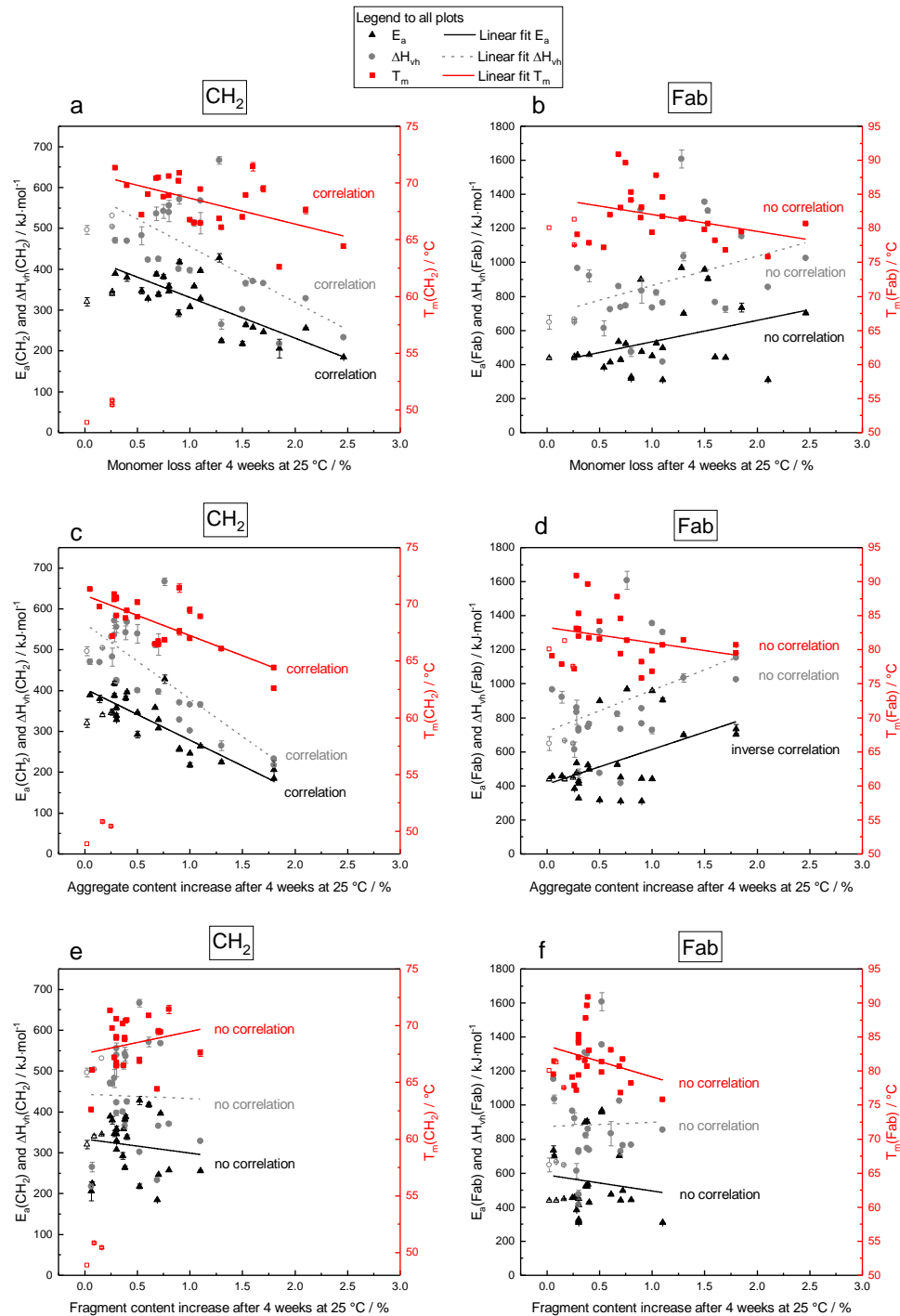


Fig. 4.5: Correlation plots of mAba to mAbg and mAb4 formulated in F1, F2, and F3 at 25 °C. The predictive parameters (E_a , ΔH_{vh} , T_m) of the CH₂-domain (a, c, e) and the Fab (b, d, f) are plotted against the monomer loss (a, b), the aggregate content increase (c, d) and the fragment content increase (e, f) at 25 °C. Linear regressions were applied and an analysis of variance (ANOVA) test was used to investigate the significance of the slope being different from zero. From the ANOVA test, it is concluded if the predictive parameters show a correlation with thermal stability or not. Data for mAb5 (depicted by open symbols) are not considered for statistical analyses due to their distinct lower $T_m(1)$ values of about 50 °C falsifying the statistical result. All predictive parameters are deduced from IF thermograms at 1 K·min⁻¹.

In Fig. 4.5, the different predictive parameters (E_a , ΔH_{vh} , T_m) for mAba to mAbg and mAb4 in formulation F1, F2, and F3 are plotted against monomer loss and against the increase of aggregate and fragment content after four weeks of incubation at thermal stress at 25 °C. Linear fits were applied to investigate the overall correlation between the predictive parameters and thermal stability. A negative slope of the linear fits (Fig. 4.5) indicates an elevated monomer loss and a higher increase in aggregate and fragment contents for lower values of ΔH_{vh} , E_a , and T_m . To investigate if the slopes are significantly different from zero, an analysis of variance (ANOVA) test was applied. From the ANOVA parameters (Tab. A.4.4, Appendix), it can be concluded which predictive parameter is correlated with thermal stability at 25 °C. For the monomer decrease, E_a , ΔH_{vh} , and T_m of the CH₂-domain transition show a negative slope significantly different from zero. Therefore, these parameters are interpreted to have a correlation with monomer decrease. The parameters deduced from the Fab unfolding do not show a correlation. Investigating the aggregate content increase, $E_a(\text{CH}_2)$, $\Delta H_{vh}(\text{CH}_2)$, and $T_m(\text{CH}_2)$ show a correlation, while $E_a(\text{Fab})$ shows an inverse correlation with aggregate content increase. The inverse correlation is not expected and could be explained by a high spreading around the linear regression. This claim can be substantiated by the fact that this inverse correlation plot shows the lowest R-square compared to the remaining plots showing a correlation. The fragment content increase for the assessed mAbs is not correlated with any of the predictive parameters of both transitions. The correlation plots of mAba to mAbg and mAb4 in formulation F1, F2, and F3 are analyzed for the three formulations together to provide an overall trend which predictive parameter is correlated with thermal stability for a broader range of conditions and samples. However, conformational and colloidal properties of the different formulations can influence the outcome of the analysis. To investigate if the different mAbs can also be discriminated within one formulation, the predictive parameters showing a correlation were analyzed separately for F1, F2, and F3 (linear plots are not shown). Results from the separately determined linear fit parameters are shown in Tab. A.4.4 (Appendix). For the mAbs within one formulation, the three predictive parameters of the CH₂-domain show the most number of linear correlation plots with the F1 formulation, followed by the F3, and F2 formulation.

To further investigate the thermal stability of mAba to mAbg and mAb4 in F1, F2, and F3, the predictive parameters were tested to correlate with thermally induced stress after incubating the mAb samples for four weeks at 40 °C. Therefore, the thermodynamic and kinetic parameters are plotted against monomer loss, aggregate, and fragment content increase determined by SEC (Fig. 4.6).

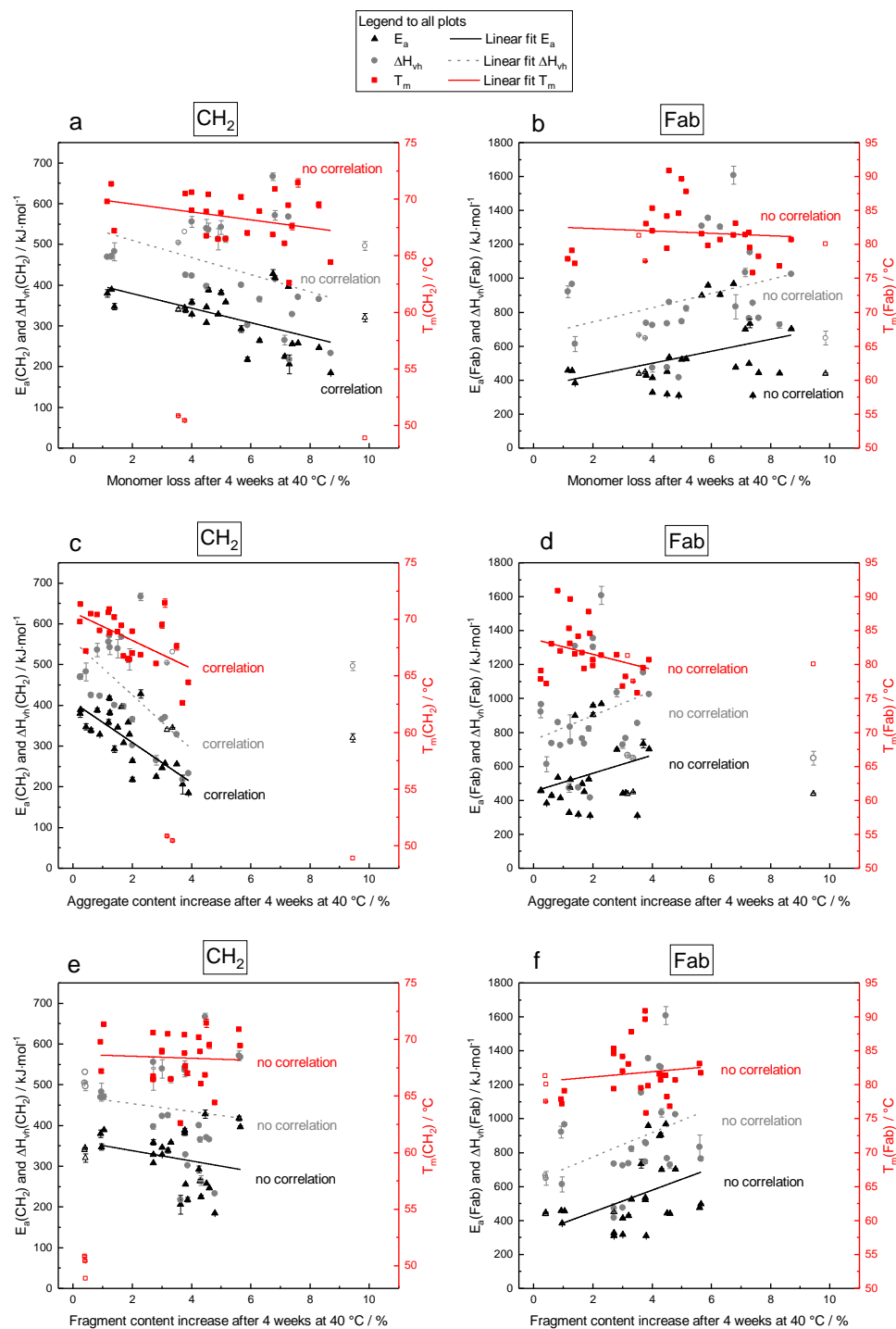


Fig. 4.6: Correlation plots of mAb_a to mAb_g and mAb₄ formulated in F1, F2, and F3 at 40 °C. The predictive parameters (E_a , ΔH_{vh} , T_m) of the CH₂-domain (a, c, e) and the Fab (b, d, f) are plotted against the monomer loss (a, b), the aggregate content increase (c, d) and the fragment content increase (e, f). Linear regressions and ANOVA were applied to investigate the significance of the slope being different from zero. From the ANOVA test, it is concluded if the predictive parameters show a correlation with thermal stability or not. Data for mAb₅ (depicted by open symbols) are not considered for statistical analysis due to their low $T_m(1)$ of about 50 °C and an onset temperature of the first unfolding transition that is close to the incubation temperature of 40 °C leading to high uncertainties by investigating the thermal stability. All predictive parameters are deduced from IF thermograms recorded at 1 K·min⁻¹.

In Fig. 4.6, linear fits were applied to the different thermodynamic and kinetic parameters for the CH₂-domain, the Fab, and the data derived from SEC. Applying ANOVA (results summarized in Tab. A.4.5, Appendix), the monomer loss for the assessed mAbs in formulation F1, F2, and F3 at 40 °C is correlated with E_a determined from the CH₂-domain transition. ΔH_{vh} and T_m of this transition do not show a correlation. The three predictive parameters of the CH₂-domain transition correlate with the aggregate content increase, while a correlation with the increase of fragment content cannot be found. For the predictive parameters describing the Fab transition, no correlation with thermal stability is found. By analyzing the correlations for the mAbs separately within F1, F2, and F3 (linear regressions not shown), a correlation between monomer decrease and E_a(CH₂) cannot be evaluated (Tab. A.4.5, Appendix). For the aggregate content increase, a correlation for mAbs in formulation F1 is found for E_a(CH₂), ΔH_{vh}(CH₂), and T_m(CH₂), while these parameters do not show a correlation with the aggregate content increase determined from the mAbs in formulation F2. The increase of aggregate content for mAbs in F3 only shows a correlation with E_a(CH₂).

To further broaden our understanding of the correlation between thermal stability and the determined predictive parameters in this chapter, thermal stability of the mAb10 variants (mAb10 to mAb10i) formulated in citrate buffer were tested to correlate with their thermodynamic and kinetic parameters from the IF unfolding transitions. Therefore, the monomer loss and the increase of aggregate and fragment contents after about 26 weeks of thermal incubation at 40 °C were tested to correlate with the values of E_a, ΔH_{vh}, and T_m for the CH₂-domain and the Fab. For these IF unfolding transitions, differences can be observed for the thermodynamic and kinetic parameters discriminating the mAb10 variants (Fig. 4.4d). The plots for thermal stability and the predictive parameters are shown in Fig. 4.7.

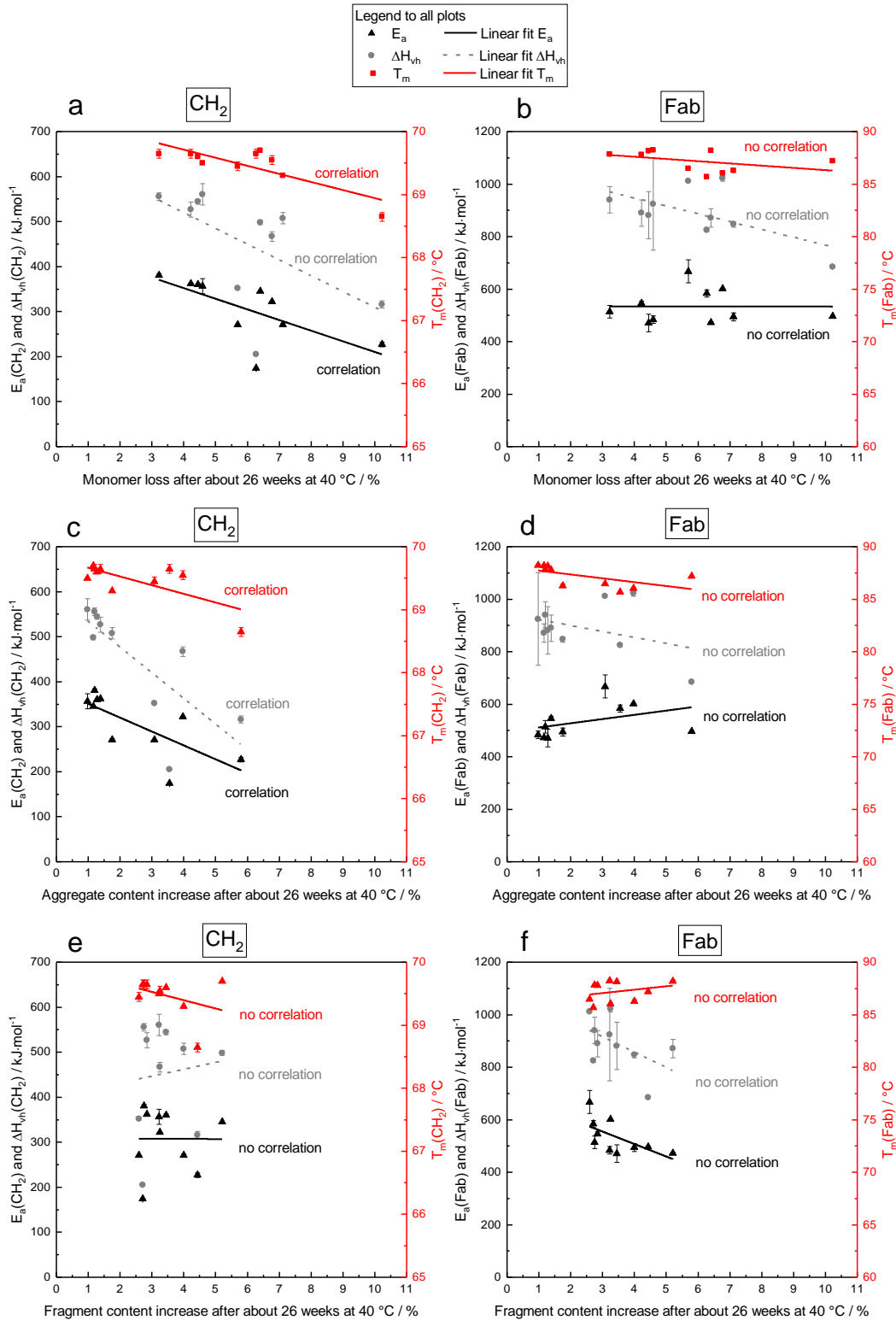


Fig. 4.7: Correlation plots of the mAb10 variants solved in citrate buffer at 40 °C. Predictive parameters (E_a , ΔH_{vh} , T_m) of the CH_2 -domain (a, c, e) and the Fab (b, d, f) vs. monomer loss (a, b), the aggregate content increase (c, d) and the fragment content increase (e, f). Linear regressions and ANOVA was used to investigate if the predictive parameters show a correlation with thermal stability or not. All predictive parameters are deduced from IF thermograms recorded at 1 K \cdot min $^{-1}$.

The respective fit parameters from the linear regressions and ANOVA are summarized in Tab. A.4.6 (Appendix). For the mAb10 variants which are all formulated in citrate buffer, the monomer decrease is correlated with $E_a(\text{CH}_2)$ and $T_m(\text{CH}_2)$, while the remaining predictive parameters for the CH_2 -domain and the Fab are not correlated with monomer loss (Fig. 4.7). The aggregate content increase is correlated with all predictive parameters for the CH_2 -domain, while the Fab does not show a correlation. The increase in fragment content does not significantly correlate with any of the predictive parameters. It can be concluded for the mAb10 variants that the monomer loss and increase of the amount of aggregates are correlated with the predictive parameters derived from the CH_2 -domain unfolding. For this unfolding transition, E_a and T_m show a slightly better correlation than ΔH_{vh} .

The irreversible three-state model (Eq. 4.9) determining E_a values from IF unfolding experiments was also tested for the mAb1 variants in Chapter III. In Chapter III, a thermal stability monomer ranking at 40 °C was reported for these variants as follows: mAb1b > mAb1a > mAb1e > mAb1 ~ mAb1d > mAb1c. These mAbs show Fab unfolding within the first transition (except for mAb1b), so the signal of the CH_2 -domain is overlaid by the one from the Fab and cannot be assessed. Therefore, the reported stability ranking is only compared to the activation energy of the Fab transitions. The determination of $E_a(\text{Fab})$ leads to the following ranking with the respective average and standard deviation values for $E_a(\text{Fab})$: mAb1b ($375 \pm 2 \text{ kJ}\cdot\text{mol}^{-1}$) > mAb1a ($364 \pm 0 \text{ kJ}\cdot\text{mol}^{-1}$) > mAb1 ($325 \pm 1 \text{ kJ}\cdot\text{mol}^{-1}$) > mAb1e ($288 \pm 4 \text{ kJ}\cdot\text{mol}^{-1}$) > mAb1c ($275 \pm 1 \text{ kJ}\cdot\text{mol}^{-1}$) > mAb1d ($246 \pm 0 \text{ kJ}\cdot\text{mol}^{-1}$) (IF fits not shown). An ANOVA analysis for $E_a(\text{Fab})$ as performed above would not result in a significantly negative slope due to monomer decrease which could be explained by the small number of mAb1 variants (ANOVA data not shown). However, a qualitative comparison of the rankings would give no large discrepancies.

In summary, thermodynamic and kinetic parameters were tested to correlate with thermal stability at 25 °C and/or 40°C. The predictive parameters of the CH_2 -domain determined for mAb4a to mAb4g and mAb4 in formulations F1, F2, and F3 and the mAb10 variants in citrate buffer show most correlations with monomer loss and aggregate content increase, while no correlation can be analyzed for the increase of fragment content. The respective values of E_a show higher accordance to thermal stability than ΔH_{vh} and T_m values of the CH_2 -transition. A correlation of the predictive

parameters derived from the Fab transitions to thermal stability is not observed for these mAbs. In contrast, the derived E_a values of the Fab transition match the thermal stability ranking of the mAb1 variants in citrate buffer qualitatively and a correlation between $\Delta H_{vh}(\text{Fab})$ and monomer loss can even be determined quantitatively (ANOVA data not shown).

Determination of activation energies at fast heating rates

As described above, activation energies were determined from IF unfolding profiles at a slow heating rate of $1 \text{ K}\cdot\text{min}^{-1}$ using the NES. However, the NES can also be used to perform heating rate dependent unfolding experiments spanning from $1 \text{ K}\cdot\text{min}^{-1}$ up to $30 \text{ K}\cdot\text{min}^{-1}$. Therefore, the NES was used to record IF unfolding profiles at faster heating rates of $18 \text{ K}\cdot\text{min}^{-1}$ and $30 \text{ K}\cdot\text{min}^{-1}$ and determine values of E_a from these profiles using the irreversible three-state model (Eq. 4.9). Fitting was performed in a similar manner as described for $1 \text{ K}\cdot\text{min}^{-1}$ (compare Tab. A.4.1 in the Appendix). Exemplarily, the fitted IF unfolding profile of mAba formulated in F1 at $18 \text{ K}\cdot\text{min}^{-1}$, $30 \text{ K}\cdot\text{min}^{-1}$, and $1 \text{ K}\cdot\text{min}^{-1}$, for comparison, are shown in Fig. 4.8.

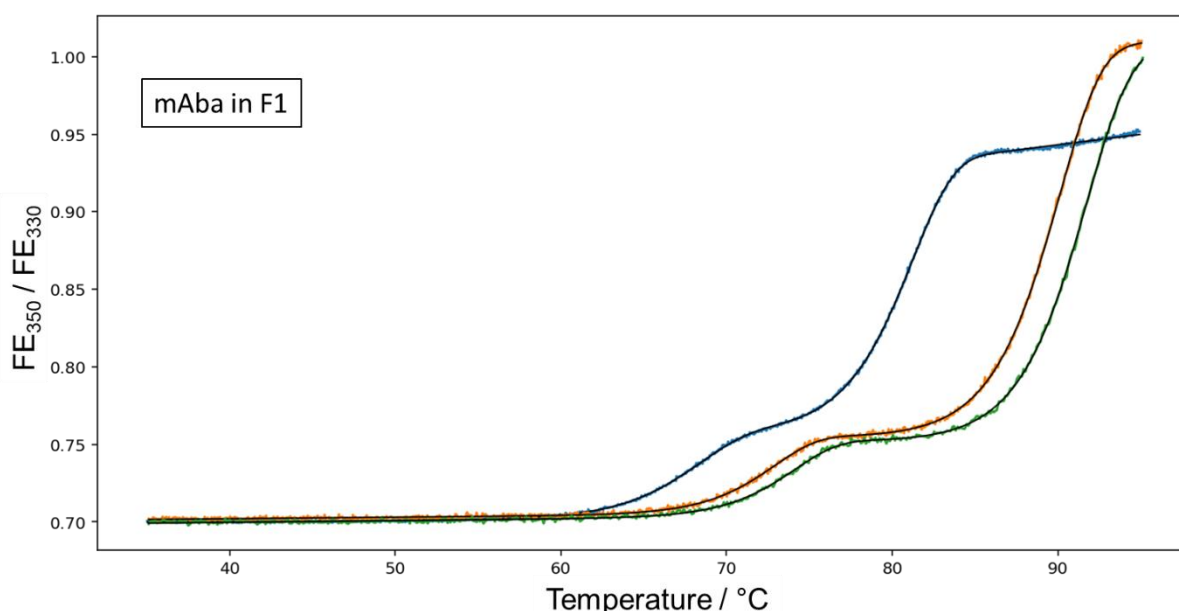


Fig. 4.8: Heating rate dependent IF thermograms of mAba in F1. The FE_{350}/FE_{330} ratio was recorded at $1 \text{ K}\cdot\text{min}^{-1}$ (blue), $18 \text{ K}\cdot\text{min}^{-1}$ (yellow), and $30 \text{ K}\cdot\text{min}^{-1}$ (green) and are plotted against the temperature. The irreversible three-state fit function (Eq. 4.9, black line) was used to determine values of E_a from the respective transitions. Shown is one profile of a duplicate measurement, respectively.

As Fig. 4.8 illustrates, Eq. 4.9 can be used to fit the IF profiles at faster heating rates. Moreover, the transitions shift to higher temperatures for faster heating rates, which can be observed for all investigated mAbs. Among other things, this property is described and discussed in Chapter V. However, as explained before, mAb_a can be ranked to category 1 so that the first transition refers to the CH₂-domain, while the second transition stands for the Fab unfolding. Activation energies for mAb_a in F1 were determined as: $E_a(\text{CH}_2) = 329 \pm 1 \text{ kJ}\cdot\text{mol}^{-1}$ and $E_a(\text{Fab}) = 415 \pm 1 \text{ kJ}\cdot\text{mol}^{-1}$ for $1 \text{ K}\cdot\text{min}^{-1}$, $E_a(\text{CH}_2) = 382 \pm 1 \text{ kJ}\cdot\text{mol}^{-1}$ and $E_a(\text{Fab}) = 432 \pm 6 \text{ kJ}\cdot\text{mol}^{-1}$ for $18 \text{ K}\cdot\text{min}^{-1}$, $E_a(\text{CH}_2) = 382 \pm 3 \text{ kJ}\cdot\text{mol}^{-1}$ and $E_a(\text{Fab}) = 426 \pm 4 \text{ kJ}\cdot\text{mol}^{-1}$ for $30 \text{ K}\cdot\text{min}^{-1}$. $E_a(\text{CH}_2)$ shows increased values for the faster heating rates, while $E_a(\text{Fab})$ shows similar values between the heating rates, with a slightly decreased value for $1 \text{ K}\cdot\text{min}^{-1}$.

To investigate the predictive character of activation energies determined from fast heating rates, correlations between values of E_a and thermal stability were determined as described above. For this purpose, thermal stability parameters showing a correlation with activation energy determined at $1 \text{ K}\cdot\text{min}^{-1}$ were tested to correlate with values of E_a at $18 \text{ K}\cdot\text{min}^{-1}$ and $30 \text{ K}\cdot\text{min}^{-1}$. The correlation plots between thermal stability and E_a at faster heating rates are depicted for mAb_a to mAb_g and mAb₄ in Fig. 4.9. For comparison, the correlation plots of $1 \text{ K}\cdot\text{min}^{-1}$ are also shown in this figure. All parameters derived from ANOVA can be found in Tab. A.4.7 (Appendix).

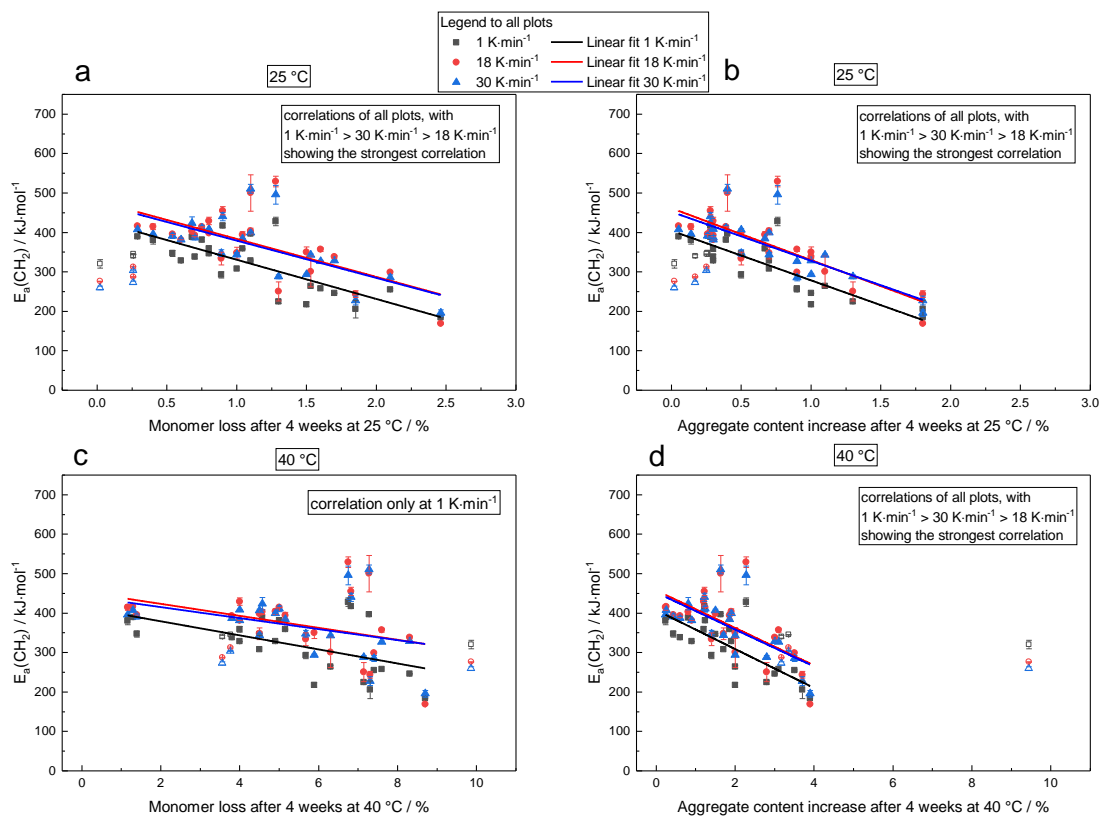


Fig. 4.9: Correlation plots of mAb4 to mAbg and mAb4 formulated in F1, F2, and F3. $E_a(\text{CH}_2)$ values determined at a heating rate of $1 \text{ K}\cdot\text{min}^{-1}$ (black), $18 \text{ K}\cdot\text{min}^{-1}$ (red), and $30 \text{ K}\cdot\text{min}^{-1}$ (blue) are plotted against monomer loss and aggregate content increase at $25 \text{ }^\circ\text{C}$ (a, b) and against monomer loss and aggregate content increase at $40 \text{ }^\circ\text{C}$ (c, d). Values are reported as mean and standard deviation of a duplicate measurement. Data for mAb5 are not considered for statistical analysis due to the close onset temperature of the first unfolding transition to the incubation temperature of $40 \text{ }^\circ\text{C}$. mAb5 samples are depicted by open symbols.

Analyzing Fig. 4.9, $E_a(\text{CH}_2)$ values shift to increased values determined for $18 \text{ K}\cdot\text{min}^{-1}$ and $30 \text{ K}\cdot\text{min}^{-1}$ compared to those values derived from $1 \text{ K}\cdot\text{min}^{-1}$. Values for the Fab transition show more similar values determined by the three different rates (Fig. A.4.16, Appendix). Strongest correlations between values of $E_a(\text{CH}_2)$ and thermal stability both at $25 \text{ }^\circ\text{C}$ and $40 \text{ }^\circ\text{C}$ can be determined for IF profiles recorded at a slower heating rate of $1 \text{ K}\cdot\text{min}^{-1}$. Faster heating rates of $18 \text{ K}\cdot\text{min}^{-1}$ and $30 \text{ K}\cdot\text{min}^{-1}$ do not provide better correlations for the tested mAbs. By analyzing the mAbs separately for formulation F1 and F3, strongest correlation of $E_a(\text{CH}_2)$ with thermal stability both at $25 \text{ }^\circ\text{C}$ and $40 \text{ }^\circ\text{C}$ can be determined for a heating rate of $1 \text{ K}\cdot\text{min}^{-1}$ (data not shown). Similar results can be observed by comparing the correlations between E_a analyzed at different heating rates and thermal stability of the mAb10 variants (Fig. 4.10, ANOVA parameters are listed in Tab. A.4.8 in the Appendix).

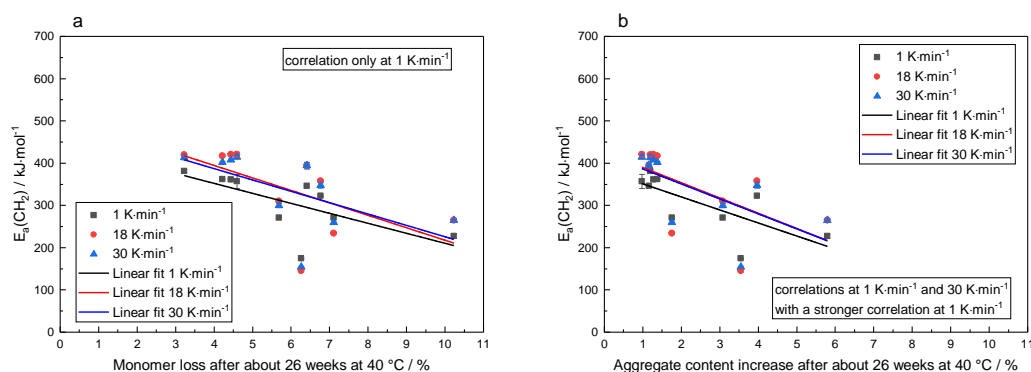


Fig. 4.10: Correlation plots of the mAb10 variants formulated in citrate buffer. $E_a(\text{CH}_2)$ values determined at a heating rate of $1 \text{ K}\cdot\text{min}^{-1}$ (black), $18 \text{ K}\cdot\text{min}^{-1}$ (red), and $30 \text{ K}\cdot\text{min}^{-1}$ (blue) are plotted against monomer loss and aggregate content increase at $40 \text{ }^\circ\text{C}$. Values are reported as mean and standard deviation of a duplicate measurement.

Strongest correlations between $E_a(\text{CH}_2)$ and thermal stability at $40 \text{ }^\circ\text{C}$ can be analyzed for the slowest heating rate of $1 \text{ K}\cdot\text{min}^{-1}$, followed by $30 \text{ K}\cdot\text{min}^{-1}$ and $18 \text{ K}\cdot\text{min}^{-1}$. In summary, strongest correlation between activation energy and thermal stability can be determined for $1 \text{ K}\cdot\text{min}^{-1}$ compared to $18 \text{ K}\cdot\text{min}^{-1}$ and $30 \text{ K}\cdot\text{min}^{-1}$.

4.5 Discussion

Determination of thermodynamic and kinetic parameters

The determination of ΔH_{vh} values using the reversible three-state model (Eq. 3.3) for IF unfolding profiles of mAbs has been discussed in Chapter III. In this chapter, the irreversible three-state fit function (Eq. 4.9) was used to determine activation energies from the respective unfolding transitions in IF thermograms for a range of mAbs. According to the illustrated reaction in Eq. 4a, the irreversible reactions are assigned to originate from a reversible pre-equilibrium. Irreversible reactions are overlaid by this reversible pre-equilibrium [8]. However, to mathematically describe and fit the irreversible reactions using an apparent three-state model, the unfolding reactions were modeled according to Eq. 4c. In contrast, thermodynamics were described according to Eq. 4b, so that the reversible and irreversible three-state model describe both extremes occurring during protein unfolding. Due to the fact that both a reversible pre-equilibrium and an irreversible reaction take place and the respective three-state

functions describe the reaction as fully reversible or irreversible, the kinetic and thermodynamic parameters should be treated as apparent values. However, the magnitude of the determined E_a values agrees with the ones previously reported for other proteins [61, 75, 76]. The agreement of thermodynamics has been discussed in Chapter III and indicates that the partition in reversible and irreversible reactions is suitable for a mathematical description. The proposed and introduced reversible and irreversible three-state model were also applied to fit the IF thermograms showing a four-state unfolding profile according to category 3. For this purpose, the three-state fits were used two times to describe the CH₂-domain as the first transition and the Fab as the third transition. This was done to exceed the three-state models to more kinds of unfolding profiles. Applying an apparent four-state model would increase the complexity and the number of variables of the fit functions disproportionately reducing its applicability. Moreover, it is unlikely that the first and the third transition are influencing each other strongly because the underlying reactions are separated by the second transition. It is unlikely for the first protein state and the fourth state to pass all three transitions at once. Therefore, the apparent four-state IF thermograms can be described in a good approximation by applying two three-state fits for the thermodynamics as well as for kinetics.

Determining thermodynamic and kinetic parameters from the IF unfolding profiles, the general trend is observed that an increased ΔH_{vh} is connected to an increased E_a . This link is determined for the CH₂-domain and the Fab, while the CH₃-domain shows clustered values without a unique trend. The clustered values could be explained with higher uncertainties for the determination of the thermodynamic and kinetic parameters of the CH₃-domain because the IF unfolding transitions of this domain are often very small. Fitting of a small transition is often weighted with higher uncertainties. However, an increase of the values of E_a and ΔH_{vh} observed for the CH₂-domain and the Fab are only a general trend and subtle differences between the two parameters exist, otherwise differences in the predictive character would not be observed. A cause for these differences might be the differences of the fitting functions describing reactions as reversible for ΔH_{vh} and as irreversible for characterizing E_a , whereas both reactions occur during heating. By analyzing the different influences of the formulations, the trend is observed that formulations F1 and F3 show higher ΔH_{vh} and E_a values for the Fab unfolding compared to F2 and citrate buffer. The observed reduction of these parameters might originate from a decreased conformational stability through the

addition of a high concentration of NaCl in the formulation [77]. In addition, the effect of citrate as buffer compound, which was previously seen to reduce E_a values of an IgG1 molecule compared to an acetate buffer, has to be considered [78].

Methodology correlating predictive parameter and thermal stability

The investigations of correlations between decreasing values for the predictive parameters (E_a , ΔH_{vh} , T_m) and decreasing thermal stability were evaluated by applying a linear regression. A significantly negative slope of the linear regression then indicates a predictive quality. For evaluation, it was chosen to analyze the slope of the linear regressions and the significance of the deviation from zero by applying the ANOVA test. In general, low R-square values are determined for those data analyses that do not show a significantly negative slope and therefore no correlation between predictive parameter and thermal stability. When a significantly negative slope is determined, the R-square values are much higher, spanning a range from 0.28 to 0.87. These values are an indicator for a useful method to investigate correlations between predictive parameters and thermal stability. The determined F-values and their respective probability values (Prob>F) deduced from ANOVA clearly distinguish between slopes different from zero or statistically equal to zero. Therefore, the outcome of the ANOVA test was interpreted to give advice if the determined predictive parameters have a correlation with thermal stability or not.

Predictive character of the investigated parameters

For the mAbs tested in this chapter, the predictive parameters derived from the CH₂-domain show a stronger correlation with thermal stability than the parameters derived from the Fab transition. By characterizing the CH₂-domain transition, the determination of E_a shows the largest number of correlating linear regressions with thermal stability compared to ΔH_{vh} and T_m values. Therefore, a stronger correlation of $E_a(\text{CH}_2)$ with thermal stability can be observed compared to the one of ΔH_{vh} and T_m of the CH₂-domain. For Fab unfolding, no significant correlation can be determined between the predictive parameters and the monomer loss or aggregate content increase in this chapter. However, a significantly negative slope between $\Delta H_{vh}(\text{Fab})$ and monomer loss at 40 °C can be observed for the mAb1 variants from Chapter III. It is important to note

that the thermal stability of the mAb1 variants as well as of the mAb10 variants were determined at a lower mAb concentration ($10 \text{ mg}\cdot\text{ml}^{-1}$ and $5 \text{ mg}\cdot\text{ml}^{-1}$) compared to a concentration of $50 \text{ mg}\cdot\text{ml}^{-1}$ for mAba to mAbg and mAb4 in formulations F1, F2, and F3. For the thermal stability data at higher mAb concentration, correlations with $E_a(\text{Fab})$ and $\Delta H_{\text{vh}}(\text{Fab})$ are worse, meaning smaller F-values, compared to the ones at lower mAb concentration. At higher mAb concentrations, colloidal properties have a larger impact on thermal stability of the mAbs compared to lower mAb concentrations causing accelerated aggregation for higher mAb concentrations [5, 12]. Pronounced influence of colloidal properties on thermal stability caused by increased mAb concentrations could also explain the stronger correlations of thermal stability and $E_a(\text{CH}_2)$, in contrast to $\Delta H_{\text{vh}}(\text{CH}_2)$ and $T_m(\text{CH}_2)$. A higher E_a value has been associated with stronger net repulsive protein-protein interactions [78]. Due to the fact that thermal stability at higher mAb concentrations is more and more influenced by colloidal properties, the predictive character of the parameters describing the conformational stability could be reduced. This hypothesis is substantiated by the observations that mAba to mAbg and mAb4 in formulations F1, F2, and F3 at $25 \text{ }^\circ\text{C}$ show a stronger correlation with thermal stability than for $40 \text{ }^\circ\text{C}$. At $40 \text{ }^\circ\text{C}$, the colloids move faster than at $25 \text{ }^\circ\text{C}$ and colloidal influences increase their impacts on stability [79]. Moreover, analyzing correlations between mAbs in a single formulation and thermal stability, best correlation is found for the plane histidine formulation (F1), followed by the F3 histidine formulation containing trehalose, and by the F2 histidine formulation with additional sodium chloride. This is due to the influence of the excipients on the colloidal properties of the formulation [5]: addition of NaCl can lead to a shielding effect of the protein charges, which may result in a reduction of the repulsive forces between the molecules [77]. Consequently, the correlations between all predictive parameters and thermal stability at $50 \text{ mg}\cdot\text{ml}^{-1}$ can be affected by increased colloidal aggregation and can lead to deviations between determined thermal stability and the predictive parameters. Another explanation of the different predictive power observed for the CH_2 -domain and the Fab unfolding parameters could be different aggregation mechanisms triggered by mAbs and their formulations. In various studies, it has been observed that either the CH_2 -domain [61, 80] or the Fab [9, 62, 64] can trigger aggregation. Furthermore, a competing pathway between the CH_2 -domain and the Fab, which is dependent on the pH, has been reported before [63]. These findings emphasize the complex aggregation mechanisms occurring for different antibodies and formulation conditions and substantiate the need

to characterize and determine different predictive parameters such as E_a , ΔH_{vh} and T_m for both, the CH₂-domain and the Fab transition.

Determination of activation energies at slow and fast heating rates

By comparing values of E_a determined from IF profiles recorded at slow and fast heating rates, increased values for $E_a(\text{CH}_2)$ can be determined from faster heating rates. For $E_a(\text{Fab})$, similar values can be analyzed for the different rates. Values of E_a were determined by an irreversible three-state model (Eq. 4.9) which is based on an unfolding model according to Eq. 4c. However, as discussed above the irreversible reactions are only one part of the proposed unfolding model according to Eq. 4a and a preequilibrium exists [29]. Therefore, the determination of E_a is influenced by the preequilibrium and values of E_a can be heating rate dependent as well as it has been observed for enthalpy values, DSC, and fluorescence thermograms before [29, 81]. Comparing the different outcomes for the determined correlations between $E_a(\text{CH}_2)$ and thermal stability dependent on slow and fast heating rates, stronger correlations can be determined for 1 K·min⁻¹ compared to 18 K·min⁻¹ and 30 K·min⁻¹. The stronger correlation for $E_a(\text{CH}_2)$ determined from IF profiles at 1 K·min⁻¹ with thermal stability could also be explained by the reversible preequilibrium influencing the unfolding reaction. As Eq. 4a illustrates, the irreversible reaction occurs from the reversible preequilibrium. A certain time is needed to reach this preequilibrium and a faster heating rate can influence the folded/unfolded equilibrium, which again has an influence on the irreversible reaction. In this case, the mAbs are supposed to not fully reach this preequilibrium at heating rates of 18 K·min⁻¹ and 30 K·min⁻¹ and therefore show more similar IF unfolding profiles among each other compared to those profiles recorded at 1 K·min⁻¹ (compare Fig. 4.8). It seems that a heating rate of 1 K·min⁻¹ expresses the unfolding reaction better than 18 K·min⁻¹ and 30 K·min⁻¹ and therefore shows a stronger correlation with thermal stability.

Limitations

The correlation analyses between the predictive parameters and thermal stability follow an overall trend. Indeed, this does not mean that every mAb can be discriminated, especially if the thermal stability is similar. The spreading of the data

around the linear fit underlines this claim. From all of the predictive parameters investigated, the parameter $E_a(\text{CH}_2)$ is identified as the most appropriate for the prediction of the thermal stability of mAbs. Furthermore, this chapter indicates that the link of thermal stability describing the monomer loss is connected to the prediction of aggregation as degradation mechanism rather than fragmentation. No correlation between thermal stability and increase in fragment content is observed for any of the mAbs analyzed. This could be explained by the finding that nonnative aggregation stems from agglomeration of unfolded protein patches [6], which is described by the temperature dependent IF unfolding profiles. In contrast, fragmentation is a process triggered by various chemical reactions [10, 11, 82] instead of the temperature dependent unfolding behavior determined by the assessed IF measurements.

4.6 Conclusion

In this chapter, activation energies of various mAb formulations were determined from IF unfolding thermograms recorded by the NES and were compared to van't Hoff enthalpies and melting temperatures. The mAbs show differences in their thermodynamic and kinetic properties dependent on the analyzed mAb domains and formulations. The predictive parameters were tested to correlate with thermal stability at 25 °C and 40 °C derived from SEC analyses. It is found that $E_a(\text{CH}_2)$ shows the strongest correlation with thermal stability. Furthermore, a slow heating rate of 1 K·min⁻¹ is recommended for the determination of E_a to predict thermal stability instead of using a fast heating rate like 30 K·min⁻¹. However, thermodynamic parameters and melting temperatures also show correlations and should not be neglected while making a prediction of the thermal stability. The predictive parameters can be determined for many different mAbs or different variants of one mAb to select those mAbs showing the most promising parameters. Among these selected mAbs, which show improved thermodynamic and kinetic properties, it is likely that at least one candidate shows superior thermal stability. In summary, this chapter provides and tests supportive tools for a large number of mAbs for prediction of thermal stability of mAbs. The methods and results presented contribute to identify the most appropriate mAb candidate for further target-oriented, time-consuming pharmaceutical development.

Chapter V – Fab assignment

5.1 Abstract

Purpose: In temperature dependent unfolding experiments of monoclonal antibodies (mAbs) usually more than one unfolding transition can be observed. To assign the unfolding transitions in intrinsic fluorescence (IF) thermograms to a certain domain within the mAb, differential scanning calorimetry (DSC) has to be performed and compared to IF thermograms. This procedure is time consuming due to the low sample throughput of DSC measurements.

Methods: To assign an IF transition to the respective mAb domain, two novel methods were developed based on the first derivative of the IF thermogram recorded with two IF spectrometers (a commercially available one, called “Prometheus” as well as a newly developed experimental device (called: “Novel Experimental Setup” (NES), introduced in Chapter IV)). As a first method, the asymmetry of the unfolding transitions was determined and used to assign the Fab to a certain transition in the IF thermogram. As a second method, heating rate dependent IF unfolding experiments spanning from $1 \text{ K}\cdot\text{min}^{-1}$ up to $30 \text{ K}\cdot\text{min}^{-1}$ were performed and the thermograms were analyzed dependent on their increase in the amplitude of the transition.

Results: Using the first method, the Fab can be assigned to the more asymmetric transition in IF thermograms, while the single CH₂- and CH₃-domain show a more symmetric transition. For the second method, an increasing amplitude for ascending heating rates can be analyzed for the Fab unfolding, while the single domains show a nearly constant amplitude. Both methods show a better hit rate for IF profiles recorded by the NES compared to the Prometheus instrument.

Conclusion: The two novel methods make it possible to assign an IF transition to the Fab unfolding without the need to compare IF thermograms with DSC for this purpose. As pointed out in Chapter III and IV before, a correct assignment of the unfolding transition is a prerequisite to compare and assess predictive parameters of different mAbs.

5.2 Introduction

A suitable characterization of monoclonal antibody (mAb) stability is the determination of thermodynamic and kinetic parameters as described in Chapter III and Chapter IV. For temperature dependent unfolding experiments, a common technique is differential scanning calorimetry (DSC), which characterizes the conformational changes during protein unfolding by detecting the changes in the heat capacity of the protein [13, 29]. A second type of technique can be temperature dependent spectroscopic methods like circular dichroism [83] or fluorescence measurements [16] to characterize the unfolding profile of a certain mAb. However, due to the complexity of the mAb structure usually more than one transition can be observed in the unfolding profile of a mAb in both DSC and spectroscopic thermograms. These different unfolding transitions, resulting from the different domains within the mAb [58], make the interpretation of a mAb unfolding profile more complex than for single domain proteins.

Protein unfolding

Protein unfolding can be triggered by various physical and chemical impacts like pH, chaotropic salts and temperature [62, 67, 84]. During unfolding, the dynamic chemical equilibrium between the folded and unfolded state of the protein shifts to the unfolded state. Dependent on the number of transitions in such unfolding experiments, a two-state [39], three-state [41], or a four-state [85] unfolding model can be applied to display the unfolding trace. However, in contrast to single domain proteins, which often show one transition [56], a mAb due to its complex multi-domain structure often shows more than one transition in the unfolding profile [9]. Although the primary sequence of different IgGs only differ in a few amino acids, the differences in the transitions in the unfolding profile can be substantial. Thus, for comparison of different unfolding profiles, it is necessary to assign the transition to the different domains within a mAb. In DSC experiments, the assignment of the unfolding transitions in thermograms has already been reported [17, 58]. However, the assignment of unfolding transitions in temperature dependent intrinsic fluorescence (IF) spectroscopic thermograms of mAbs is directly not possible so far. In those cases, DSC was used to assign the unfolding transitions in spectroscopic thermograms as reported in Chapter III and Chapter IV.

This chapter now introduces two novel methods for the direct identification of the transitions in mAb IF thermograms.

5.3 Material and methods

Antibody formulations

The mAbs used in this chapter are introduced in Chapter III (mAb1 to mAb1e in 25 mM sodium citrate, 125 mM sodium chloride, pH 6.0 buffer (named citrate buffer) and mAb2 and mAb3 in 10 mM sodium phosphate, 10 mM sodium chloride, pH 6.5 buffer (named as phosphate buffer)) and in Chapter IV. From Chapter IV, the 24 mAbs (mAb1 to mAb1e, mAb2 to mAb8, mAb9 to mAb9b, and mAba to mAbh) solved in 10 mM histidine, pH 6.0 formulation (named as F1) were analyzed in this chapter.

Sample preparation

The mAb solutions were prepared as described in Chapter III and Chapter IV. Samples were analyzed at a mAb concentration of $1 \text{ mg}\cdot\text{ml}^{-1}$ in the respective buffer.

Intrinsic fluorescence (IF) spectroscopic measurements

Temperature dependent unfolding experiments were conducted using the commercially available IF spectrometer Prometheus NT.48 and a newly developed experimental device, named as “Novel Experimental Setup” (NES) (both from NanoTemper Technologies GmbH, Munich, Germany) according to the methods described in Chapter III and Chapter IV. Briefly, IF unfolding thermograms were recorded from 20 °C or 35 °C to 95 °C using different heating rates spanning from $1 \text{ K}\cdot\text{min}^{-1}$ up to $30 \text{ K}\cdot\text{min}^{-1}$. For analysis, the first derivative of the FE_{350} / FE_{330} -ratio is plotted against the temperature to assign the unfolding transitions to the different domains within the mAb.

Differential scanning calorimetry (DSC)

DSC measurements of the mAb1 variants (mAb1 to mAb1e) formulated in citrate buffer and mAb2 and mAb3 in phosphate buffer were performed according to Chapter III. For the 24 mAbs in F1 (mAb1 to mAb1e, mAb2 to mAb8, mAb9 to mAb9b, and mAbA to mAbh) the DSC procedures are described in Chapter IV. All DSC measurements were performed at a heating rate of 1 K·min⁻¹.

5.4 Results

In Chapter III and IV, the IF unfolding transitions are assigned by comparing the apparent transitions with DSC thermograms. However, two novel methods based on the first derivative of IF thermograms were developed to assign the Fab transition to a certain IF unfolding transition.

Peak asymmetries (first method)

For the first method, the asymmetry of the transitions of the first derivative IF thermogram was analyzed. For the eight analyzed mAbs in Chapter III, the evaluated thermograms recorded by the Prometheus instrument of mAb1 and mAb1b in citrate buffer and mAb2 and mAb3 in phosphate buffer are illustrated as examples. The first derivative of the IF and DSC unfolding thermograms of mAb1 and mAb1b in citrate buffer are shown in Fig. 5.1.

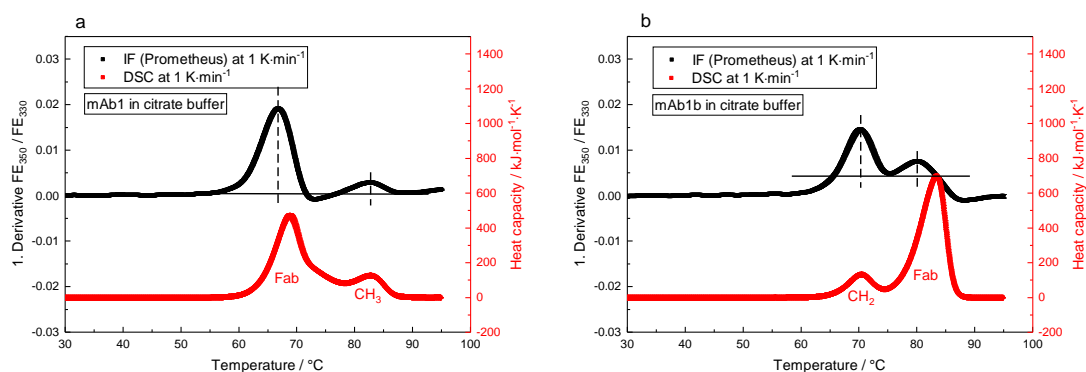


Fig. 5.1: First derivative IF unfolding profile and DSC thermogram of mAb1 and mAb1b. The mean and standard deviation of the first derivative of the fluorescence ratio (FE_{350}/FE_{330}) as a triplicate are plotted against the temperature for mAb1 (a) and mAb1b (b) both solved in citrate buffer. The respective DSC thermogram as a duplicate is depicted as control. IF (Prometheus) and DSC thermograms are shown as an envelope-curve including the standard deviations. A base line (black solid line) was set to separate the two transitions and the symmetry was determined from the transition maximum (black dotted line) to the point, where the unfolding trace touches the baseline. An “Asymmetry Factor” (ASF), as ratio between the two distances from the black dotted line to the signal boundary, was defined to characterize the symmetry of the transition signal in a consistent approach.

In Fig. 5.1a, the first derivative of the IF unfolding profile of mAb1 is shown. Two apparent transitions can be observed as positive signals in the IF thermogram. By analyzing the symmetries of the two signals, it is possible to assign the transition of the Fab in the IF thermogram. Therefore, a baseline (black solid line) was set to separate both transitions so that the unfolding profile contacts the baseline at the beginning and at the end of the signal. To determine the symmetry of the signals, the distance from the transition maximum (black dotted line) to the points, where the unfolding profile touches the baseline at the beginning and the end was measured. The ratio of the distances gives a value, which was defined as “Asymmetry Factor” (ASF). It is practicable to divide the larger distance by the smaller distance. In this case, the ASF is always larger or similar to one. The error of the ASF was determined by considering the uncertainties of the distances. For the distances, an uncertainty of ± 0.5 mm was defined and the error of the ASF was calculated according to the Gauß propagation of uncertainty. By evaluating the first derivative of an IF unfolding profile in the described way, the Fab transition can be assigned to the signal with the largest ASF. For mAb1, the first transition shows the larger ASF (2.2 ± 0.24) compared to the second transition ($ASF = 1.1 \pm 0.15$), so that the Fab unfolding can be assigned to the first transition. Comparing this result with the DSC thermogram, it becomes clear that the first

unfolding transition of mAb1 refers to the Fab. Most properly, the second transition can be assigned to the CH₃-domain, while the CH₂-domain unfolds within the Fab transition, which can be concluded from the temperature area where these domains unfold [17, 58]. For a second example, the first derivative IF thermogram and the DSC thermogram of mAb1b is illustrated in Fig. 5.1b. The larger ASF was determined to the second signal (1.7 ± 0.32) so that the Fab unfolding refers to the second unfolding transition in the IF thermogram. This finding can be confirmed by DSC, which shows that the Fab unfolds during the second transition of mAb1b. The first transition shows most properly the CH₂-domain unfolding with a determined ASF of 1.0 ± 0.14 , while the CH₃-domain unfolds during the Fab unfolding in the second transition.

For the remaining four mAb1 variants formulated in citrate buffer, the Fab transition can correctly be assigned as the first unfolding transition, with an ASF of 2.3 ± 0.1 for mAb1a, 2.3 ± 0.2 for mAb1c, 2.0 ± 0.1 for mAb1d, and 1.7 ± 0.1 for mAb1e. The ASF of the respective second transition of all four mAbs is around 1.1 ± 0.1 and therefore smaller than for the first transition. The respective plots can be found in the Appendix (Fig. A.5.1).

Other examples, which show the first derivative of the unfolding profile of mAb2 and mAb3 in phosphate buffer and the respective DSC thermograms, are shown in Fig. 5.2.

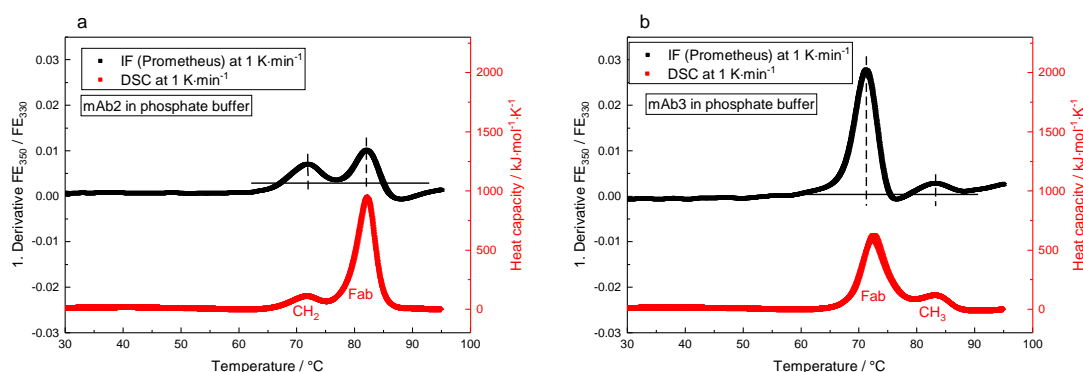


Fig. 5.2: First derivative IF unfolding profile and DSC thermogram of mAb2 and mAb3. The mean and standard deviation of the first derivative of the fluorescence ratio (FE_{350} / FE_{330}) as a triplicate are plotted against the temperature for mAb2 (a) and mAb3 (b) both solved in phosphate buffer. The respective DSC thermogram as a duplicate is depicted as control. IF (Prometheus) and DSC thermograms are shown as an envelope-curve including the standard deviations. Transition signal asymmetries were determined according to the caption of Fig. 5.1.

The more asymmetric signal is determined as the second transition ($ASF = 1.8 \pm 0.35$) in the IF unfolding profile of mAb2 (Fig. 5.2a). Therefore, mAb2 shows the Fab unfolding during the second transition, which can be confirmed by DSC. The first transition shows most properly the CH₂-domain of mAb2 ($ASF = 1.1 \pm 0.17$), while the CH₃-domain unfolding is overlapped from the Fab unfolding during the second transition. In Fig. 5.2b, mAb3 shows the more asymmetric signal during the first transition of the IF unfolding profile resulting in an ASF of 2.4 ± 0.32 . Therefore, the Fab unfolds within the first transition which is also confirmed by DSC. Most properly the Fab unfolding overlaps the CH₂-domain, while the second transition represents the CH₃-domain unfolding showing an ASF of 1.0 ± 0.18 .

The determination of the ASF was also tested for the examples representing the four IF profile categories in Chapter IV. The first derivative of the IF thermograms of mAb_a, mAb_b, mAb_c, and mAb₆ formulated in F1 for the four IF profile categories introduced in Chapter IV are illustrated in Fig. 5.3.

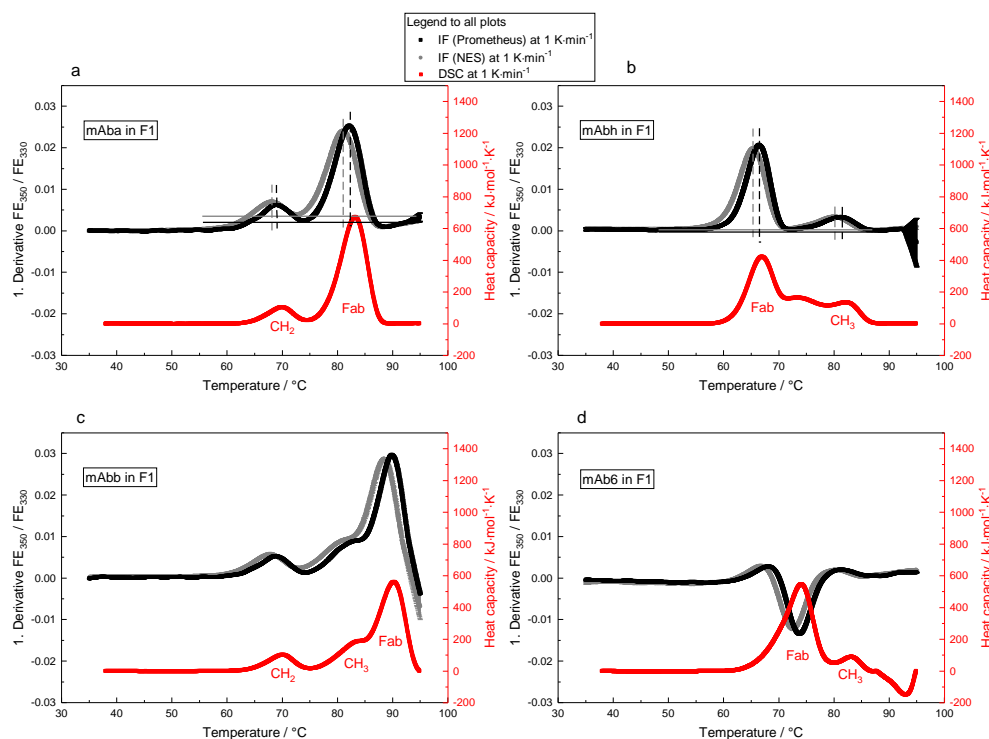


Fig. 5.3: First derivative IF unfolding profile and DSC thermogram of the mAb profile clusters. The mean and standard deviation of the first derivative of the fluorescence ratio (FE_{350}/FE_{330}) as a duplicate are plotted against the temperature for the Prometheus instrument and the NES, shown as an envelope-curve. mAb_a (a) is depicted exemplarily for an IF profile of category 1 (compare Chapter IV), mAb_b (b) as an example for category 2, mAb_c (c) for category 3, and mAb₆ (d) as an example for category 4. The respective DSC thermograms as single determination are depicted as control. For mAb_a and mAb_b, transition signal asymmetries were determined as described for Fig. 5.1. For mAb_c and mAb₆, the asymmetries cannot be determined in the consistent approach as described before.

For the mAbs showing a three-state unfolding behavior with two apparent positive transition signals in their first derivative IF unfolding profile according to category 1 (Fig. 5.3a) and category 2 (Fig. 5.3b), the asymmetries of the signals can be determined as described above. The first transition of mAba has an ASF of 1.2 ± 0.1 and the second transition 1.5 ± 0.1 for both the Prometheus and the NES. Therefore, mAba should show the Fab unfolding within the second transition, which can be confirmed by DSC. For mAbh, the ASF of the first transition is 1.6 ± 0.1 determined by the Prometheus instrument and 2.1 ± 0.1 for the NES. The ASF of the second transition of mAbh can be analyzed to 1.4 ± 0.1 using the Prometheus and to 1.8 ± 0.1 by using the NES. Therefore, the Fab can be assigned to the first transition. For mAbb (category 3) and mAb6 (category 4), the described method determining the asymmetry cannot be applied to those IF profiles. This is caused by the fact that one consistent baseline for all three transitions cannot be set for mAbb. For mAb6, the negative signal overlaps the first and third transition on half so that a reliable symmetry determination is not possible. However, to assign the IF profiles of category 3 and 4, the second method performing different heating rates can be applied (introduced later).

To validate the newly developed first method to assign IF transitions to the Fab unfolding, a broader test set of 24 mAbs formulated in F1 (Chapter IV) was analyzed regarding their signal asymmetries. The results analyzed for IF thermograms recorded by the Prometheus instrument and the NES are summarized in Fig. 5.4, while the respective analyzed IF thermograms together with DSC for control can be found in the Appendix (Fig. A.5.3 to Fig. A.5.6).

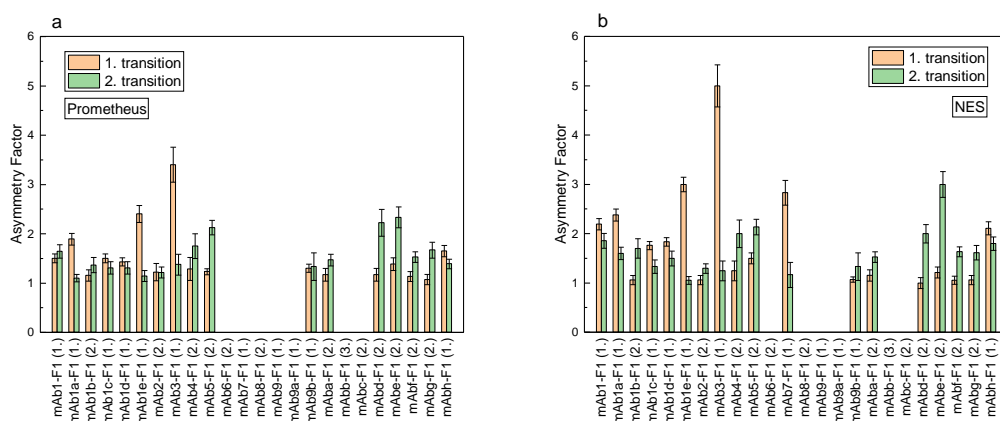


Fig. 5.4: Summarized Asymmetry Factors for the mAbs in F1. For the analyzable first derivative IF unfolding profile according to category 1 and 2 and with transitions showing a sufficient separation, the ASFs are depicted. Errors were calculated using the Gauß propagation of uncertainty as described before. IF profiles were recorded at $1 \text{ K} \cdot \text{min}^{-1}$ using the Prometheus instrument (a) and the NES (b). The number in brackets behind the sample name gives the information, which IF transition can be assigned to the Fab according to DSC.

In Fig. 5.4a, the determined ASFs recorded by the Prometheus instrument are illustrated for the respective mAbs. mAbs with missing values show IF profiles according to category 3 (mAbb) or to category 4 (mAb6, mAb8, mAb9, and mAb9a), where the method cannot be applied. mAbc (for both devices) and mAb7 (analyzed with the Prometheus instrument) do not show a high separation between the transitions and the determination would not give a reliable result. For the remaining mAbs, the transition asymmetries of 10 out of the 17 analyzable mAb IF thermograms recorded by the Prometheus instrument can be discriminated and correctly assigned within the margin of errors (Fig. 5.4a). In contrast, the determination of the ASFs analyzed from IF thermograms recorded by the NES 17 out of 18 samples can be discriminated and correctly assigned to the Fab transition (Fig. 5.4b) giving a hit rate of 94 % compared to 59 % for the Prometheus instrument.

Differences in the signal amplitude (second method)

The second method is illustrated for mAb1 and mAb1b in citrate buffer and mAb2 and mAb3 in phosphate buffer, respectively. The heating rate dependent first derivative IF thermograms recorded by the NES are illustrated in Fig. 5.5.

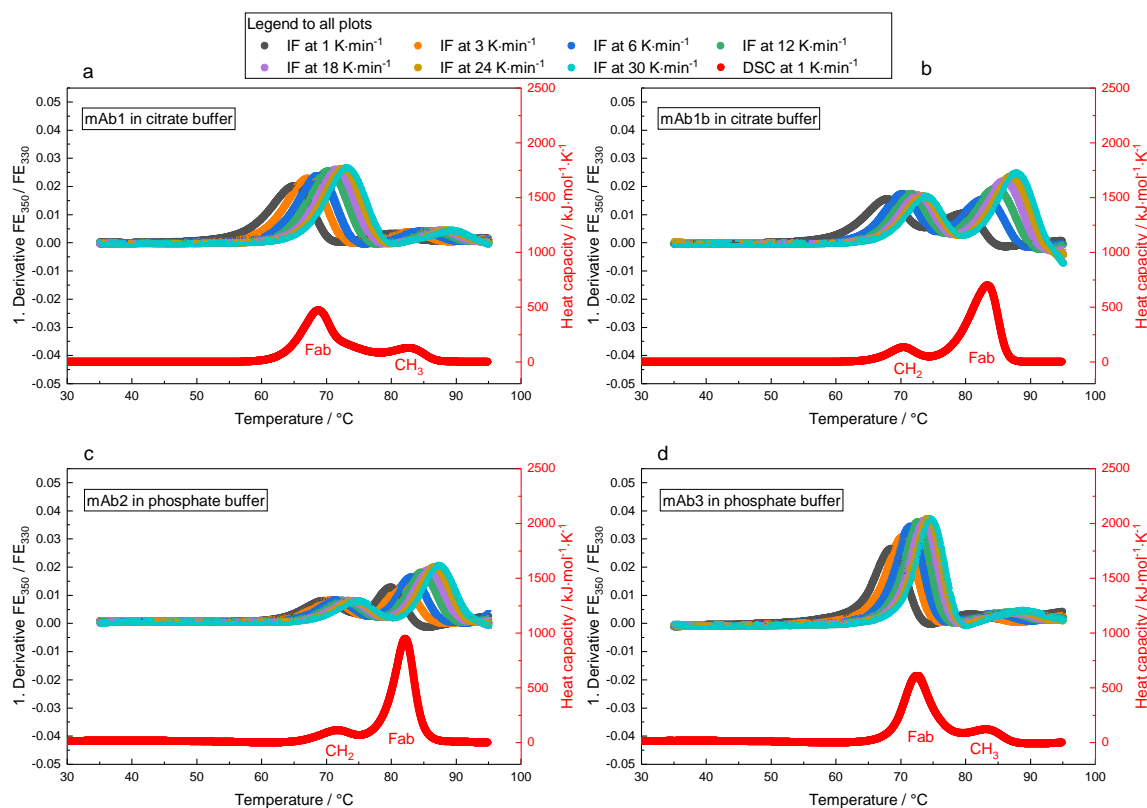


Fig. 5.5: Heating rate dependent changes in the IF unfolding profiles and DSC of mAb1 (a), mAb1b (b), mAb2 (c), and mAb3 (d). The mean and the standard deviation of the first derivative of the FE₃₅₀/FE₃₃₀-ratio as duplicate are plotted against the temperature. Different heating rates were performed spanning from 1 K·min⁻¹ up to 30 K·min⁻¹ using the NES. The respective DSC thermogram as a duplicate is depicted as control. IF (Prometheus) and DSC thermograms are shown as an envelope-curve including the standard deviations.

In general, all transitions shift to increased temperatures by ascending heating rates (Fig. 5.5). However, to assign the Fab to a certain transition, the difference in the signal amplitude has to be evaluated. The transition representing the Fab unfolding shows a transition with an increasing amplitude between a slower and a faster heating rate, which can be deduced from the largest signal in DSC. For mAb1b and mAb2 (Fig. 5.5b and c), this can be observed for the second transition, while for mAb1 and mAb3 the first transition shows the largest increase in the amplitude (Fig. 5.5a and d). This can also be observed for the remaining four mAb1 variants in citrate buffer (mAb1a, mAb1c

to mAb1e), where the respective IF thermograms are depicted in Fig. A.5.2 (Appendix). Therefore, the Fab of all mAb profiles introduced in Chapter III can correctly be assigned using the second method.

The second method was also tested for the mAbs representing the four IF profile categories in Chapter IV: category 1 (mAba), category 2 (mAbh), category 3 (mAbb), and category 4 (mAb6). The IF profiles, recorded by the NES spanning from 1 K·min⁻¹ up to 30 K·min⁻¹, are illustrated in Fig. 5.6.

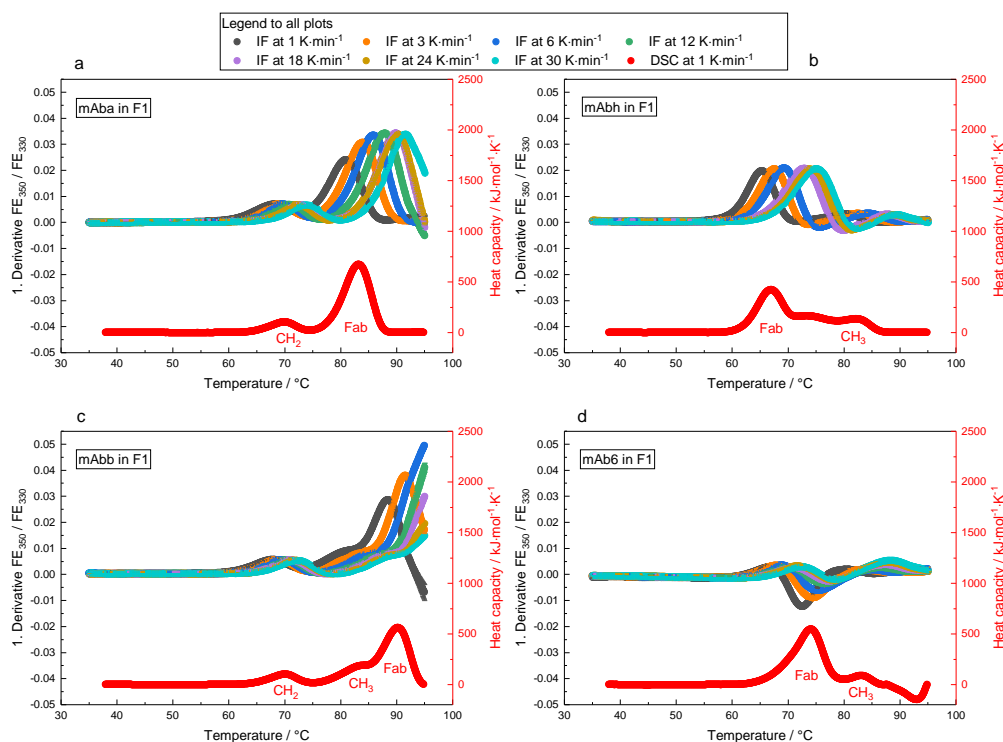


Fig. 5.6: Heating rate dependent changes in the IF profiles and DSC for the cluster profiles. For mAba (a), mAbh (b), mAbb (c), and mAb6 (d) exemplarily shown for the four IF profile categories (compare Chapter IV), the mean and the standard deviation of the first derivative of the FE₃₅₀/FE₃₃₀-ratio as duplicate are plotted against the temperature, shown as an envelope-curve. Heating rates spanning from 1 K·min⁻¹ up to 30 K·min⁻¹ were performed using the NES. The respective DSC thermograms as single determination are depicted as control.

As Fig. 5.6 illustrates, the Fab unfolding shows a transition with a larger increase in the amplitude between a slower and a faster heating rate compared to other transitions in the profile. This conclusion can be made from the largest DSC signal. The largest increase in the amplitude can be analyzed for the second transition of mAba, the third transition of mAbb, and the second transition (negative signal) for mAb6. For mAbh, the first transition (Fab) indeed only shows a slightly larger amplitude increase for

ascending heating rates, but the changes between the first and second transition can just be discriminated within the margin of errors.

Applying the second methods to IF thermograms recorded with the Prometheus instrument of mAba, mAbb, mAbh, and mAb6 at a slower heating rate ($1 \text{ K}\cdot\text{min}^{-1}$) and a faster heating rate ($6 \text{ K}\cdot\text{min}^{-1}$, exception mAbb at $3 \text{ K}\cdot\text{min}^{-1}$), the following results can be observed (Fig. 5.7).

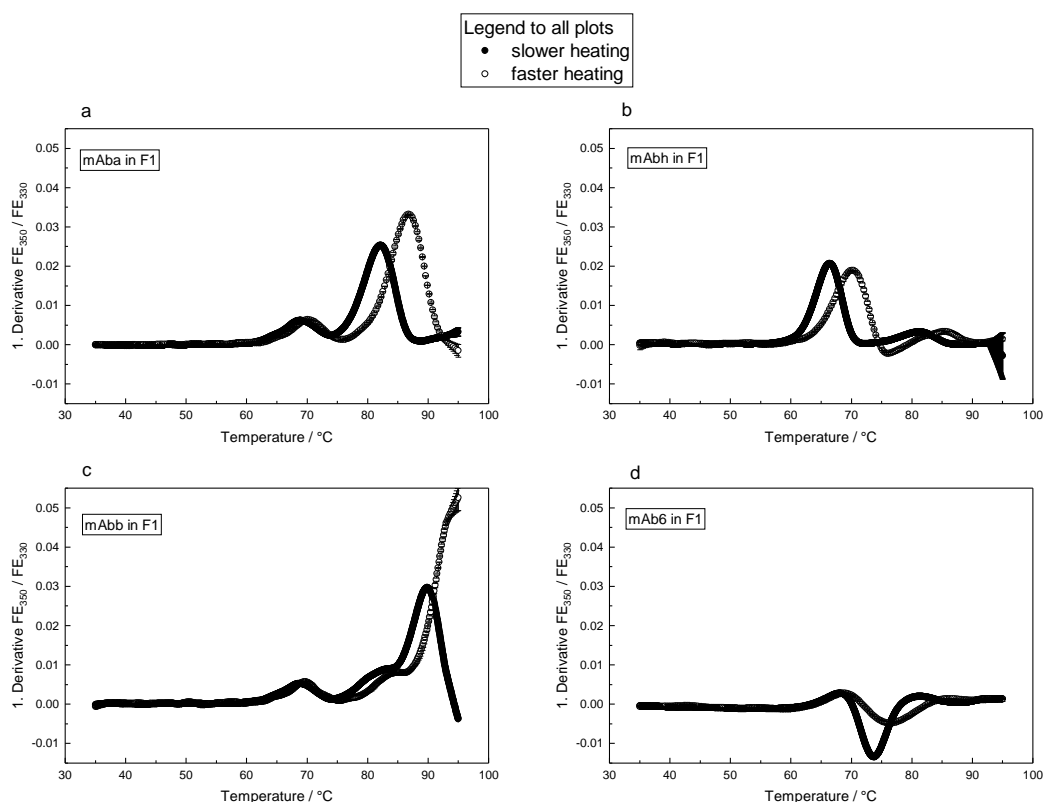


Fig. 5.7: Heating rate dependent IF profiles using the Prometheus instrument. For mAba (a), mAbh (b), mAbb (c), and mAb6 (d) exemplarily shown for the four IF profile categories (compare Chapter IV), the mean and the standard deviation of the first derivative of the FE_{350}/FE_{330} -ratio as duplicate are plotted against the temperature, depicted as an envelope-curve. Heating rates spanning from $1 \text{ K}\cdot\text{min}^{-1}$ to $6 \text{ K}\cdot\text{min}^{-1}$ (exception mAbb at $3 \text{ K}\cdot\text{min}^{-1}$, due to the high T_m for the third transition) were performed using the Prometheus instrument.

In Fig. 5.7, similar results can be observed as compared to Fig. 5.6, with exception that the first transition of mAbh shows a slightly decreasing amplitude with an increasing heating rate. Using the Prometheus, the F_{ab} can be assigned to the transition showing the largest increase in the amplitude, which can be observed for mAba, mAbb, and mAb6.

To validate the second method, the changes in the amplitude (increase or decrease) between slower ($1 \text{ K}\cdot\text{min}^{-1}$) and faster heating rates ($30 \text{ K}\cdot\text{min}^{-1}$, exception mAbb at $3 \text{ K}\cdot\text{min}^{-1}$) of the 24 mAbs in F1 were determined using the NES (IF thermograms are depicted in Fig. A.5.3 to Fig. A.5.6, Appendix). As comparison, the second method was also performed using the Prometheus instrument between $1 \text{ K}\cdot\text{min}^{-1}$ and $6 \text{ K}\cdot\text{min}^{-1}$ (exception mAbb at $3 \text{ K}\cdot\text{min}^{-1}$). The results are summarized in Fig. 5.8.

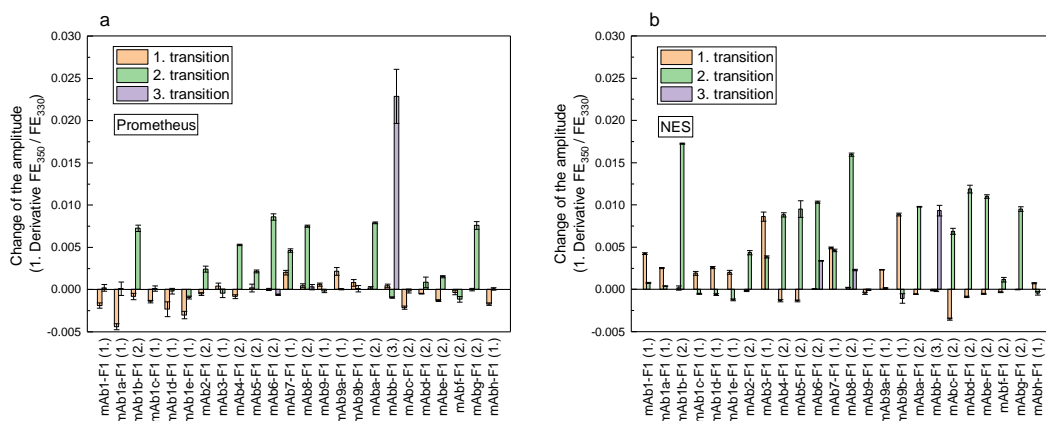


Fig. 5.8: Summarized changes of the amplitudes for different mAb IF thermograms. For 24 mAbs formulated in F1 using the Prometheus instrument (a), the changes of the amplitude from a duplicate measurement between a slow heating rate ($1 \text{ K}\cdot\text{min}^{-1}$) and a fast heating rate ($6 \text{ K}\cdot\text{min}^{-1}$, exception $3 \text{ K}\cdot\text{min}^{-1}$ for mAbb) are depicted. Errors were calculated from the standard deviations of the amplitudes using the Gauß propagation of uncertainty. Positive changes are connected to an amplitude increase from a slower to a faster heating rate, while negative values show a decrease of the amplitude. The results for the NES are shown in (b) between $1 \text{ K}\cdot\text{min}^{-1}$ and $30 \text{ K}\cdot\text{min}^{-1}$ (exception mAbb at $3 \text{ K}\cdot\text{min}^{-1}$). The transition showing the largest increase in the amplitude can be assigned to the Fab unfolding. The number in brackets behind the sample name gives the information, which IF transition can be assigned to the Fab according to DSC.

According to the second method, the Fab is assigned to the transition showing the largest increase in the amplitude (largest positive bars in Fig. 5.8). By doing so, the Prometheus instrument (Fig. 5.8a) only shows 14 out of 24 mAbs that can be discriminated and correctly be assigned to the Fab, showing a significantly increase in the amplitude between a slow and a fast heating rate. Using the NES, 23 out of 24 mAbs can be discriminated and correctly assigned to the Fab, showing a hit rate of 96 % compared to a hit rate of only 58 % using the Prometheus instrument.

In summary, it can be concluded that the Fab of all mAbs (with exception of mAb9) can be assigned to a certain unfolding transition in IF thermograms using the two newly

introduced methods. The correct assignment was verified by DSC. The results show that IF profiles recorded by the NES should be used instead of the Prometheus instrument to assign a certain transition to the Fab unfolding.

5.5 Discussion

Explanations for the observed properties

This chapter introduces two novel methods to identify the Fab unfolding in temperature dependent IF unfolding profiles of mAbs. The first introduced method determining the asymmetry of the transitions was tested for several IgG1 mAbs. For mAbs showing an apparent three-state unfolding behavior, the transitions result from the Fab, the CH₂-, and the CH₃-domain, at which either the CH₂- or the CH₃-domain is overlaid by the Fab fragment (category 1 and 2) [17, 58]. The mAbs, following a three-state unfolding model, show an unfolding profile in the first derivative IF thermogram that the asymmetry of the Fab transition is larger than the asymmetry of the single CH₂- and CH₃-domain transition. To have a consistent method determining the most asymmetric signal, an Asymmetry Factor was established. The characteristic of the Fab transition asymmetry in the first derivative of IF thermograms could stem from the amount of four different domains within the Fab. A hint that the amount of different domains could influence the shape of the transition signals in IF thermograms can be the findings of Shimba et al. [59]. They determined DSC thermograms of three different isolated Fab variants of an IgG, where the Fab variants are composed of different amounts of domains. In their DSC thermograms, it can be observed that the Fab composed of four different domains has a more asymmetric signal than the Fab, which is composed of two different domains. As shown in Chapter III, the cooperativity unit of the Fab is higher than of the single CH₂- or CH₃-domain. A cooperativity closer to one results in a more sigmoidal character of the single domain transition compared to the Fab transition. A sigmoidal transition can be interpreted that the transition is cooperative between two states [86]. This higher cooperativity results in a more symmetric transition in the first derivative for the single domains and therefore in an ASF close to one.

The second method determining the heating rate dependent changes in the amplitude of the first derivative IF profiles can also be used to identify the Fab unfolding transition.

In this case, the Fab transition shows a larger increase in the amplitude from a slow to a fast heating rate compared to the single CH₂- and CH₃-domain transitions. The heating rate dependent changes in the IF unfolding profiles could also be explained with the differences in the cooperativity of the Fab compared to the single domains. By performing temperature dependent unfolding experiments using the NES, the signal amplitude of the Fab transition increases with increasing heating rates. A decreasing amplitude for the Fab observed for IF profiles recorded by the Prometheus instrument is supposed to be attributed to a lack of resolution detecting the fluorescence signals at faster heating rates (see below for a device comparison). Parallel to the amplitude increase, the transitions shift to higher temperatures for faster heating rates, which is not only the case for the Fab, but also for the CH₂- and CH₃-domain. The transition shift towards higher temperatures for faster heating has also been observed for fluorescence and DSC thermograms before [81]. The transition shift for the Fab and the single domain transitions could be explained that the mAb is exposed for a shorter time at each temperature for faster heating rates. In contrast to this heating rate dependent characteristic, the amplitude of the first derivative in IF thermograms represents the changes in the fluorescence ratio dependent on the temperature and the characteristics are different for the Fab and the single domain transitions. Within the Fab transition, at least four different domains from the Fab unfold within the transition, whereas the different domains could influence each other in their unfolding behavior due to their interactions among them. The influences of different domains within the Fab and their interactions have been reported before [87, 88]. Due to the fact that the Fab transition shifts to higher temperatures for ascending heating rates, the increased temperature could break those domain interactions within the Fab. This could lead to higher cooperativity and a more simultaneously unfolding of the different domains within the Fab. This becomes noticeable in an increased unfolding change and therefore a signal showing a larger amplitude in the first derivative for the Fab compared to the single domains. The heating rate dependent change in the signal amplitude is differently pronounced, which could be explained by different domain-domain interactions within the Fab. Little changes in the amplitude could therefore be associate with less stronger interactions between the domains. However, this has to be investigated in further studies. For the CH₂- and CH₃-domain transition, only one domain unfolds within the transition and thus, there can be no changes in the interactions between different domains within a single domain transition. Therefore,

the signal amplitude remains nearly constant in most cases, while the transition shifts to higher temperatures for faster heating rates. Larger changes in the amplitude of the single domain transition could most properly explained by a high overlap of the Fab transition.

Differences between the IF spectrometers (Prometheus vs. NES)

The observed properties in the first derivative IF thermogram, which were used to assign a certain transition to the Fab unfolding, are more pronounced for profiles recorded by the NES compared to the Prometheus instrument. In general, it is expected that both devices should show similar results and that the observed properties are not device dependent. For the determination of the transition asymmetry (first method), several mAbs cannot be assigned within error bars using the Prometheus instrument. Nevertheless, in most cases the Fab shows the more asymmetric signal for these mAbs. Possibly, the resolution detecting unfolding for the Prometheus is not as good as it can be observed for the NES. This hypothesis can be substantiated by the fact that the onset temperature at which the mAbs start to unfold, is slightly lower for the NES than for the Prometheus indicating a more sensitive detection for the unfolding begin. The improved detection optic for the NES is also obvious by recording IF thermograms at faster heating rates. In this case, the fluorescence signal is more stable and therefore allows the assignment of the Fab according to the second method. This becomes obvious in the smaller standard deviations at faster heating rates recorded by the NES compared to the Prometheus instrument. Therefore, the NES is recommended for the two newly developed approaches using IF thermograms to assign a certain transition to the Fab unfolding.

5.6 Conclusion

In this chapter, two novel methods were developed to assign an IF transition to the Fab unfolding. For this purpose, either the transition signal asymmetry of the first derivative IF thermogram or the heating rate dependent changes of the amplitude have to be analyzed. While the first method determining the signal asymmetry can be applied for one IF thermogram at $1 \text{ K} \cdot \text{min}^{-1}$, the second method performing different heating rates needs the record of at least two experiments. However, the second method can be

applied to a broader range of IF thermograms. Therefore, it is recommended to first perform an IF thermogram at $1 \text{ K}\cdot\text{min}^{-1}$. If a three-state unfolding IF profile with two separated transitions is recorded, the transition signal asymmetry can be analyzed. In a case, where the IF transition asymmetry cannot be analyzed in the described manner, at least one additional measurement at a faster heating rate has to be performed. The transition signal showing the largest increase in the amplitude from a slow to a fast heating rate can then be assigned to the Fab transition. The two newly introduced methods are recommended for IF thermograms recorded by the NES due to the higher hit rate compared to the Prometheus instrument. The correct assignment of IF unfolding transitions to a certain mAb domain is important to compare different IF profiles and their predictive parameters as illustrated in Chapter III and IV. This is now possible for IF temperature dependent experiments without the comparison to DSC thermograms. This is an essential improvement of fluorescence unfolding experiments, because IF experiments have an easier sample handling and a higher throughput than DSC experiments.

Chapter VI – Concluding remarks

6.1 Conclusion

The present study introduces different thermodynamic and kinetic parameters derived from temperature dependent unfolding experiments and evaluates their predictive character regarding mAb thermal stability. In conclusion, this study can give a guideline of how an assessment of thermal mAb stability could look like (illustrated in Fig 6.1).

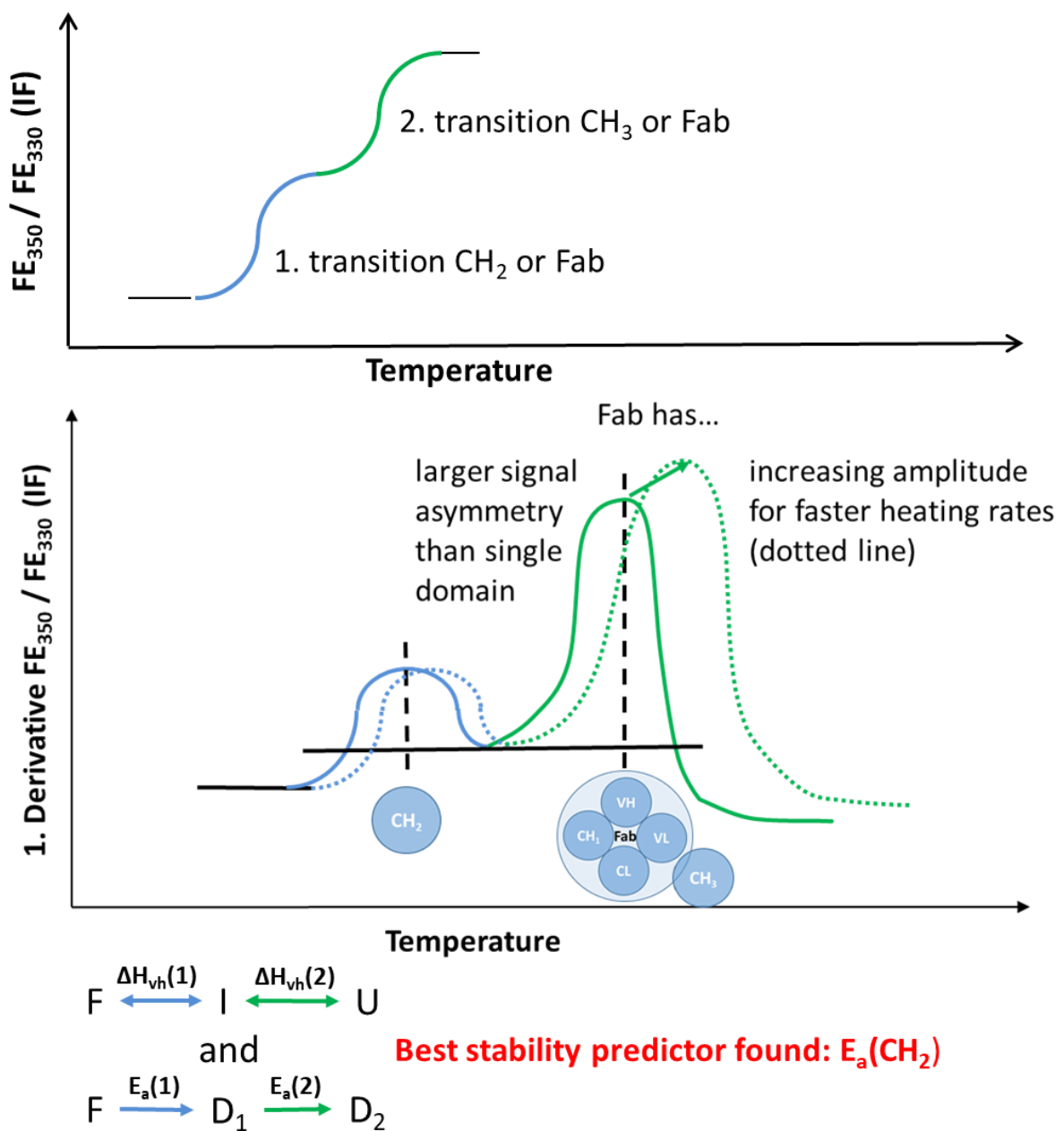


Fig. 6.1: Graphical summary of a thermal stability assessment of mAbs.

The routine can start with first and rapid IF unfolding screening of various mAb variants in different formulations. Dependent on the first derivative IF unfolding profile, the asymmetry of the transition signal gives advice, which transition refers to the Fab unfolding. With this information, the remaining CH₂- and CH₃-domain of an IgG1 molecule can be assigned. In those cases, where the asymmetry cannot be discriminated or the IF profile does not match a three-state model, an additional measurement with a faster heating rate can be performed. Dependent on the amplitude change of the first derivative IF profile, the Fab can be assigned. Once the IF transitions are assigned to a certain mAb region, the IF thermograms can be analyzed regarding their thermodynamic and kinetic parameters. For those mAbs, for that a CH₂-domain transition can be detected, it is recommended to first rank the expected thermal stability of different mAbs according to largest $E_a(\text{CH}_2)$ values. In a second step, ΔH_{vh} and T_m values of the CH₂-domain should be considered for stability ranking. For mAb profiles, for which the CH₂-domain transition is overlaid by the Fab transition and a comparison of the predictive parameters from the CH₂-domain transition is not possible, predictive parameters derived from the Fab transition should be considered for prediction of thermal stability. For these mAbs, $\Delta H_{vh}(\text{Fab})$ was identified as the most appropriate parameter. In summary, the present study delivers an assessment of different predictive parameters for thermal stability of various mAbs, mAb variants, and formulations and provides tools for interpreting IF profiles more precisely regarding the mAb region involved in unfolding transition. The findings and procedures of this study make it possible to rank different mAbs according to their investigated thermodynamic and kinetic parameters.

6.2 Outlook

The present study provides an assessment of different parameters for the use of predicting thermal stability of mAbs. However, some questions regarding the topic of stability predictions are still open. One aspect that was also mentioned and discussed in Chapter IV is the increasing colloidal influences of formulation by increased concentrations of mAb and NaCl. Besides conformational stability mainly described in this study, colloidal stability is another aspect to consider. In the case of colloidal stability, other techniques like dynamic light scattering, self-interaction chromatography, and small angle x-ray scattering provide parameters describing protein-protein

interactions [19, 89, 90]. For further improved stability prediction, a combination of parameters describing conformational and colloidal stability could be promising. For this purpose, conformational and colloidal parameters have to be weighted regarding their expected influence. Dependent on the formulation either the conformational parameter or the colloidal parameter is assessed with a larger impact on thermal stability and a higher or lower impact is referred to the respective conformational and colloidal parameter for stability prediction. One interesting approach has recently been published by Oyama et al. combining the interaction parameter B_{22} with the aggregation temperature (T_{agg}). However, its validity to stability prediction is limited due to a T_{agg} value which is close to the incubation temperature for thermal stability [91]. Another starting point for further possible improvements and accurate description of mAb unfolding can be the development of a mathematical model that describes the proposed unfolding mechanism more exactly than described in this study. In the present case, this means that a mathematical model could be developed for the unfolding reaction presented in Eq. 4a as described in Chapter IV. The challenge might be that for each apparent transition in an IF thermogram the proposed two reactions (reversible and irreversible) have to be described within one transition. This more accurate description could lead to more precise thermodynamic and kinetic parameters and could further improve thermal stability prediction. Another way to improve the applicability of IF fitting to describe thermodynamics and kinetics can be the development of fit function describing special cases of IF profile like the wave-shaped profile introduced in Chapter IV. Regarding the IF analysis, the commercial Prometheus instrument can be improved for detecting IF profiles at faster heating rates more precisely as it can be observed for the NES. For this purpose, the Prometheus instrument could then also be used to assign IF transition to a certain mAb region with a higher accuracy. The main advantage of a newly developed Prometheus instrument over the NES would be a much higher throughput of 48 samples instead of two samples per run.

Chapter VII - Bibliography

7.1 Danksagungen

Für die Anfertigung meiner Doktorarbeit gilt es an dieser Stelle meinen Dank auszusprechen. Zunächst möchte ich mich für die wissenschaftliche Betreuung und die Anstellung als Doktorand in der Naturwissenschaftlichen Fakultät II der Martin-Luther-Universität Halle-Wittenberg bei Herrn Prof. Dr. Dariush Hinderberger bedanken. Vielen Dank, dass Sie trotz der weiten Distanz die wissenschaftliche Betreuung der Doktorarbeit übernommen haben. Weiterhin gibt es Dank zu sagen an Dr. Michaela Blech für die fachliche Betreuung und freundliche Aufnahme in Ihre Laborgruppe vor Ort in Biberach bei Boehringer Ingelheim innerhalb der Abteilung „Pharmaceutical Development Biologicals (PDB), Early Stage 2“. Vielen Dank, dass Sie die Anfertigung dieser Doktorarbeit mit ermöglicht haben. Hier ist vor allem auch die Kooperation mit NanoTemper zu erwähnen, die Sie mit organisiert haben. Bei Prof. Dr. Patrick Garidel möchte ich mich für die wissenschaftliche Betreuung und hilfreichen fachlichen Diskussionen im speziellen zu Themen der Thermodynamik und DSC bedanken. Von Seiten NanoTemper gibt es Dank zu sagen an Dr. David Ng für die Entwicklung des NES und dem dazugehörigen Python Skript mit Fitfunktion zur Bestimmung von Aktivierungsenergien. Des Weiteren danke ich Dr. Nuska Tschammer, Dr. Philipp Baaske und Dr. Anna Schulze von NanoTemper für fachliche Betreuung im Besonderen zu Themen von Fluoreszenz Spektroskopie und Bestimmung von Aktivierungsenergien. Für das Korrekturlesen möchte ich zusätzlich noch Dr. Judith Mittag und Ibrahim Fawaz von Boehringer Ingelheim danken.

Für die Durchführung von DSC Messungen ist vor allem Gabriele Richter und Samuel Hempelt von Boehringer Ingelheim zu danken. Zudem gilt es Dank zu sagen für die Bereitstellung von thermischen Stabilitätsdaten aus verschiedenen Entwicklungsstudien und Arbeiten. Vielen Dank dazu an Oliver Mayer, Samuel Hempelt, Felicitas Wahl, Stefanie Konzelmann und Simone Schaz von Boehringer Ingelheim. Zudem möchte ich mich bei allen Kollegen in der PDB bedanken für die schöne Arbeitsatmosphäre und Unterstützungen bei Fragen und im Speziellen bei meinen Doktorandenkollegen Josef Hartl, Nils Glücklich, Ibrahim Fawaz und Elena Hipper für die schöne Zeit im Büro.

Zuletzt gilt es noch Dank an meine Frau Dr. med. Marie-Christin Melien für ihre berufliche Flexibilität und Bereitschaft zum Wohnortwechsel nach Biberach. Vielen Dank für die moralische Unterstützung und für den „Blick über den Tellerrand hinaus“ was medizinische Fragestellung und Wissen angeht. Meinen Eltern Monika und Eberhard Weber möchte ich auch danken für die Unterstützungen während des Studiums, das Voraussetzung für die Doktorarbeit war.

7.2 References

1. Wang, W., et al., *Antibody structure, instability, and formulation*. J Pharm Sci, 2007. **96**(1): p. 1-26.
2. Frokjaer, S. and D.E. Otzen, *Protein drug stability: a formulation challenge*. Nat Rev Drug Discov, 2005. **4**(4): p. 298-306.
3. Roberts, C.J., T.K. Das, and E. Sahin, *Predicting solution aggregation rates for therapeutic proteins: Approaches and challenges*. International Journal of Pharmaceutics, 2011. **418**(2): p. 318-333.
4. Wang, W., S. Nema, and D. Teagarden, *Protein aggregation--pathways and influencing factors*. Int J Pharm, 2010. **390**(2): p. 89-99.
5. Wang, W., *Instability, stabilization, and formulation of liquid protein pharmaceuticals*. Int J Pharm, 1999. **185**(2): p. 129-88.
6. Roberts, C.J., *Non-native protein aggregation kinetics*. Biotechnology and Bioengineering, 2007. **98**(5): p. 927-938.
7. Amin, S., et al., *Protein aggregation, particle formation, characterization & rheology*. Current Opinion in Colloid and Interface Science, 2014. **19**(5): p. 438-449.
8. Andrews, J.M. and C.J. Roberts, *A Lumry–Eyring Nucleated Polymerization Model of Protein Aggregation Kinetics: 1. Aggregation with Pre-Equilibrated Unfolding*. The Journal of Physical Chemistry B, 2007. **111**(27): p. 7897-7913.
9. Brummitt, R.K., et al., *Nonnative aggregation of an IgG1 antibody in acidic conditions: Part 1. Unfolding, colloidal interactions, and formation of high-molecular-weight aggregates*. Journal of Pharmaceutical Sciences, 2011. **100**(6): p. 2087-2103.
10. Cohen, S.L., C. Price, and J. Vlasak, *β -Elimination and Peptide Bond Hydrolysis: Two Distinct Mechanisms of Human IgG1 Hinge Fragmentation upon Storage*. Journal of the American Chemical Society, 2007. **129**(22): p. 6976-6977.
11. Vlasak, J. and R. Ionescu, *Fragmentation of monoclonal antibodies*. MAbs, 2011. **3**(3): p. 253-63.
12. Shire, S.J., Z. Shahrokh, and J. Liu, *Challenges in the development of high protein concentration formulations*. Journal of Pharmaceutical Sciences, 2004. **93**(6): p. 1390-1402.
13. Bruylants, G., J. Wouters, and C. Michaux, *Differential scanning calorimetry in life science: thermodynamics, stability, molecular recognition and application in drug design*. Current medicinal chemistry, 2005. **12**(17): p. 2011-2020.

14. den Engelsman, J., et al., *Strategies for the Assessment of Protein Aggregates in Pharmaceutical Biotech Product Development*. Pharmaceutical Research, 2011. **28**(4): p. 920-933.
15. Garidel, P., et al., *A rapid, sensitive and economical assessment of monoclonal antibody conformational stability by intrinsic tryptophan fluorescence spectroscopy*. Biotechnology Journal, 2008. **3**(9-10): p. 1201-1211.
16. Garidel, P., A.R. Karow, and M. Blech, *Orthogonal spectroscopic techniques for the early developability assessment of therapeutic protein candidates*. Spectrosc. Eur., 2014. **28**(4): p. 9-13.
17. Lowe, D., et al., *Aggregation, stability, and formulation of human antibody therapeutics*, in *Advances in protein chemistry and structural biology*. 2011, Elsevier. p. 41-61.
18. Gill, P., T.T. Moghadam, and B. Ranjbar, *Differential scanning calorimetry techniques: applications in biology and nanoscience*. J Biomol Tech, 2010. **21**(4): p. 167-93.
19. Blaffert, J., et al., *Spectroscopic methods for assessing the molecular origins of macroscopic solution properties of highly concentrated liquid protein solutions*. Analytical Biochemistry, 2018. **561-562**: p. 70-88.
20. Breitsprecher, D., et al. *Getting the Full Picture: Predicting the Aggregation propensity of mAbs Using Chemical and Thermal Denaturation on a Single, Fully Automated Platform*, Application Note NT-PR-011, . 2016. 7.
21. Eftink, M.R., *The use of fluorescence methods to monitor unfolding transitions in proteins*. Biophysical journal, 1994. **66**(2): p. 482-501.
22. Seeliger, D., et al., *Boosting antibody developability through rational sequence optimization*. MAbs, 2015. **7**(3): p. 505-515.
23. van der Kant, R., et al., *Prediction and Reduction of the Aggregation of Monoclonal Antibodies*. Journal of Molecular Biology, 2017. **429**(8): p. 1244-1261.
24. Bauer, J., et al., *Rational optimization of a monoclonal antibody improves the aggregation propensity and enhances the CMC properties along the entire pharmaceutical process chain*. mAbs, 2020. **12**(1): p. 1787121.
25. Czeslik, C., H. Seemann, and R. Winter, *Basiswissen Physikalische Chemie*. Vol. 4. 2010, Wiesbaden: Vieweg+Teubner.
26. Gey, M.H., *Instrumentelle Analytik und Bioanalytik*. Vol. 3. 2015, Berlin Heidelberg: Springer.
27. Lakowicz, J.R., *Principles of fluorescence spectroscopy*. Vol. 3. 2006: Springer.
28. *Prometheus - The new gold standard for challenging stability characterizations*.
29. Privalov, P.L. and S.A. Potekhin, [2] *Scanning microcalorimetry in studying temperature-induced changes in proteins*. Methods in enzymology, 1986. **131**: p. 4-51.
30. Privalov, P.L., *Stability of proteins small globular proteins*, in *Advances in protein chemistry*. 1979, Elsevier. p. 167-241.
31. Feige, M.J., L.M. Hendershot, and J. Buchner, *How antibodies fold*. Trends in biochemical sciences, 2010. **35**(4): p. 189-198.
32. Keizer, R.J., et al., *Clinical Pharmacokinetics of Therapeutic Monoclonal Antibodies*. Clinical Pharmacokinetics, 2010. **49**(8): p. 493-507.
33. Jefferis, R. and D.S. Kumararatne, *Selective IgG subclass deficiency: Quantification and clinical relevance*. Clinical and Experimental Immunology, 1990. **81**(3): p. 357-367.
34. Jefferis, R., *Antibody therapeutics: Isotype and glycoform selection*. Expert Opinion on Biological Therapy, 2007. **7**(9): p. 1401-1413.

35. Berg, J.M., J.L. Tymoczko, and L. Stryer, *Stryer Biochemie*. Vol. 7. 2013, Berlin Heidelberg: Springer.
36. Melien, R., et al., *Thermodynamic Unfolding and Aggregation Fingerprints of Monoclonal Antibodies Using Thermal Profiling*. *Pharmaceutical Research*, 2020. **37**(4): p. 78.
37. Wang, W., *Protein aggregation and its inhibition in biopharmaceutics*. *Int J Pharm*, 2005. **289**(1-2): p. 1-30.
38. Dill, K.A., *Dominant Forces in Protein Folding*. *Biochemistry*, 1990. **19**(31): p. 7133-7155.
39. Meuzelaar, H., J. Vreede, and S. Woutersen, *Influence of Glu/Arg, Asp/Arg, and Glu/Lys Salt Bridges on α -Helical Stability and Folding Kinetics*. *Biophysical Journal*, 2016. **110**(11): p. 2328-2341.
40. Kubelka, J., et al., *Chemical, physical, and theoretical kinetics of an ultrafast folding protein*. *Proceedings of the National Academy of Sciences*, 2008. **105**(48): p. 18655-18662.
41. Boehm, K., et al., *Thermodynamic Analysis of Denaturant-Induced Unfolding of HodC69S Protein Supports a Three-State Mechanism*. *Biochemistry*, 2008. **47**(27): p. 7116-7126.
42. Davis, C.M. and R.B. Dyer, *The Role of Electrostatic Interactions in Folding of β -Proteins*. *Journal of the American Chemical Society*, 2016. **138**(4): p. 1456-1464.
43. Naganathan, A.N., U. Doshi, and V. Muñoz, *Protein Folding Kinetics: Barrier Effects in Chemical and Thermal Denaturation Experiments*. *Journal of the American Chemical Society*, 2007. **129**(17): p. 5673-5682.
44. Beermann, B., et al., *Stability, Unfolding, and Structural Changes of Cofactor-Free 1H-3-Hydroxy-4-oxoquinoline 2,4-Dioxygenase*. *Biochemistry*, 2007. **46**(14): p. 4241-4249.
45. Zimm, B.H. and J.K. Bragg, *Theory of the phase transition between helix and random coil in polypeptide chains*. *The Journal of Chemical Physics*, 1959. **31**(2): p. 526-535.
46. Seelig, J. and H.-J. Schönfeld, *Thermal protein unfolding by differential scanning calorimetry and circular dichroism spectroscopy two-state model versus sequential unfolding*. *Quarterly reviews of biophysics*, 2016. **49**.
47. Li-Blatter, X. and J. Seelig, *Thermal and Chemical Unfolding of Lysozyme. Multistate Zimm–Bragg Theory Versus Two-State Model*. *The Journal of Physical Chemistry B*, 2019. **123**(48): p. 10181-10191.
48. Garidel, P., et al., *Thermal and Chemical Unfolding of a monoclonal IgG1 antibody: Application of the Multi-State Zimm-Bragg Theory*. *Biophysical Journal*, 2020.
49. Sötl, F., et al. *Analysis of formulation-dependent colloidal and conformational stability of monoclonal antibodies, Application Note NT-PR-005*, . 2015. 7.
50. Bergemann, K., et al., *Production and downstream processing*, in *Handbook of therapeutic antibodies*. 2007. p. 199-237.
51. Serdyuk, I.N., N.R. Zaccai, and J. Zaccai, *Methods in molecular biophysics: structure, dynamics, function*. 2007, Cambridge University Press. p. 194-220.
52. Færgeman, N.J., et al., *Thermodynamics of Ligand Binding to Acyl-Coenzyme A Binding Protein Studied by Titration Calorimetry*. *Biochemistry*, 1996. **35**(45): p. 14118-14126.
53. Gummadi, S.N., *What is the Role of Thermodynamics on Protein Stability*. *Biotechnology and Bioprocess Engineering*, 2003. **8**(9): p. 9-18.

54. Meuzelaar, H., et al., *Solvent-Exposed Salt Bridges Influence the Kinetics of α -Helix Folding and Unfolding*. The Journal of Physical Chemistry Letters, 2014. **5**(5): p. 900-904.
55. Doig, A.J. and M.J.E. Sternberg, *Side-chain conformational entropy in protein folding*. Protein Science, 1995. **4**(11): p. 2247-2251.
56. Makhatadze, G.I. and P.L. Privalov, *Energetics of Protein Structure*, in *Advances in Protein Chemistry*. 1995. p. 307-425.
57. Southall, N.T., K.A. Dill, and A. Haymet, *A view of the hydrophobic effect*. 2002, ACS Publications.
58. Garber, E. and S.J. Demarest, *A broad range of Fab stabilities within a host of therapeutic IgGs*. Biochem Biophys Res Commun, 2007. **355**(3): p. 751-7.
59. Shimba, N., et al., *Comparative thermodynamic analyses of the Fv, Fab* and Fab and Fab fragments of anti-dansyl mouse monoclonal antibody*. FEBS Letters, 1995. **360**(3): p. 247-250.
60. Ionescu, R.M., et al., *Contribution of variable domains to the stability of humanized IgG1 monoclonal antibodies*. Journal of pharmaceutical sciences, 2008. **97**(4): p. 1414-1426.
61. Andersen, C.B., et al., *Aggregation of a multidomain protein : A coagulation mechanism governs aggregation of a model IgG1 antibody under weak thermal stress*. Protein Science, 2010. **19**(2): p. 279.
62. Sahin, E., et al., *Comparative effects of pH and ionic strength on protein-protein interactions, unfolding, and aggregation for IgG1 antibodies*. Journal of Pharmaceutical Sciences, 2010. **99**(12): p. 4830-4848.
63. Wu, H., et al., *Competing aggregation pathways for monoclonal antibodies*. FEBS Letters, 2014. **588**(6): p. 936-941.
64. Brader, M.L., et al., *Examination of thermal unfolding and aggregation profiles of a series of developable therapeutic monoclonal antibodies*. Molecular pharmaceutics, 2015. **12**(4): p. 1005-1017.
65. Lumry, R. and H. Eyring, *Conformation changes of proteins*. The Journal of physical chemistry, 1954. **58**(2): p. 110-120.
66. Singla, A., et al., *Aggregation Kinetics for IgG1-Based Monoclonal Antibody Therapeutics*. The AAPS Journal, 2016. **18**(3): p. 689-702.
67. Seelig, J., *Cooperative protein unfolding. A statistical-mechanical model for the action of denaturants*. Biophysical chemistry, 2018. **233**: p. 19-25.
68. Kesik-Brodacka, M., *Progress in biopharmaceutical development*. Biotechnology and Applied Biochemistry, 2018. **65**(3): p. 306-322.
69. Zbacnik, N.J., C.S. Henry, and M.C. Manning, *A Chemometric Approach Toward Predicting the Relative Aggregation Propensity: A β (1-42)*. Journal of Pharmaceutical Sciences, 2020. **109**(1): p. 624-632.
70. Bedouelle, H., *Principles and equations for measuring and interpreting protein stability: From monomer to tetramer*. Biochimie, 2016. **121**: p. 29-37.
71. Colón, W., et al., *Biological Roles of Protein Kinetic Stability*. Biochemistry, 2017. **56**(47): p. 6179-6186.
72. Finkelstein, A.V., et al., *There and back again: Two views on the protein folding puzzle*. Physics of Life Reviews, 2017. **21**: p. 56-71.
73. Cai, J., et al., *New temperature integral approximation for nonisothermal kinetics*. AIChE Journal, 2006. **52**(4): p. 1554-1557.
74. Cai, J. and R. Liu, *An improved version of Junmeng–Fang–Weiming–Fusheng approximation for the temperature integral*. Journal of Mathematical Chemistry, 2008. **43**(3): p. 1193-1198.

75. Voordouw, G., C. Milo, and R.S. Roche, *Role of bound calcium ions in thermostable, proteolytic enzymes. Separation of intrinsic and calcium ion contributions to the kinetic thermal stability.* Biochemistry, 1976. **15**(17): p. 3716-3724.
76. Fujita, S.C., N. Go, and K. Imahori, *Melting-profile analysis of thermal stability of thermolysin. A formulation of temperature-scanning kinetics.* Biochemistry, 1979. **18**(1): p. 24-28.
77. Kim, N., et al., *Aggregation of anti-streptavidin immunoglobulin gamma-1 involves Fab unfolding and competing growth pathways mediated by pH and salt concentration.* Biophysical Chemistry, 2013. **172**: p. 26-36.
78. Barnett, G.V., et al., *Acetate- and Citrate-Specific Ion Effects on Unfolding and Temperature-Dependent Aggregation Rates of Anti-Streptavidin IgG1.* Journal of Pharmaceutical Sciences, 2016. **105**(3): p. 1066-1073.
79. Chi, E.Y., et al., *Physical stability of proteins in aqueous solution: mechanism and driving forces in nonnative protein aggregation.* Pharm Res, 2003. **20**(9): p. 1325-36.
80. Hari, S.B., et al., *Acid-Induced Aggregation of Human Monoclonal IgG1 and IgG2: Molecular Mechanism and the Effect of Solution Composition.* Biochemistry, 2010. **49**(43): p. 9328-9338.
81. Lang, B.E. and K.D. Cole, *Differential scanning calorimetry and fluorimetry measurements of monoclonal antibodies and reference proteins: Effect of scanning rate and dye selection.* Biotechnology progress, 2017. **33**(3): p. 677-686.
82. Gaza-Bulseco, G. and H. Liu, *Fragmentation of a Recombinant Monoclonal Antibody at Various pH.* Pharmaceutical Research, 2008. **25**(8): p. 1881-1890.
83. Chakroun, N., et al., *Mapping the Aggregation Kinetics of a Therapeutic Antibody Fragment.* Molecular Pharmaceutics, 2016. **13**(2): p. 307-319.
84. Anderson, D.E., W.J. Bechtel, and F.W. Dahlquist, *pH-Induced Denaturation of Proteins: A Single Salt Bridge Contributes 3-5 kcal/mol to the Free Energy of Folding of T4 Lysozyme.* Biochemistry, 1990. **29**(9): p. 2403-2408.
85. Dasgupta, A. and J.B. Udgaonkar, *Four-state folding of a SH3 domain: Salt-induced modulation of the stabilities of the intermediates and native state.* Biochemistry, 2012. **51**(23): p. 4723-4734.
86. Dill, K.A., et al., *Principles of protein folding — A perspective from simple exact models.* Protein Science, 1995. **4**(4): p. 561-602.
87. Röthlisberger, D., A. Honegger, and A. Plückthun, *Domain interactions in the Fab fragment: a comparative evaluation of the single-chain Fv and Fab format engineered with variable domains of different stability.* Journal of molecular biology, 2005. **347**(4): p. 773-789.
88. Toughiri, R., et al., *Comparing domain interactions within antibody Fabs with kappa and lambda light chains.* MAbs, 2016. **8**(7): p. 1276-1285.
89. Garidel, P. and F. Kebbel, *Protein therapeutics and aggregates characterized by photon correlation spectroscopy.* BioProcess Int, 2010. **8**(3): p. 38-46.
90. Hartl, J., et al., *Characterizing protein–protein-interaction in high-concentration monoclonal antibody systems with the quartz crystal microbalance.* Physical Chemistry Chemical Physics, 2017. **19**(48): p. 32698-32707.
91. Oyama, H., et al., *Relation of Colloidal and Conformational Stabilities to Aggregate Formation in a Monoclonal Antibody.* Journal of Pharmaceutical Sciences, 2020. **109**(1): p. 308-315.

7.3 List of figures

Fig. 2.1: Intrinsic fluorescence emission maxima of a protein	12
Fig. 2.2: Schematic structure and domains of an IgG1	14
Fig. 3.1: IF (a) and DSC (b)	24
Fig. 3.2: Aggregation assay plots	31
Fig. 3.3: Thermal stability derived from SEC of the mAbs at 40 °C and 25 °C	33
Fig. 3.4: Thermodynamics derived from IF and DSC	37
Fig. 4.1: IF and DSC unfolding profiles of the four unfolding clusters	48
Fig. 4.2: IF unfolding profiles recorded by the Prometheus instrument	51
Fig. 4.3: IF unfolding profiles recorded by the NES	52
Fig. 4.4: ΔH_{vh} against E_a	53
Fig. 4.5: Correlation plots of mAb _a to mAb _g and mAb ₄ formulated in F1, F2, and F3 at 25 °C	56
Fig. 4.6: Correlation plots of mAb _a to mAb _g and mAb ₄ formulated in F1, F2, and F3 at 40 °C	59
Fig. 4.7: Correlation plots of the mAb ₁₀ variants solved in citrate buffer at 40 °C	61
Fig. 4.8: Heating rate dependent IF thermograms of mAb _a in F1	63
Fig. 4.9: Correlation plots of mAb _a to mAb _g and mAb ₄ formulated in F1, F2, and F3	65
Fig. 4.10: Correlation plots of the mAb ₁₀ variants formulated in citrate buffer	66
Fig. 5.1: First derivative IF unfolding profile and DSC thermogram of mAb ₁ and mAb _{1b}	76
Fig. 5.2: First derivative IF unfolding profile and DSC thermogram of mAb ₂ and mAb ₃	77
Fig. 5.3: First derivative IF unfolding profile and DSC thermogram of the mAb profile clusters	78
Fig. 5.4: Summarized Asymmetry Factor for the mAbs in F1	80
Fig. 5.5: Heating rate dependent changes in the IF unfolding profiles of mAb ₁ (a), mAb _{1b} (b), mAb ₂ (c), and mAb ₃ (d)	81
Fig. 5.6: Heating rate dependent changes in the IF profiles and DSC for the cluster profiles	82
Fig. 5.7: Heating rate dependent IF profiles using the Prometheus instrument	83
Fig. 5.8: Summarized changes of the amplitudes for different mAb IF thermograms	84
Fig. 6.1: Graphical summary of a thermal stability assessment of mAbs	89

Fig. A.3.1: Fitted DSC thermograms of the used mAbs	103
Fig. A.3.2: DSC analysis for mAba, mAbh, mAbb, and mAb6 in formulation F1	104
Fig. A.3.3: Thermodynamics derived from IF vs. DSC	105
Fig. A.4.1: Cluster profiles in F1, F2, F3, and citrate buffer recorded by the Prometheus	111
Fig. A.4.2: Cluster profiles in F1, F2, F3, and citrate buffer recorded by the NES	112
Fig. A.4.3: IF and DSC profiles for the mAb1 variants in F1 recorded by the Prometheus	113
Fig. A.4.4: IF and DSC profiles for mAb2 to mAb8 in F1 recorded by the Prometheus	114
Fig. A.4.5: IF and DSC profiles for the mAb9 variants in F1 recorded by the Prometheus	115
Fig. A.4.6: IF and DSC profiles for mAbc to mAbg in F1 recorded by the Prometheus	116
Fig. A.4.7: IF and DSC profiles for the mAb10 variants (mAb10 to mAb10d) in citrate buffer in F1 recorded by the Prometheus	117
Fig. A.4.8: IF and DSC profiles for the mAb10 variants (mAb10e to mAb10i) in citrate buffer in F1 recorded by the Prometheus.	118
Fig. A.4.9: IF profiles of the mAb1 variants in F1 recorded by the NES	120
Fig. A.4.10: IF profiles of mAb2 to mAb8 in F1 recorded by the NES	121
Fig. A.4.11: IF profiles of the mAb9 variants in F1 recorded by the NES	122
Fig. A.4.12: IF profiles of mAbc to mAbg in F1 recorded by the NES	123
Fig. A.4.13: IF profiles of the mAb10 variants (mAb10 to mAb10c) in F1 recorded by the NES	124
Fig. A.4.14: IF profiles of the mAb10 variants (mAb10d to mAb10f) in F1 recorded by the NES	125
Fig. A.4.15: IF profiles of the mAb10 variants (mAb10g to mAb10i) in F1 recorded by the NES	126
Fig. A.4.16: Activation energies of mAba to mAbg, mAb4 and mAb5 in F1, F2, and F3	137
Fig. A.5.1: First derivative IF thermograms and DSC for mAb1a (a), mAb1c (b), mAb1d (c), and mAb1e (d) in citrate buffer	140
Fig. A.5.2: Heating rate dependent first derivative IF thermograms for mAb1a (a), mAb1c (b), mAb1d (c), and mAb1e (d) in citrate buffer	141
Fig. A.5.3: First derivative IF and DSC thermograms of the mAb1 variants in F1	142
Fig. A.5.4: First derivative IF and DSC thermograms of mAb2 to mAb8 in F1	143
Fig. A.5.5: First derivative IF and DSC thermograms of the mAb9 variants in F1	144

7.4 List of tables

Tab. 3.1: Thermodynamic and aggregation parameters derived from IF, DSC, and light scattering	25
Tab. 3.2: Thermal stability ranking deduced from different parameters	35
Tab. 4.1: mAb IF profiles classified according to category 1 to 4	50
Tab. A.3.1: Parameters derived from the reversible three-state fit of the IF unfolding traces	101
Tab. A.4.1: Fixed variables for the reversible and irreversible three-state model	107
Tab. A.4.2: Fitting variables of mAba, mAbh, and mAbb in F1	109
Tab. A.4.3: Summary of thermodynamics and kinetics	128
Tab. A.4.4: Parameters derived from the linear regressions for mAba to mAbg and mAb4 in F1, F2, and F3 at 25 °C	133
Tab. A.4.5: Parameters derived from the linear regressions for mAba to mAbg and mAb4 in F1, F2, and F3 at 40 °C	135
Tab. A.4.6: Parameters derived from the linear regressions of the mAb10 variants in citrate buffer at 40 °C	136
Tab. A.4.7: Parameters derived from the linear regressions for mAba to mAbg and mAb4 in F1, F2, and F3 at 25 °C at slow and fast heating	138
Tab. A.4.8: Parameters derived from the linear regressions of the mAb10 variants in citrate buffer at 40 °C at slow and fast heating	139

Appendix

Appendix of Chapter III

A.3.4 Results and discussion

Unfolding and thermodynamic profiling

The IF unfolding profiles of the eight mAbs were fitted by the introduced reversible three-state unfolding model (Eq. 3.3, Chapter III) using OriginPro 2017® (OriginLab Cooperation, Northampton, USA). Fitting was performed by first fixing or defining upper and lower bounds of the parameters like melting temperature, slope, and intercept of the linear regions to initialize the parameters and the fitting curve. For the last iterations, all parameters were chosen as variable (exceptions are listed in the table caption of Tab. A.3.1). Iterations were performed until the fits converged. The fitting parameter describing the quality, the shape, and the thermodynamics of the IF fits are summarized in Tab. A.3.1.

Tab. A.3.1: Parameters derived from the reversible three-state fit of the IF unfolding traces. IF unfolding profiles (Fig. 3.1a, Chapter III) were fitted by using Eq. 3.3 (Chapter III). The intercepts Y_{i0} and the slopes S_i of the linear areas are symbolized for the three states with F (folded state), I (intermediate state), and U (unfolded state), respectively. The transitions of the IF thermograms are characterized by the melting temperature (T_m) and the van't Hoff enthalpy (ΔH_{vh}) for the first and second transition. Standard errors were calculated by the software. The slope of the folded state (S_F) was fixed to zero for mAb1 to mAb1e to have a consistent fitting for the similar unfolding profiles. Additionally, the slope of the unfolded state (S_U) for mAb1a was fixed to zero. The parameter $T_m(2)$ was fixed to the transition midpoint to fit the small second transition for all mAbs showing the Fab transition within the first transition (mAb1 to mAb1e and mAb3).

	mAb1	mAb1a	mAb1b	mAb1c	mAb1d	mAb1e	mAb2	mAb3
Chi-square-reduced	12.6	19.8	6.96	8.20	1.76	10.5	2.87	0.58
R-square	0.999	0.999	0.999	0.999	0.999	0.999	0.999	0.999
Y_{F0}	$0.68 \pm 4.1 \cdot 10^{-5}$	$0.68 \pm 6.6 \cdot 10^{-5}$	$0.68 \pm 3.4 \cdot 10^{-5}$	$0.68 \pm 1.6 \cdot 10^{-5}$	$0.69 \pm 1.1 \cdot 10^{-4}$	$0.68 \pm 2.8 \cdot 10^{-5}$	$0.48 \pm 4.3 \cdot 10^{-4}$	$0.76 \pm 1.7 \cdot 10^{-3}$
$S_F / 1 \cdot K^{-1}$	0	0	0	0	0	0	$8.1 \cdot 10^{-4} \pm 1.4 \cdot 10^{-6}$	$-1.3 \cdot 10^{-4} \pm 5.5 \cdot 10^{-6}$
$\Delta H_{vh}(1) / kJ \cdot mol^{-1}$	544 ± 3.5	715 ± 5.5	505 ± 3.3	534 ± 2.2	571 ± 4.8	615 ± 3.9	528 ± 7.6	757 ± 5.7
$T_m(1) / K$	339.3 ± 0.03	340.9 ± 0.02	342.7 ± 0.14	341.7 ± 0.03	341.0 ± 0.02	341.6 ± 0.03	343.9 ± 0.21	343.8 ± 0.02

Y_{10}	1.2 ± 0.03	1.7 ± 0.02	0.29 ± 0.18	1.4 ± 0.04	1.2 ± 0.02	1.2 ± 0.04	-0.052 ± 0.09	1.6 ± 0.03
$S_1 / 1 \cdot K^{-1}$	$-1.1 \cdot 10^{-3} \pm 8.6 \cdot 10^{-5}$	$-2.5 \cdot 10^{-3} \pm 4.9 \cdot 10^{-5}$	$1.4 \cdot 10^{-3} \pm 5.1 \cdot 10^{-4}$	$-1.7 \cdot 10^{-3} \pm 1.3 \cdot 10^{-4}$	$-1.3 \cdot 10^{-3} \pm 5.2 \cdot 10^{-5}$	$-1.1 \cdot 10^{-3} \pm 1.1 \cdot 10^{-4}$	$2.5 \cdot 10^{-3} \pm 2.7 \cdot 10^{-4}$	$-2.1 \cdot 10^{-3} \pm 7.7 \cdot 10^{-5}$
$\Delta H_{wh(2)} / kJ \cdot mol^{-1}$	638 ± 34	504 ± 11	686 ± 46	608 ± 38	760 ± 24	617 ± 31	1049 ± 57	721 ± 26
$T_m(2) / K$	355	355	354.4 ± 0.19	355	354	355	355.4 ± 0.09	354
Y_{U0}	0.72 ± 0.02	$0.83 \pm 1.8 \cdot 10^{-4}$	1.2 ± 0.02	0.71 ± 0.03	0.59 ± 0.01	0.75 ± 0.02	0.79 ± 0.01	$0.37 \pm 8.9 \cdot 10^{-3}$
$S_U / 1 \cdot K^{-1}$	$3.0 \cdot 10^{-4} \pm 6.2 \cdot 10^{-5}$	0	$-1.1 \cdot 10^{-3} \pm 5.3 \cdot 10^{-5}$	$3.4 \cdot 10^{-4} \pm 7.0 \cdot 10^{-5}$	$6.6 \cdot 10^{-4} \pm 2.3 \cdot 10^{-5}$	$2.3 \cdot 10^{-4} \pm 6.0 \cdot 10^{-5}$	$2.2 \cdot 10^{-4} \pm 2.2 \cdot 10^{-5}$	$1.4 \cdot 10^{-3} \pm 2.4 \cdot 10^{-5}$

DSC thermograms were fitted to simulate the not fully separated transitions and signal areas were determined by integration to obtain ΔH_{cal} for each transition. For mAb1a and mAb3, a PearsonVII function was found to fit the DSC curves best. For the remaining mAbs, a Bigauss function was chosen to determine the signal areas. Fitting and integration were analyzed by the software OriginPro 2017[®] for the single thermograms of a duplicate and the respective plots of one duplicate are shown in Fig. A.3.1. The determined parameters derived from the DSC thermograms are listed in Tab. 3.1 (Chapter III).

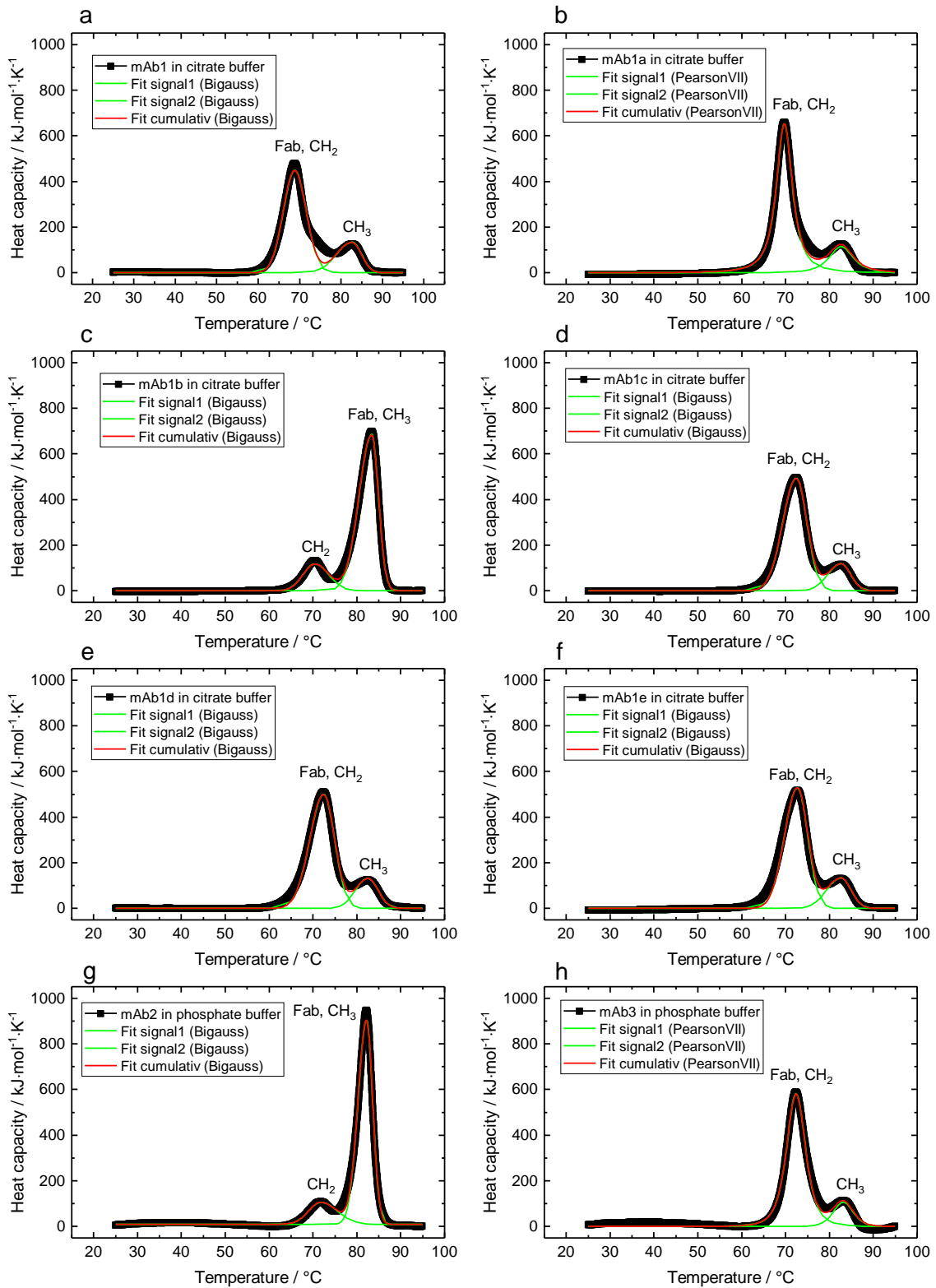


Fig. A.3.1: Fitted DSC thermograms of the used mAbs. Shown is one example of a duplicate, respectively. The signals of the DSC plots (black) were fitted by appropriate functions (Bigauss or PearsonVII) simulating the progress of the not fully separated signals. The curves of the single transition signals are illustrated with green lines. The respective cumulative fit is illustrated by a red line.

Subtopic – Comparison of additional IF vs. DSC thermodynamics

To evaluate and compare ΔH_{vh} values determined from IF and DSC, the 24 mAb samples formulated in F1 and the ten mAb10 variants in citrate buffer were analyzed (introduced in Chapter IV). DSC thermograms were evaluated according to the described method in Chapter III. Exemplarily, the DSC thermograms of mAba, mAbh, mAbb, and mAb6 are shown (Fig. A.3.2) representing the four introduced IF unfolding categories in Chapter IV.

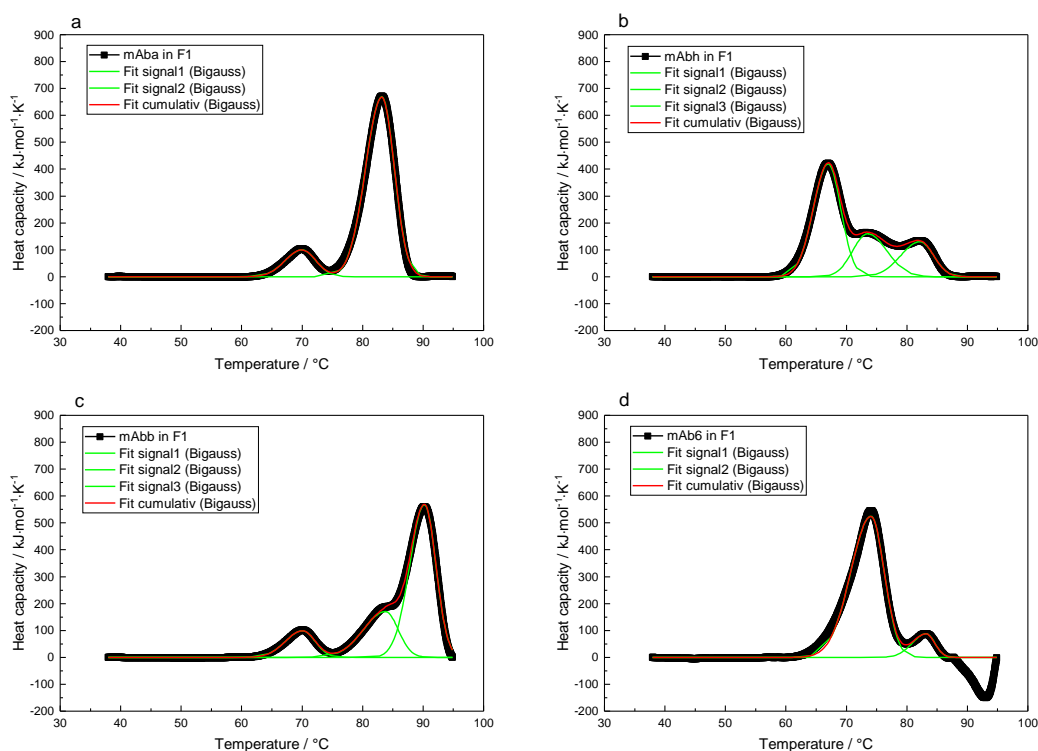


Fig. A.3.2: DSC analysis for mAba (a), mAbh (b), mAbb (c), and mAb6 (d) in formulation F1. The thermograms recorded by a capillary based DSC as single measurements are exemplarily shown for the mAbs representing the four different IF profile cluster. Integration of the signal areas and evaluation was performed according to the described way in Chapter III.

As described above, a Bigauss fit function was used to simulate the not fully resolved DSC thermograms to determine the area under the curve of the respective transitions. Due to the fact that mAbh shows three transitions in the DSC thermogram, three signals were integrated. This is contrary to the IF thermogram of mAbh, where only two transitions are resolved, and a three-state fit function is applied (compare Chapter IV). In the case of mAb6, the IF thermogram cannot be analyzed by the

three-state fit function due to the wave-shaped profile, but an evaluation of the DSC thermodynamics is possible. These examples illustrate, that the resolution of IF and DSC can be different regarding their apparent transitions. For those cases, where the determined thermodynamics can be compared for both methods, the values are summarized in Fig. A.3.3.

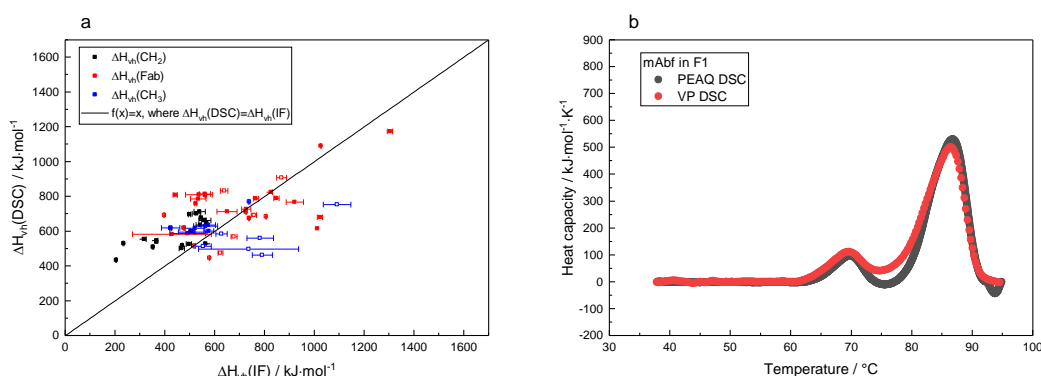


Fig. A.3.3: Thermodynamics derived from IF vs. DSC. ΔH_{vh} determined from IF analysis using the reversible three-state model is compared to ΔH_{vh} determined from DSC. Values of ΔH_{vh} were analyzed from the CH₂-domain (black), the Fab (red), and the CH₃-domain (blue) for the 24 mAbs in F1 and the mAb10 variants in citrate buffer, where a three-state can be applied (a). For the two different types of DSC measurements used for analysis, closed symbols represent a capillary based DSC device (PEAQ- and VP-capillary-DSC), while open symbols stand for a DSC device based on a measuring cell (VP-DSC). (b) Comparison of a DSC thermogram derived from a capillary based DSC device (PEAQ DSC) vs. a DSC analysis from a measuring cell (VP-DSC) both determined as a single measurement.

As depicted in Fig. A.3.3, the ΔH_{vh} values determined by IF and DSC show similar magnitudes for most of the analyzed mAbs. Indeed, the deviations between both methods are larger than observed in Chapter III. However, larger differences for these mAbs can be explained by worse experimental conditions than the experiments before. Due to an outage of the automated capillary based PEAQ-DSC device, some DSC thermograms had to be recorded by a measuring cell based VP-DSC device and data from another capillary based DSC (VP-capillary-DSC) had also be used for analysis. Due to the very low sample throughput of the VP-DSC device, the determination of DSC was performed as single measurement. Therefore, a deviation of the DSC thermodynamics here cannot be estimated. Moreover, thermodynamic values for the two different kinds of DSC devices can deviate due to the different heating cell geometries of the DSC devices. Therefore, thermodynamics determined from the two capillary based devices were distinguished to the measuring cell based device in

Fig. A.3.3a. One example illustrating the device dependent differences is shown in Fig. A.3.3b. While the melting temperatures show comparable values, the area under the curve shows differences. Therefore, the determined ΔH_{vh} values show differences especially for the smaller first transition representing the CH₂-domain of mAbf. From the capillary based DSC (PEAQ-DSC), a $\Delta H_{vh}(\text{CH}_2)$ for mAbf of 714 kJ·mol⁻¹ was determined, while 524 kJ·mol⁻¹ can be analyzed by the measuring cell based VP-DSC device. For the Fab (second transition), a $\Delta H_{vh}(\text{Fab})$ of 620 kJ·mol⁻¹ can be determined by the PEAQ-DSC device, while an analysis with the VP-DSC device revealed 587 kJ·mol⁻¹. For mAbf, the thermodynamics determined by the VP-DSC device show a higher accordance to the IF thermodynamics than the values obtained from the PEAQ-DSC device. A conclusion which DSC device shows a higher accordance to the IF thermodynamics for all tested mAbs cannot be made, because different mAbs and therefore different profiles were investigated by the DSC devices. In summary, a quantitative thermodynamic DSC analysis of the investigated mAbs in F1 formulation has to be handled with care and is underlain with higher uncertainties, but gives the hint that thermodynamics derived from IF and DSC show similar magnitudes as investigated in Chapter III. A qualitative analysis regarding the temperature range of the transitions and the use of DSC for assignment of IF transitions is possible in any case and comparable for the DSC devices.

Appendix of Chapter IV

A.4.3 Material and methods

To obtain suitable fittings for the reversible and irreversible three-state fit function (Eq. 3.3, Chapter III and Eq. 4.9, Chapter IV), some of the fit variables were fixed. For the three-state fit functions, the fixed variables are summarized in Tab. A.4.1.

Tab. A.4.1: Fixed variables for the reversible and irreversible three-state model. For the applied fits, the respective variables, which were fixed to obtain suitable curve fittings, are listed and justified. For the mAbs showing a four-state IF unfolding profile according to category 3, two three-state fits were applied. Fitting at faster heating rates of $18 \text{ K}\cdot\text{min}^{-1}$ and $30 \text{ K}\cdot\text{min}^{-1}$ was performed with the same fixed variables (exceptions: mAbc and mAbc with only a fixed $m_{D1}=0$ variable due to the higher resolution between the two transitions at faster heating rates. mAbf was fitted with additionally fixed $m_{D2}=0$ variable caused by the large shift of the second transition towards the end temperature of $95 \text{ }^\circ\text{C}$).

Sample	Fixed variables for the reversible three-state model (Eq. 3.3)	Fixed variables for irreversible three-state model (Eq. 4.9)	Rationale
mAb1 in F1 and F2 mAb1a, mAb1c, mAb1d, mAb1e in F1; mAb3 in citrate buffer	fixed $T_m(2)$	-	small 2. transition
mAb1, mAb1a, mAb1c, mAb1d, mAb1e in F3; mAb3 in F2	fixed $T_m(2)$; $S_u = 0$	-	small 2. transition
mAb1, mAb1a, mAb1c, mAb1d, mAb1e in citrate buffer	according to Tab. A.3.1	$m_{D1} = 0$	small 2. transition
mAb1a, mAb1c, mAb1d, mAb1e in F2; mAb5, mAbh in F1, F2, F3, and citrate buffer; mAb10a, mAb10d, mAb10h in citrate buffer	-	-	-
mAb1b in citrate buffer	according to Tab. A.3.1	$m_{D1} = 0$	not fully separated transitions
mAb1b in F1, F2, F3; mAb2, mAb4, mAbf, mAbg in F1, F2, F3, and citrate buffer; mAbc in F1, F2, and F3	$S_i = 0$	$m_{D1} = 0$	not fully separated transitions
mAb9a and mAb10b in citrate buffer	$S_i = 0$	-	not fully separated transitions
mAb9b in F1	fixed $T_m(2)$	$m_{D1} = 0$	small 2. transition

mAb9b in F3 and citrate buffer	-	$m_{D_1} = 0$	small 2. transition	
mAbc in F1, F2, and F3	fixed $T_m(1)$; $S_i = 0$	fixed $c_{D_1 0}$; $m_{D_1} = 0$	not fully separated transitions	
mAba and mAbc in citrate buffer	fixed $T_m(1)$; $S_i = 0$	$m_{D_1} = 0$	not fully separated transitions	
mAbd in F1, F2, F3, and citrate buffer	fixed $T_m(1)$; $S_i = 0$	$m_{D_1} = 0$	not fully separated transitions, with small 1. transition	
mAbe in F1, F2, and F3	fixed $T_m(1)$; fixed Y_{10} ; $S_i = 0$	fixed $c_{D_1 0}$; $m_{D_1} = 0$	not fully separated transitions, with small 1. transition	
mAbb in F1 and F2; mAb10, mAb10e, mAb10f, mAb10g, mAb10i in citrate buffer	1. Fit 2. Fit	$S_i = 0$; $S_U = 0$ $S_F = 0$; $S_i = 0$	$m_{D_1} = 0$; $m_{D_2} = 0$ $m_F = 0$; $m_{D_1} = 0$	not fully separated transitions and consistent approach to describe the 4-state unfolding profile
mAb10c in citrate buffer	1. Fit 2. Fit	$S_i = 0$; $S_U = 0$ $S_F = 0$; $S_i = 0$; $S_U = 0$; fixed $T_m(1)$	$m_{D_1} = 0$; $m_{D_2} = 0$ $m_F = 0$; $m_{D_1} = 0$	not fully separated transitions and consistent approach to describe the 4-state unfolding profile
mAbb in F3	1. Fit 2. Fit	$S_i = 0$; $S_U = 0$ $S_F = 0$; $S_i = 0$; $S_U = 0$	$m_{D_1} = 0$; $m_{D_2} = 0$ $m_F = 0$; $m_{D_1} = 0$	not fully separated transitions and consistent approach to describe the 4-state unfolding profile
mAbb in citrate buffer	1. Fit 2. Fit	$S_i = 0$; $S_U = 0$; fixed $T_m(2)$ $S_F = 0$; $S_i = 0$; fixed $T_m(1)$	$m_{D_1} = 0$; $m_{D_2} = 0$ $m_F = 0$; $m_{D_1} = 0$	not fully separated transitions and consistent approach to describe the 4-state unfolding profile

A.4.4 Results

Kinetic and thermodynamic characterization of various mAb formulations

All fitted variables for the mAbs in F1 exemplarily shown for the different IF profile categories from the reversible (Eq. 3.3) and the irreversible (Eq. 4.9) three-state model are summarized in Tab. A.4.2.

Tab. A.4.2: Fitting variables of mAb_a, mAb_b, and mAb_c in F1. For the exemplarily shown fitted IF thermograms of the mAbs in F1 representing the different IF profile categories (Fig. 4.2 and Fig. 4.3, Chapter IV) all fitting variables and standard errors are summarized. On the top of the table, fitting variables deduced from the reversible three-state model (Eq. 3.3) are shown. At the bottom, the fitting variables of the irreversible three-state model (Eq. 4.9) are depicted. Shown are the fit variables from one example of a duplicate measurement.

	mAb _a (category 1)	mAb _b (category 2)	mAb _c (Fit1) (category 3)	mAb _c (Fit2) (category 3)
Y_{F0}	$0.63 \pm 2.9 \cdot 10^{-3}$	$0.58 \pm 1.7 \cdot 10^{-3}$	$0.53 \pm 1.7 \cdot 10^{-3}$	$0.63 \pm 3.5 \cdot 10^{-4}$
$S_F / 1 \cdot K^{-1}$	$-2.0 \cdot 10^{-6} \pm 9.0 \cdot 10^{-6}$	$2.9 \cdot 10^{-4} \pm 5.3 \cdot 10^{-6}$	$1.7 \cdot 10^{-4} \pm 5.4 \cdot 10^{-6}$	0 (fixed)
$\Delta H_{vh(1)} /$ $kJ \cdot mol^{-1}$	426 ± 6.8	739 ± 3.3	530 ± 7.6	438 ± 10
$T_m(1) / K$	342.2 ± 0.05	339.5 ± 0.03	341.4 ± 0.04	355.5 ± 0.15
Y_{I0}	$0.68 \pm 3.8 \cdot 10^{-4}$	1.4 ± 0.07	$0.63 \pm 2.7 \cdot 10^{-4}$	$0.71 \pm 2.5 \cdot 10^{-3}$
$S_I / 1 \cdot K^{-1}$	0 (fixed)	$-1.7 \cdot 10^{-3} \pm 1.9 \cdot 10^{-4}$	0 (fixed)	0 (fixed)
$\Delta H_{vh(2)} /$ $kJ \cdot mol^{-1}$	726 ± 5.3	449 ± 22	438 ± 7.2	755 ± 9.3
$T_m(2) / K$	354.8 ± 0.01	352.0 ± 0.17	356.3 ± 0.10	363.5 ± 0.09
Y_{U0}	0.55 ± 0.02	0.81 ± 0.02	$0.72 \pm 1.8 \cdot 10^{-3}$	4.4 ± 0.44
$S_U / 1 \cdot K^{-1}$	$8.0 \cdot 10^{-4} \pm 5.1 \cdot 10^{-5}$	$1.2 \cdot 10^{-5} \pm 4.6 \cdot 10^{-5}$	0 (fixed)	$9.7 \cdot 10^{-3} \pm 1.2 \cdot 10^{-3}$
C_{F0}	$0.68 \pm 1.8 \cdot 10^{-3}$	$0.63 \pm 1.4 \cdot 10^{-3}$	$0.56 \pm 1.2 \cdot 10^{-3}$	$0.71 \pm 3.1 \cdot 10^{-4}$
$m_F / 1 \cdot K^{-1}$	$6.3 \cdot 10^{-5} \pm 5.5 \cdot 10^{-6}$	$3.7 \cdot 10^{-4} \pm 4.5 \cdot 10^{-6}$	$3.2 \cdot 10^{-4} \pm 3.8 \cdot 10^{-6}$	0 (fixed)
$E_a(1) / kJ \cdot mol^{-1}$	329 ± 2.4	497 ± 1.6	386 ± 3.2	349 ± 5.2
$A(1) / 1 \cdot K^{-1}$	$e^{115} \pm e^{0.87}$	$e^{176} \pm e^{0.55}$	$e^{135} \pm e^{1.1}$	$e^{118} \pm e^{1.8}$
C_{D10}	$0.76 \pm 1.5 \cdot 10^{-4}$	0.76 ± 0.02	$0.70 \pm 1.9 \cdot 10^{-4}$	$0.77 \pm 5.9 \cdot 10^{-4}$
$m_{D1} / 1 \cdot K^{-1}$	0 (fixed)	$3.3 \cdot 10^{-4} \pm 4.8 \cdot 10^{-5}$	0 (fixed)	0 (fixed)

$E_a(2) / \text{kJ}\cdot\text{mol}^{-1}$	416 ± 1.2	451 ± 15	281 ± 2.7	526 ± 3.3
$A(2) / 1\cdot\text{K}^{-1}$	$e^{140} \pm e^{0.42}$	$e^{153} \pm e^{5.1}$	$e^{93.8} \pm e^{0.92}$	$e^{174} \pm e^{1.1}$
c_{D_20}	$0.45 \pm 6.7\cdot 10^{-3}$	$0.79 \pm 4.9\cdot 10^{-3}$	$0.80 \pm 8.3\cdot 10^{-4}$	1.2 ± 0.04
$m_{D_2} / 1\cdot\text{K}^{-1}$	$1.4\cdot 10^{-3} \pm 1.8\cdot 10^{-5}$	$3.0\cdot 10^{-4} \pm 1.4\cdot 10^{-5}$	0 (fixed)	$7.8\cdot 10^{-4} \pm 1.2\cdot 10^{-4}$

The IF unfolding thermograms and the respective fits using the reversible three-state model (Fig. A.4.1) and the irreversible three-state model (Fig. A.4.2) are exemplarily depicted for mAba, mAbh, and mAbb in all four formulations F1, F2, F3, and citrate buffer. Due to the similar shape and the fact that mAb6 (category 4) cannot be described by both three-state models, only the IF plots in the four formulations recorded by the Prometheus instrument are illustrated (Fig. A.4.1). IF unfolding profiles of mAb6 in F1, F2, F3, and citrate buffer show a similar wave-shaped profile using the NES.

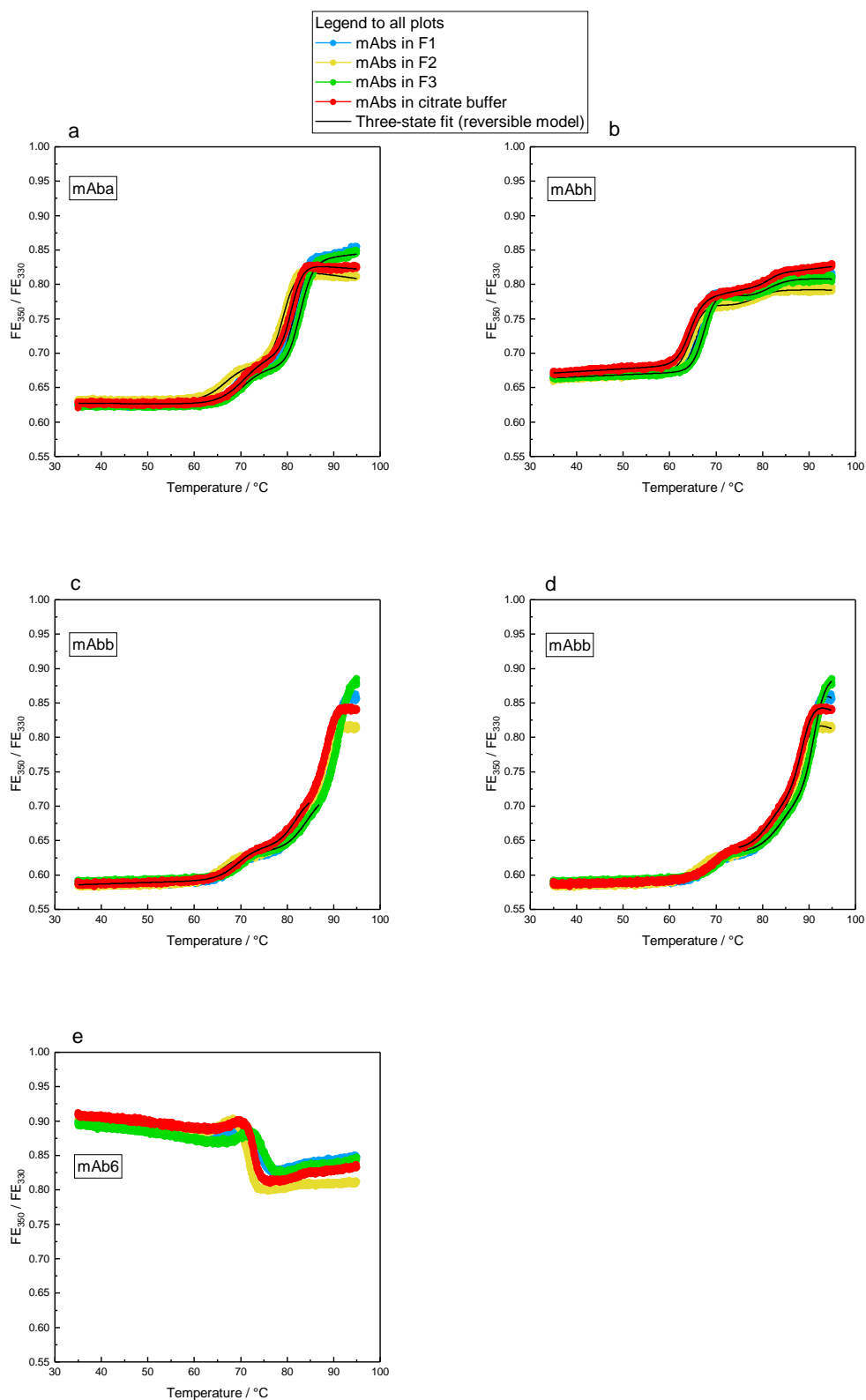


Fig. A.4.1: Cluster profiles in F1, F2, F3, and citrate buffer recorded by the Prometheus. FE_{350}/FE_{330} signal vs. temperature. The IF thermograms and the respective reversible three-state fit model (Eq. 3.3, black line) are exemplarily depicted for the four used formulations F1 (blue), F2 (yellow), F3 (green), and citrate buffer (red). For the IF profile category 1, mAba is shown in (a), mAbh (b) is shown for category 2, and mAbb ((c) and (d)) for category 3. For mAb6 (e) (category 4), the three-state model cannot be used for a reliable fit to simulate the wave-shaped profile. Shown is one example of a duplicate, respectively.

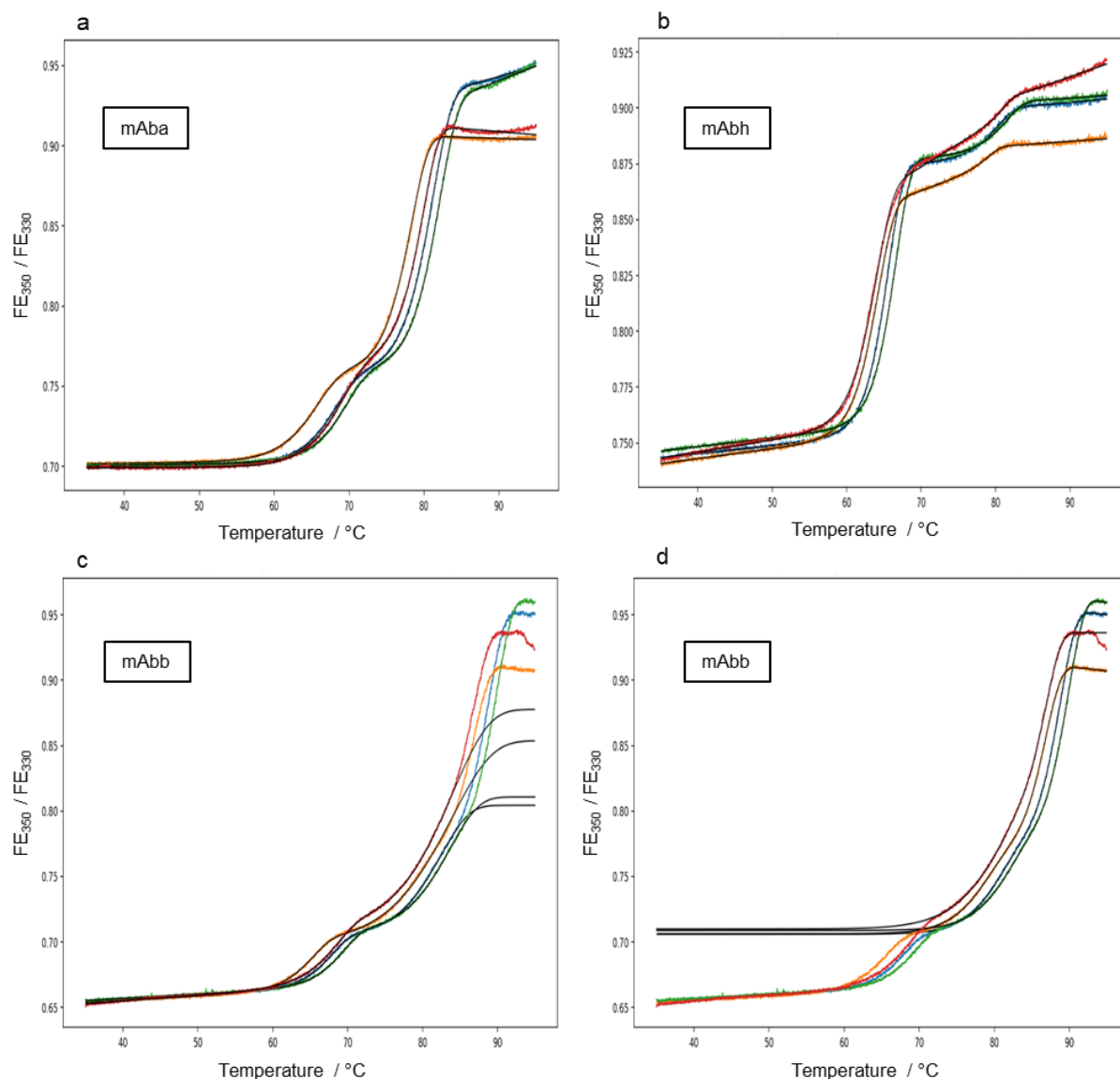


Fig. A.4.2: Cluster profiles in F1, F2, F3, and citrate buffer recorded by the NES. FE_{350} / FE_{330} signal vs. temperature. For category 1 to 3, mAba (a), mAbh (b), and mAbb ((c) and (d)) are shown for the four formulations (F1 (blue), F2 (yellow), F3 (green), and citrate buffer (red)). The irreversible three-state model (Eq. 4.9, black line) was used to fit the IF profiles. Shown is one example of a duplicate, respectively.

For each remaining mAb, the IF thermogram recorded by the Prometheus instrument and reversible three-state fit (Eq. 3.3, Chapter III) of one formulation is exemplarily shown due to the similar shape of the profiles for different formulations (Fig. A.4.3 to Fig. A.4.8). To assign the respective IF transitions to a certain mAb domain, the DSC thermograms are depicted additionally.

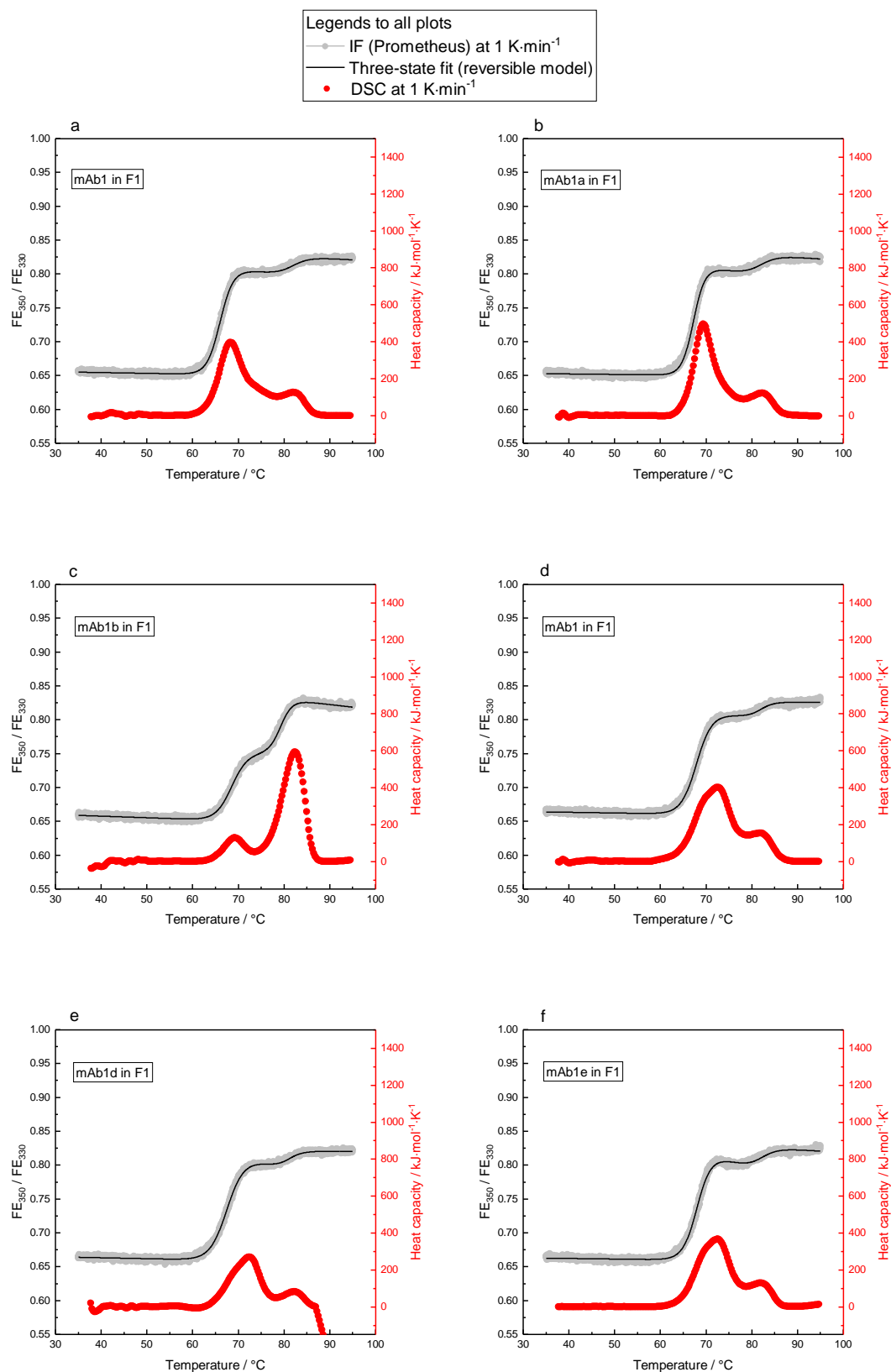


Fig. A.4.3: IF and DSC profiles for the mAb1 variants in F1 recorded by the Prometheus. The FE₃₅₀ / FE₃₃₀ signal is plotted against the temperature. For the six mAb1 variants, the IF profiles were recorded at 1 K·min⁻¹ using the Prometheus instrument. The reversible three-state model (Eq. 3.3, black line) was used to fit the respective IF profile (gray). Shown is one example of a duplicate, respectively. To assign the IF transitions to a certain mAb region, DSC thermograms are shown for comparison (red).

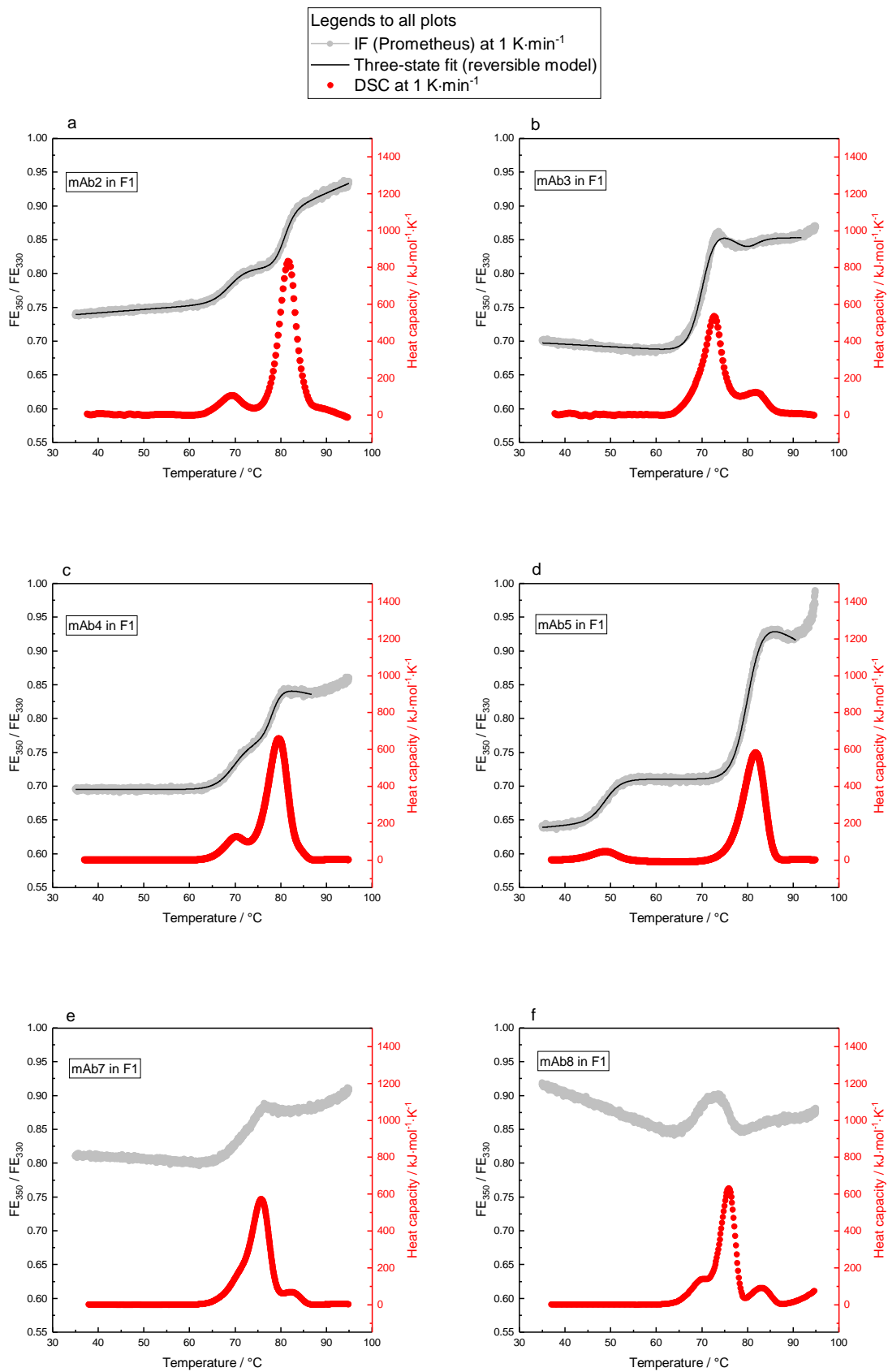


Fig. A.4.4: IF and DSC profiles for mAb2 to mAb8 in F1 recorded by the Prometheus. For description, see caption of Fig. A.4.3.

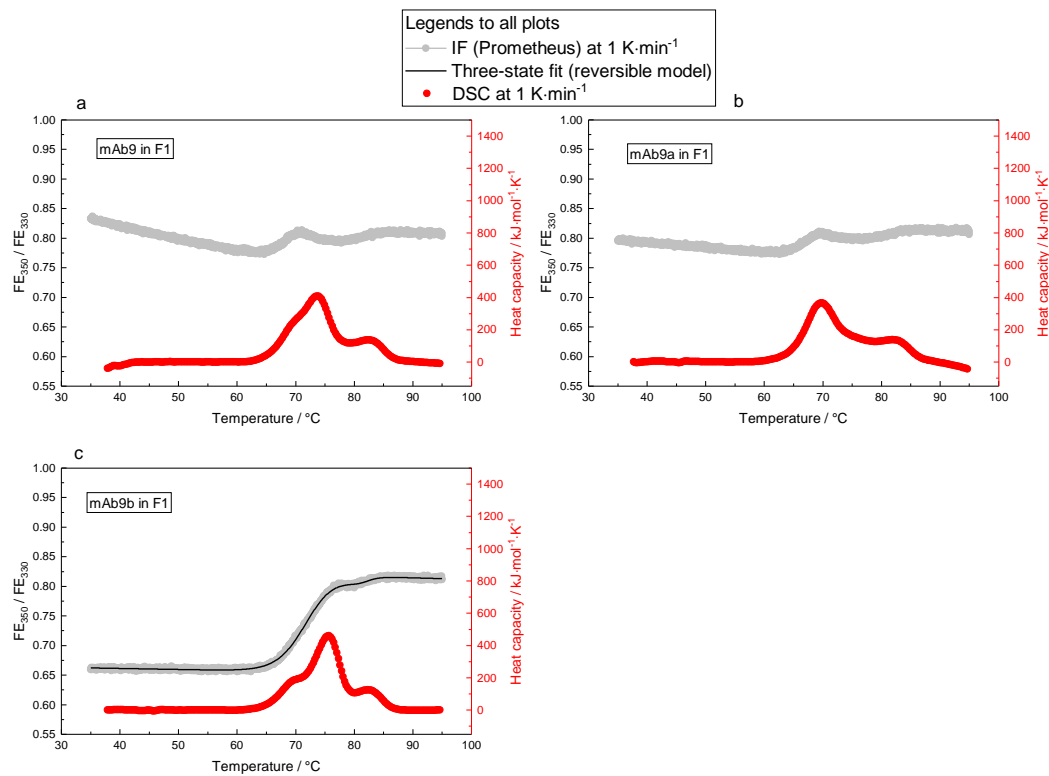


Fig. A.4.5: IF and DSC profiles for the mAb9 variants in F1 recorded by the Prometheus. For description, see caption of Fig. A.4.3.

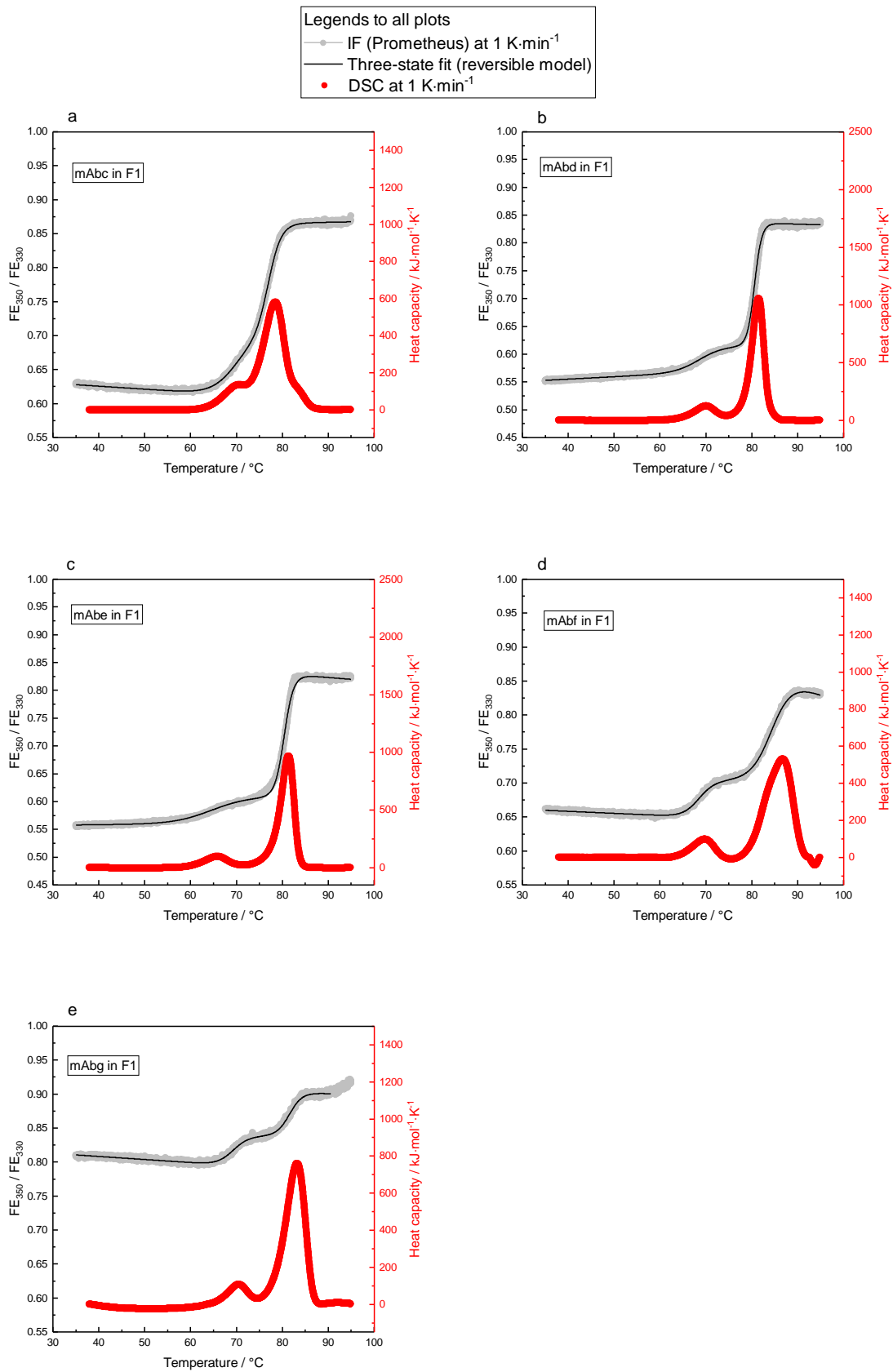


Fig. A.4.6: IF and DSC profiles for mAbc to mAbg in F1 recorded by the Prometheus. For description, see caption of Fig. A.4.3.

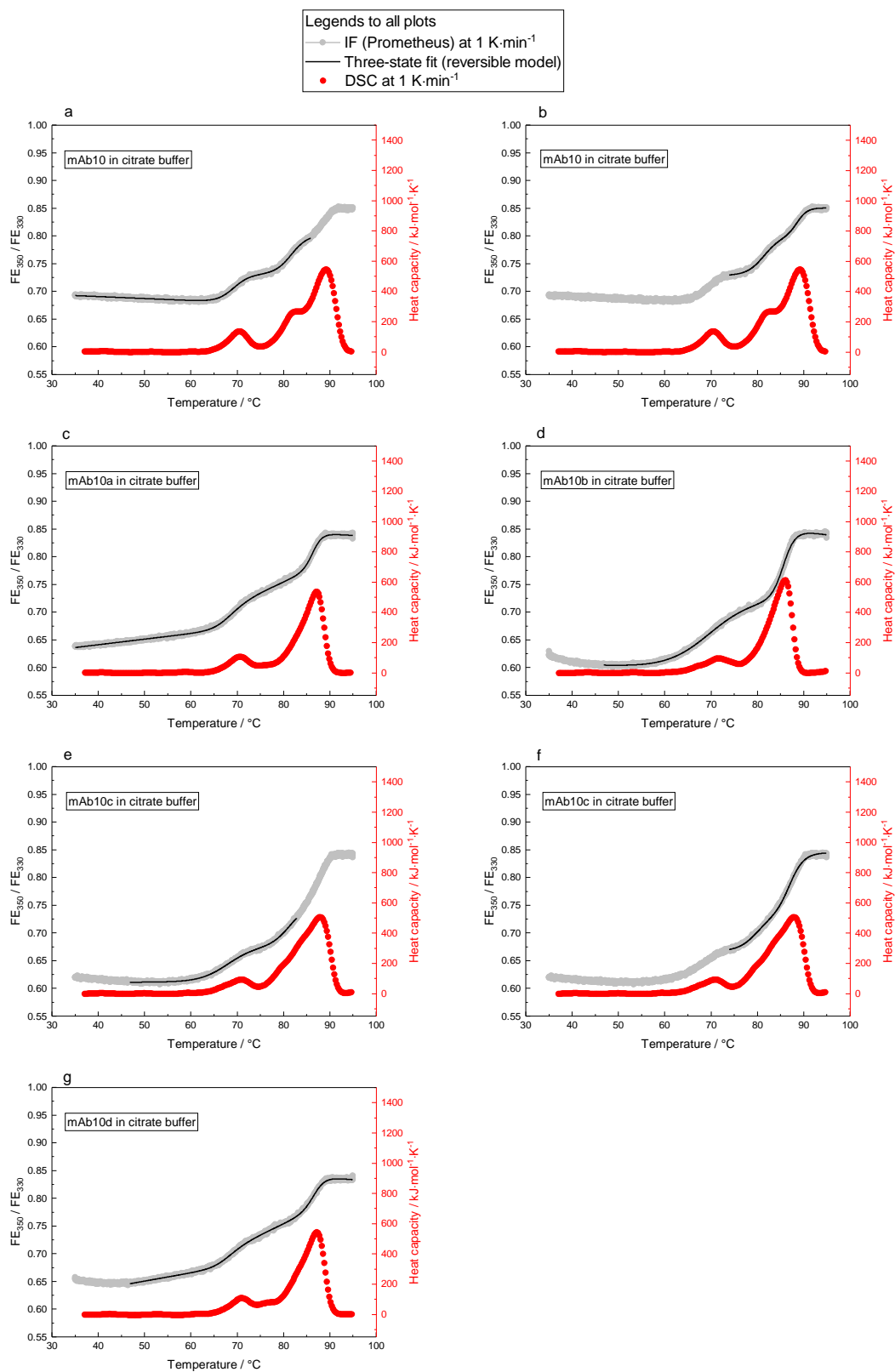


Fig. A.4.7: IF and DSC profiles for the mAb10 variants (mAb10 to mAb10d) in citrate buffer in F1 recorded by the Prometheus. For description, see caption of Fig. A.4.3. For IF profiles showing four apparent transition, the reversible three-state fit was used two times.

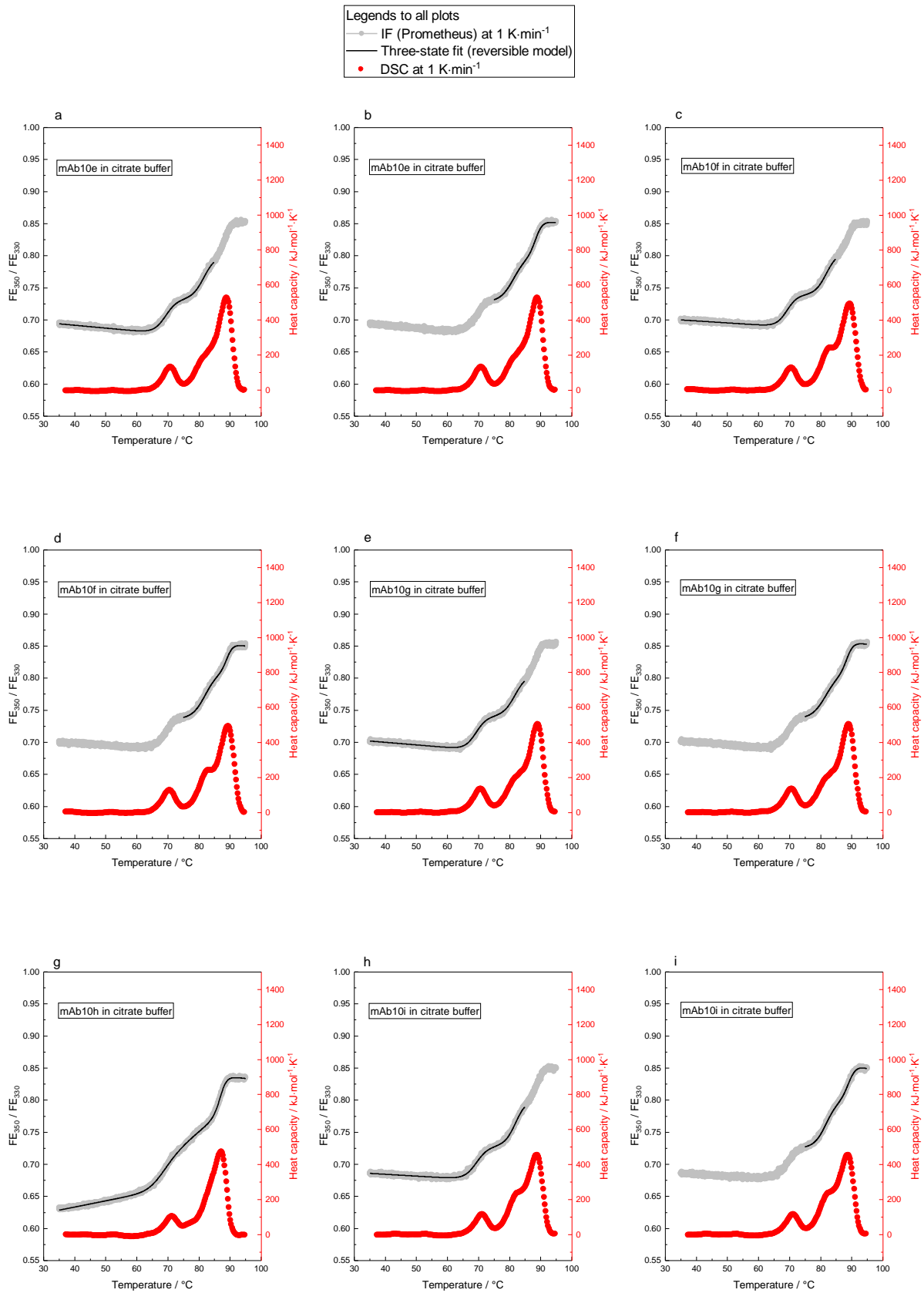


Fig. A.4.8: IF and DSC profiles for the mAb10 variants (mAb10e to mAb10i) in citrate buffer in F1 recorded by the Prometheus. For description, see caption of Fig. A.4.3. For IF profiles showing four apparent transition, the reversible three-state fit was used two times.

For each mAb formulated in F1, the IF thermogram recorded by the NES at $1 \text{ K}\cdot\text{min}^{-1}$ is exemplarily shown (Fig. A.4.9 to Fig. A.4.15). The IF thermogram was fitted using the irreversible three-state fit model (Eq. 4.9, Chapter IV).

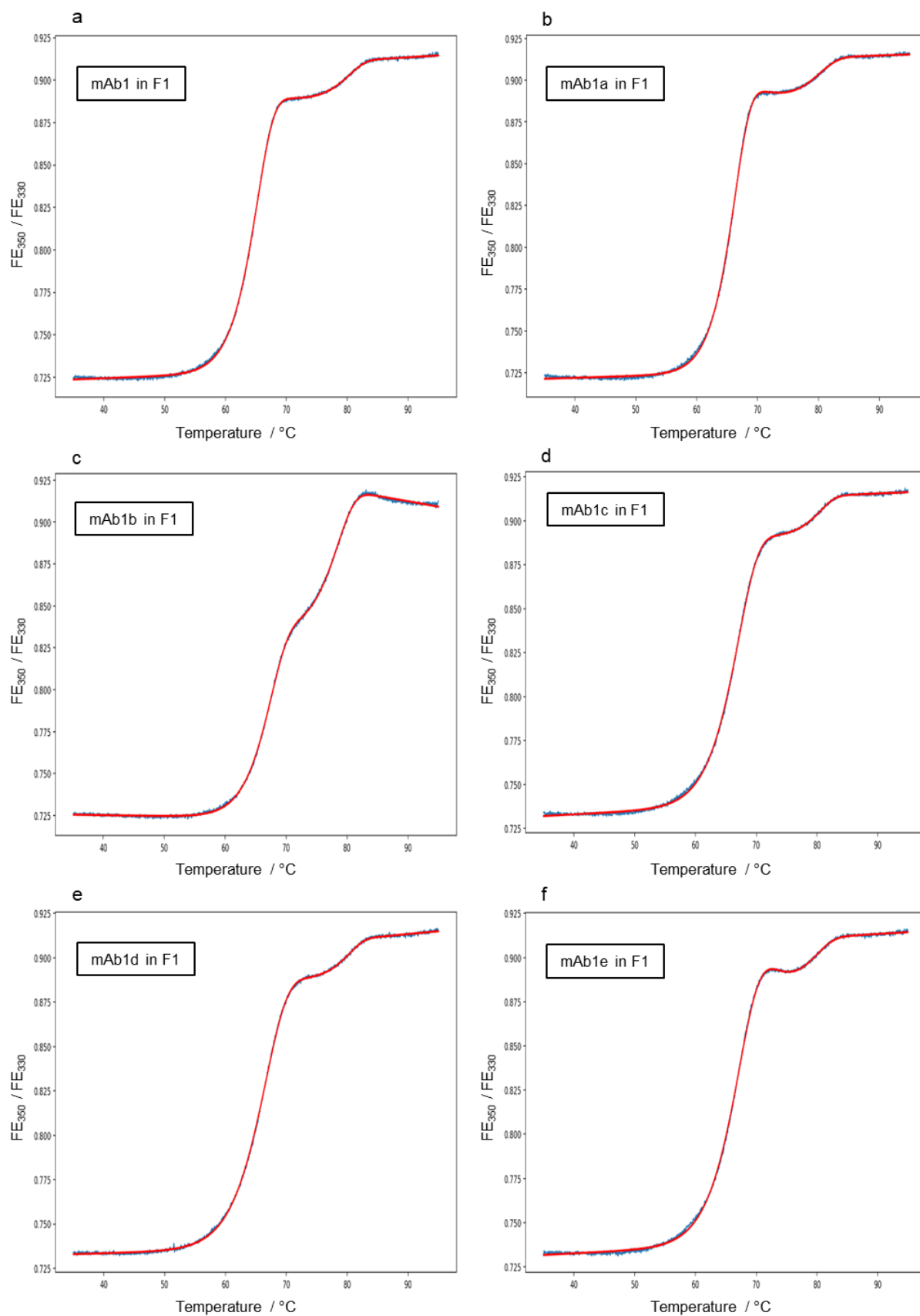


Fig. A.4.9: IF profiles of the mAb1 variants in F1 recorded by the NES. For the six mAb1 variants, the IF profiles were recorded at $1 \text{ K} \cdot \text{min}^{-1}$ using the NES. The FE_{350} / FE_{330} signal is plotted against the temperature. The irreversible three-state model (Eq. 4.9, red line) was used to fit the respective IF profile (blue). Shown is one example of a duplicate, respectively.

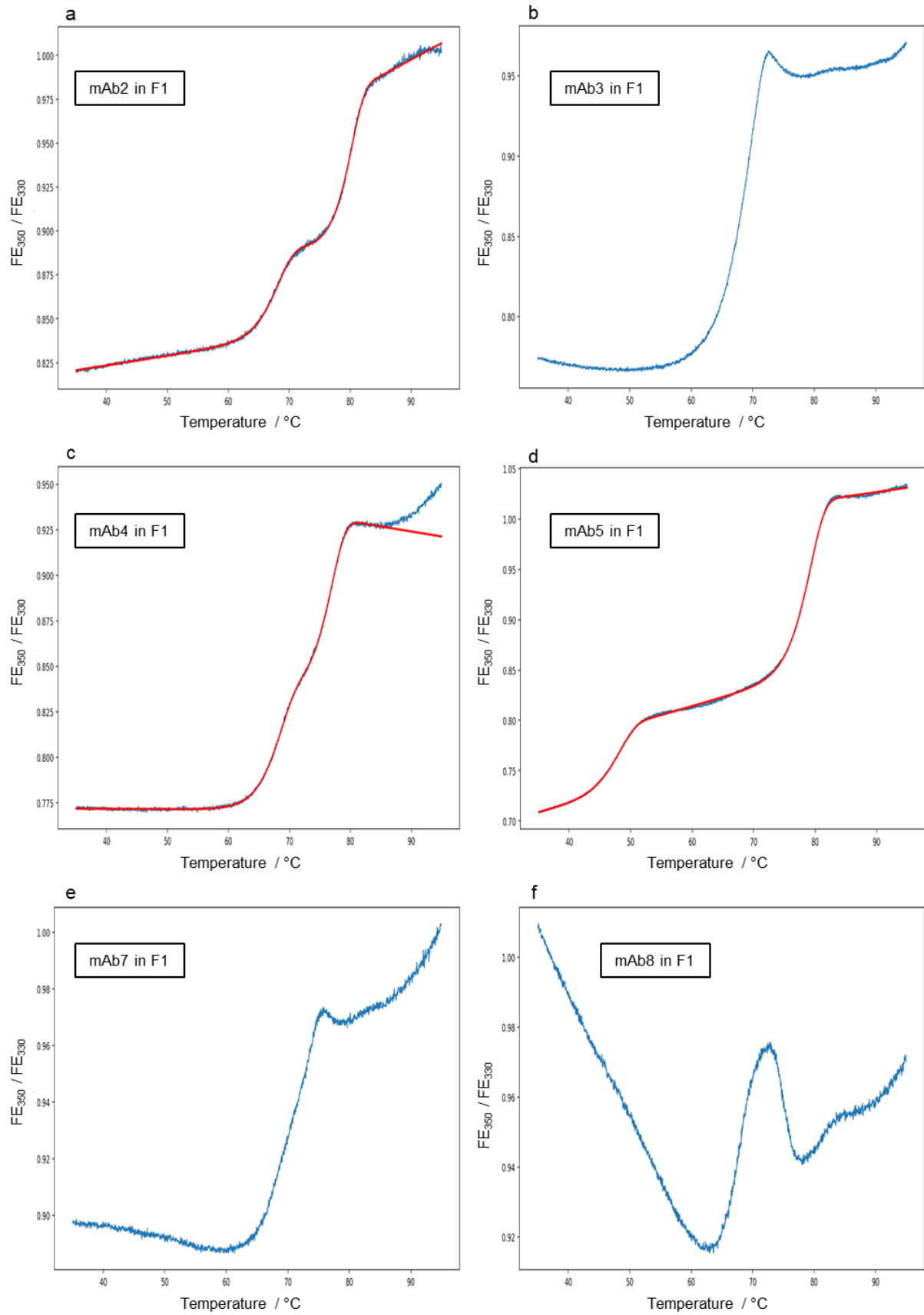


Fig. A.4.10: IF profiles of mAb2 to mAb8 in F1 recorded by the NES. For description, see caption of Fig. A.4.9.

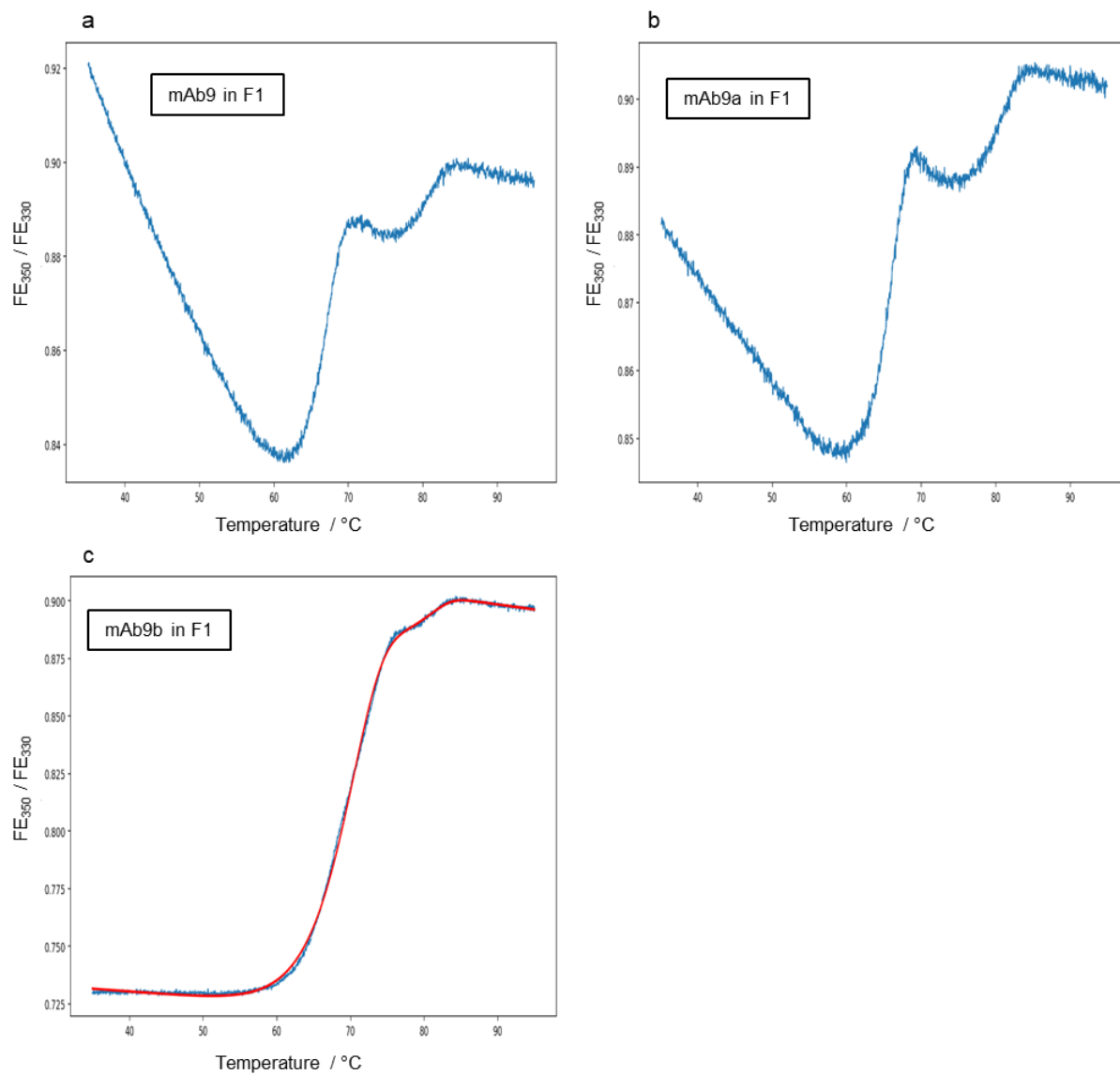


Fig. A.4.11: IF profiles of the mAb9 variants in F1 recorded by the NES. For description, see caption of Fig. A.4.9.

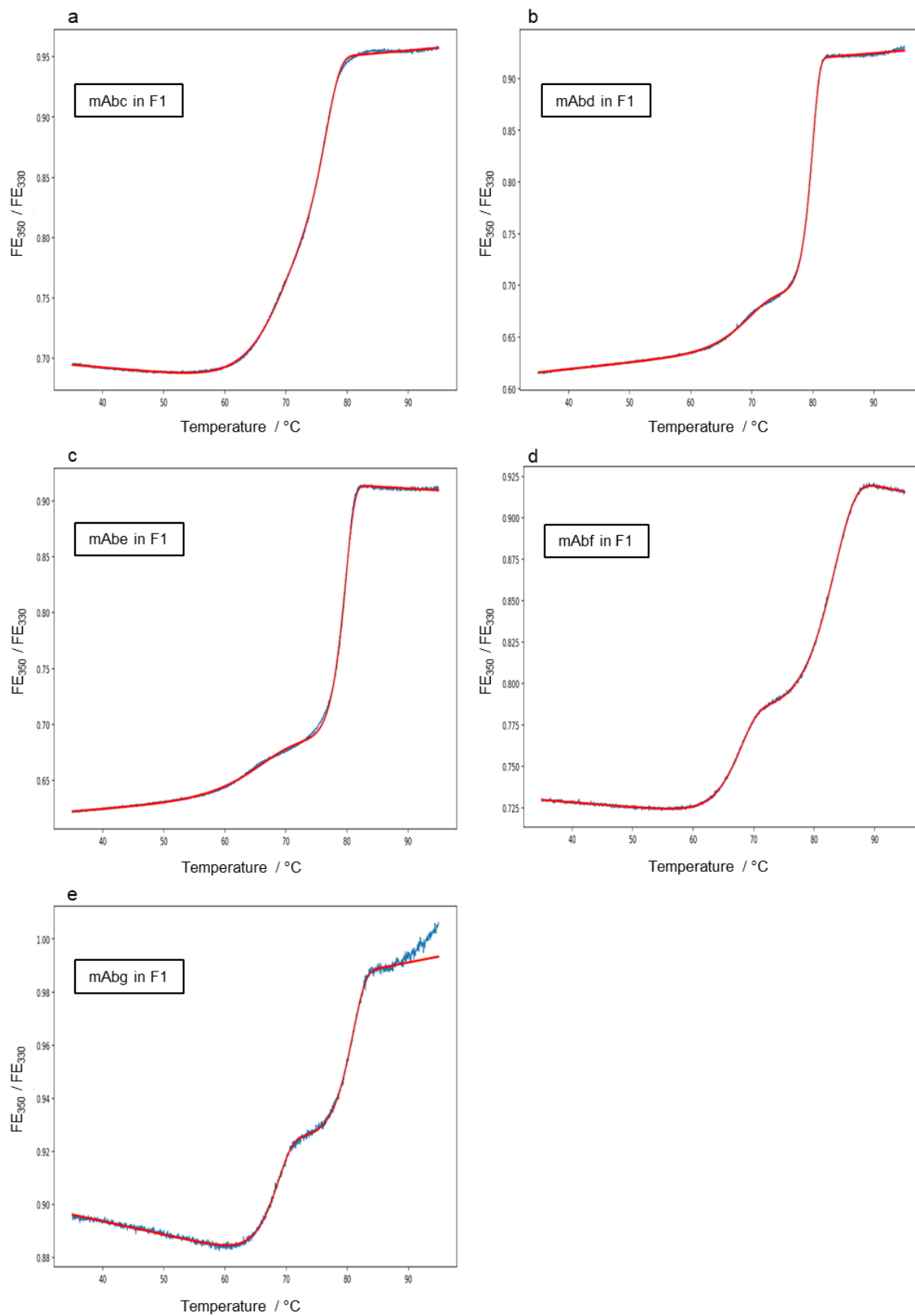


Fig. A.4.12: IF profiles of mAbc to mAbg in F1 recorded by the NES. For description, see caption of Fig. A.4.9.

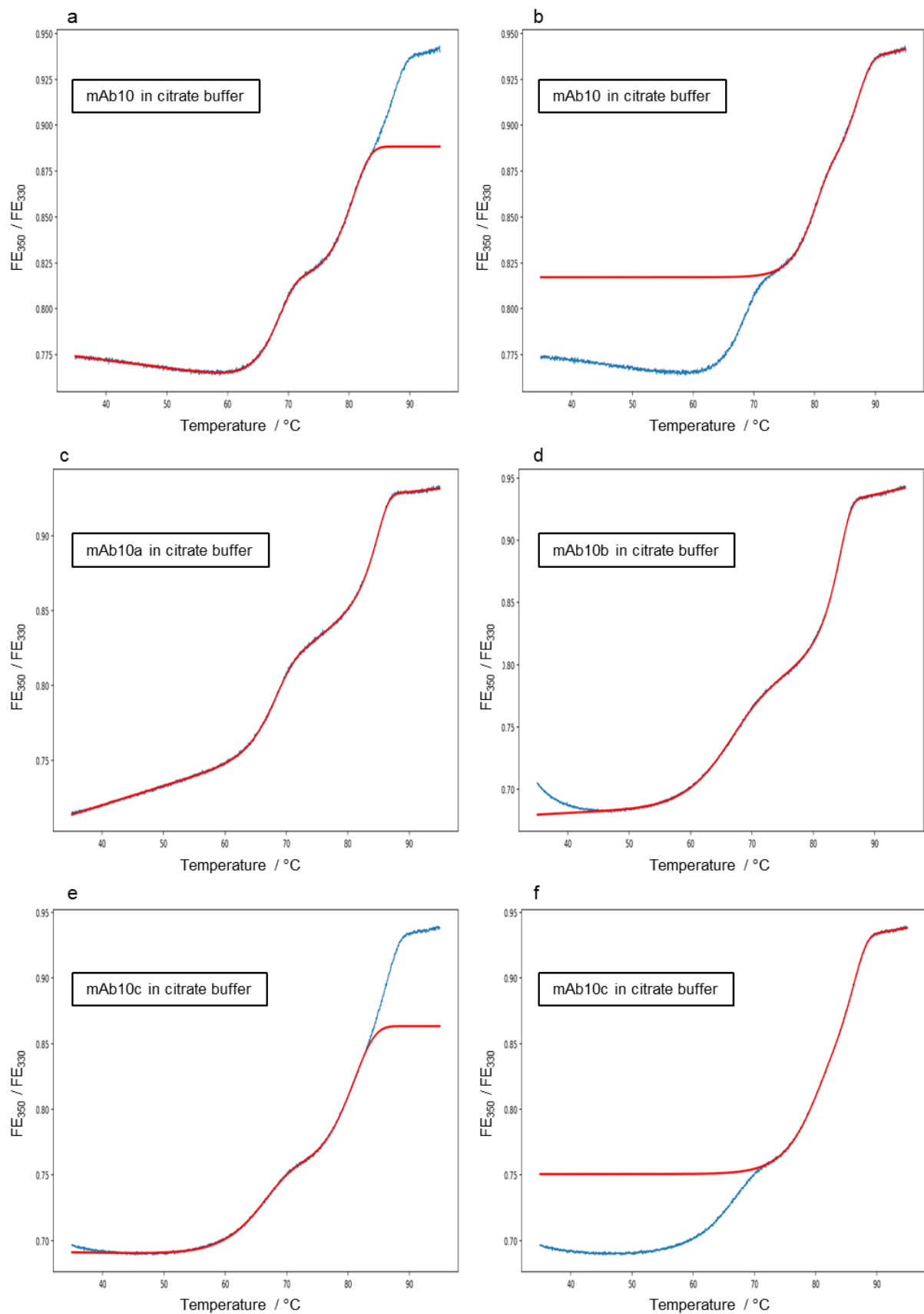


Fig. A.4.13: IF profiles of the mAb10 variants (mAb10 to mAb10c) in F1 recorded by the NES. For description, see caption of Fig. A.4.9. For IF profiles showing four apparent transition, the reversible three-state fit was used two times.

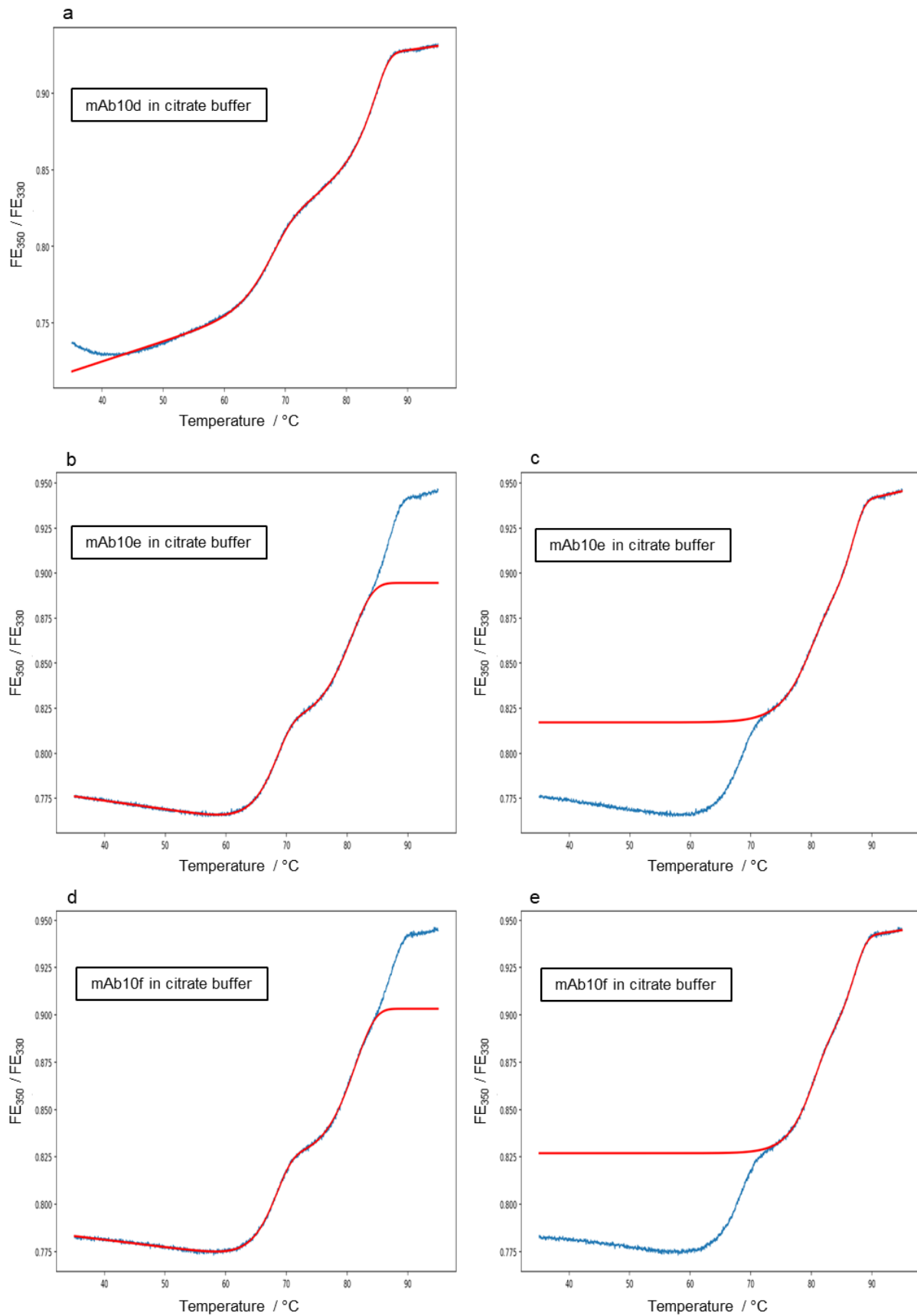


Fig. A.4.14: IF profiles of the mAb10 variants (mAb10d to mAb10f) in F1 recorded by the NES. For description, see caption of Fig. A.4.9. For IF profiles showing four apparent transition, the reversible three-state fit was used two times.

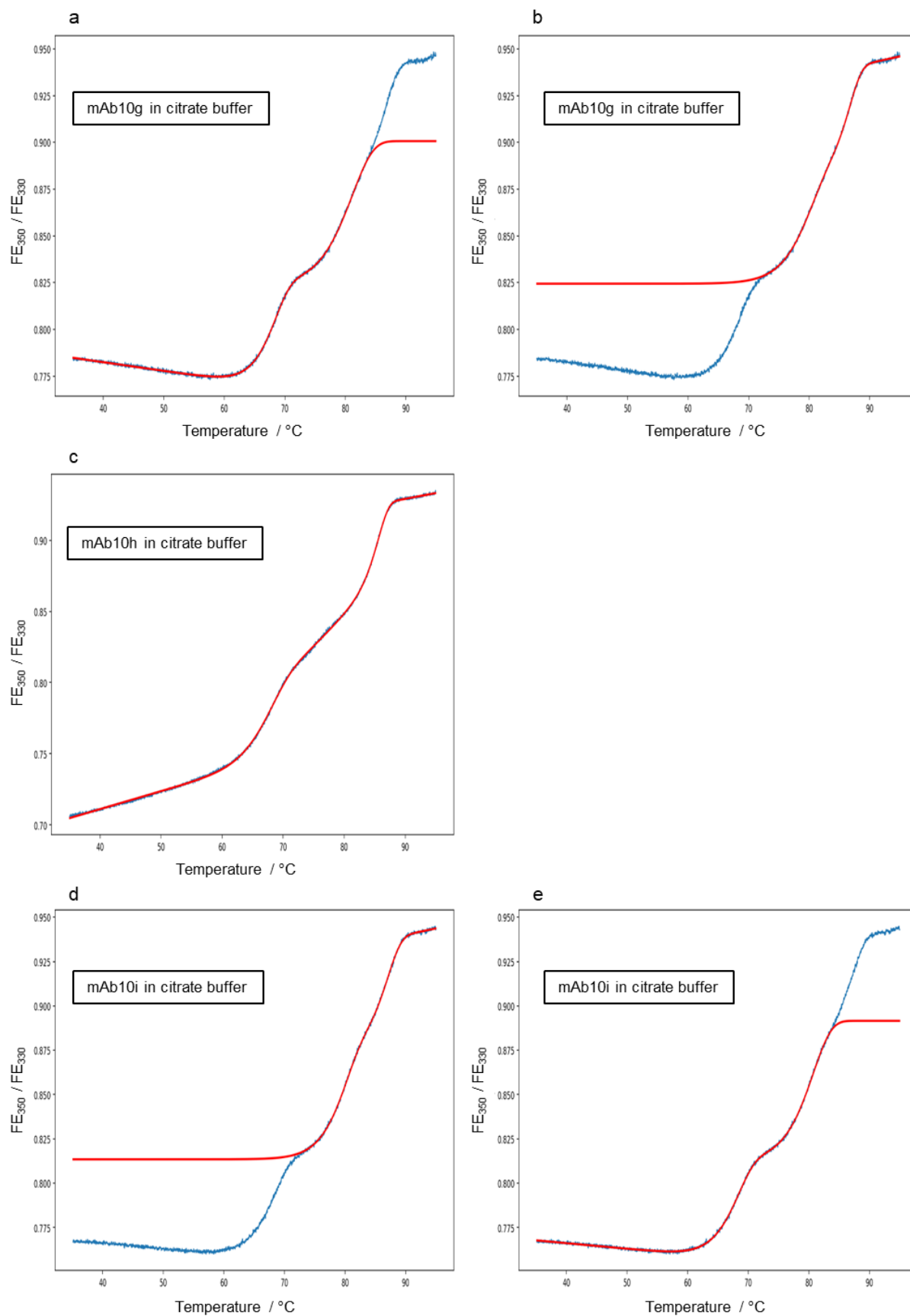


Fig. A.4.15: IF profiles of the mAb10 variants (mAb10g to mAb10i) in F1 recorded by the NES. For description, see caption of Fig. A.4.9. For IF profiles showing four apparent transition, the reversible three-state fit was used two times.

A compilation of all T_m , E_a , ΔH_{vh} , and thermal stability data is shown in Tab. A.4.3.

Tab. A.4.3: Summary of thermodynamics and kinetics. All values of T_m , E_a , ΔH_{vh} , and thermal stability used for analysis in Chapter IV are summarized. All predictive parameters are deduced from IF thermograms as described in Chapter IV and are reported as mean and standard deviation of a duplicate measurement (exception: mAb1 variants in citrate buffer as described in Chapter III). The samples were measured at a mAb concentration of $1 \text{ mg}\cdot\text{ml}^{-1}$ solved in citrate buffer (25 mM sodium citrate, 125 mM NaCl at pH 6.0, abbreviated here as “Cit”), F1 (10 mM histidine at pH 6.0), F2 (10 mM histidine, 150 mM NaCl at pH 6.0), and F3 (10 mM histidine, 220 mM trehalose at pH 6.0). For IF analyses, both the Prometheus instrument and the NES were used at a heating rate of $1 \text{ K}\cdot\text{min}^{-1}$. Thermal stability was investigated by the thermally induced stress studies as described in Chapter IV. Transitions were assigned according to DSC and the IF profiles are clustered in the four introduced categories, abbreviated here as “Cat”.

Sample	Transition	IF (Prometheus)			IF (NES)			IF (Prometheus)			SEC					
		$T_m(1) / ^\circ\text{C}$	$T_m(2) / ^\circ\text{C}$	$T_m(3) / ^\circ\text{C}$	$E_a(1) / \text{kJ}\cdot\text{mol}^{-1}$	$E_a(2) / \text{kJ}\cdot\text{mol}^{-1}$	$E_a(3) / \text{kJ}\cdot\text{mol}^{-1}$	$\Delta H_{vh}(1) / \text{kJ}\cdot\text{mol}^{-1}$	$\Delta H_{vh}(2) / \text{kJ}\cdot\text{mol}^{-1}$	$\Delta H_{vh}(3) / \text{kJ}\cdot\text{mol}^{-1}$	Monomer loss at $40^\circ\text{C} / \%$	Aggregate content increase at $40^\circ\text{C} / \%$	Fragment content increase at $40^\circ\text{C} / \%$	Monomer loss at $25^\circ\text{C} / \%$	Aggregate content increase at $25^\circ\text{C} / \%$	Fragment content increase at $25^\circ\text{C} / \%$
mAb1-Cit (Cat. 2)	(1) = Fab (2) = CH ₃	66.6±0.0	82.5±0.1		325±0.7	473±8.5		544±3.5	638±34		3.3	0.7	2.6			
mAb1-F1 (Cat. 2)	(1) = Fab (2) = CH ₃	66.3±0.1	81.6±0.1		354±2.1	395±29		678±12	736±201							
mAb1-F2 (Cat. 2)	(1) = Fab (2) = CH ₃	64.2±0.1	80.0±0.2		349±2.1	281±13		680±0.0	599±24							
mAb1-F3 (Cat. 2)	(1) = Fab (2) = CH ₃	67.9±0.0	82.8±0.1		348±2.1	353±9.2		683±6.4	775±46							
mAb1a-Cit (Cat. 2)	(1) = Fab (2) = CH ₃	68.1±0.0	82.7±0.1		364±0.0	702±11		715±5.5	504±11		2.0	0.4	1.6			
mAb1a-F1 (Cat. 2)	(1) = Fab (2) = CH ₃	67.5±0.0	81.6±0.1		382±0.0	311±7.1		758±11	554±33							
mAb1a-F2 (Cat. 2)	(1) = Fab (2) = CH ₃	65.6±0.1	80.1±0.2		367±4.2	281±2.1		725±16	553±30							
mAb1a-F3 (Cat. 2)	(1) = Fab (2) = CH ₃	69.1±0.1	82.9±0.1		387±1.4	286±3.5		774±11	819±41							
mAb1b-Cit (Cat. 1)	(1) = CH ₂ (2) = Fab	70.2±0.1	79.9±0.1		315±6.4	375±2.1		505±3.3	686±46		1.3	-0.3	1.5			
mAb1b-F1 (Cat. 1)	(1) = CH ₂ (2) = Fab	68.8±0.1	79.3±0.1		341±0.7	367±2.1		564±6.4	806±1.4							
mAb1b-F2 (Cat. 1)	(1) = CH ₂ (2) = Fab	66.4±0.0	79.0±0.1		344±0.7	403±1.4		589±17	684±23							
mAb1b-F3 (Cat. 1)	(1) = CH ₂ (2) = Fab	70.3±0.1	80.6±0.2		346±3.5	384±7.8		585±8.5	848±26							
mAb1c-Cit (Cat. 2)	(1) = Fab (2) = CH ₃	69.0±0.1	82.4±0.2		275±1.4	585±13		534±2.3	608±38		6.6	4.9	1.7			
mAb1c-F1 (Cat. 2)	(1) = Fab (2) = CH ₃	68.2±0.1	81.5±0.1		303±1.4	439±19		579±0.7	783±53							
mAb1c-F2 (Cat. 2)	(1) = Fab (2) = CH ₃	66.2±0.0	80.3±0.2		244±6.4	489±83		488±9.9	1429±16							
mAb1c-F3 (Cat. 2)	(1) = Fab (2) = CH ₃	69.6±0.0	82.7±0.3		300±2.1	467±190		599±0.7	756±37							
mAb1d-Cit (Cat. 2)	(1) = Fab (2) = CH ₃	68.4±0.1	82.3±0.1		246±0.0	577±9.2		571±4.8	760±24		4.4	2.7	1.8			
mAb1d-F1 (Cat. 2)	(1) = Fab (2) = CH ₃	67.8±0.1	81.2±0.2		272±2.8	392±21		518±4.2	738±2.8							
mAb1d-F2 (Cat. 2)	(1) = Fab (2) = CH ₃	66.0±0.1	80.0±0.1		211±0.0	1444±79		421±17	1230±30							
mAb1d-F3 (Cat. 2)	(1) = Fab (2) = CH ₃	69.2±0.1	82.4±0.1		281±11	390±1.4		528±1.4	866±66							

mAb1e-Cit (Cat. 2)	(1) = Fab (2) = CH ₃	68.9±0.1	82.4±0.1	288±3.5	552±20	615±3.9	617±31	2.8	1.2	1.6				
mAb1e-F1 (Cat. 2)	(1) = Fab (2) = CH ₃	68.4±0.0	81.5±0.1	306±0.0	278±6.4	623±9.9	627±23							
mAb1e-F2 (Cat. 2)	(1) = Fab (2) = CH ₃	66.4±0.1	80.4±0.0	280±1.4	1700±415	502±7.1	1158±110							
mAb1e-F3 (Cat. 2)	(1) = Fab (2) = CH ₃	70.0±0.1	83.0±0.0	316±3.5	277±5.7	643±6.4	865±21							
mAb2-Cit (Cat. 1)	(1) = CH ₂ (2) = Fab	68.9±0.1	80.6±0.1	352±0.7	539±5.7	457±4.2	976±14							
mAb2-F1 (Cat. 1)	(1) = CH ₂ (2) = Fab	68.7±0.1	81.1±0.0	393±4.2	491±4.2	506±8.5	868±20							
mAb2-F2 (Cat. 1)	(1) = CH ₂ (2) = Fab	66.2±0.0	79.6±0.2	378±2.8	521±3.5	516±6.4	795±2.1							
mAb2-F3 (Cat. 1)	(1) = CH ₂ (2) = Fab	70.3±0.0	82.6±0.1	409±0.0	472±2.8	531±1.4	828±14							
mAb3-Cit (Cat. 2)	(1) = Fab (2) = CH ₃	69.1±0.0	81.9±0.2	356±0.0	299±2.1	776±23	400±169							
mAb3-F1 (Cat. 2)	(1) = Fab (2) = CH ₃	70.6±0.1	81.5±0.0			639±15	791±41							
mAb3-F2 (Cat. 2)	(1) = Fab (2) = CH ₃	67.8±0.0	80.3±0.6	337±2.8	265±7.1	615±12	832±5.7							
mAb3-F3 (Cat. 2)	(1) = Fab (2) = CH ₃	71.8±0.1	83.1±0.0			669±11	537±134							
mAb4-Cit (Cat. 1)	(1) = CH ₂ (2) = Fab	70.6±0.1	76.7±0.1	326±18	534±27	458±9.9	606±60							
mAb4-F1 (Cat. 1)	(1) = CH ₂ (2) = Fab	69.8±0.0	77.9±0.1	381±9.2	458±4.2	470±1.4	922±35	1.2	0.2	0.9	0.4	0.1	0.3	
mAb4-F2 (Cat. 1)	(1) = CH ₂ (2) = Fab	67.2±0.1	77.2±0.0	348±7.8	384±0.7	483±22	615±44	1.4	0.4	1.0	0.5	0.3	0.3	
mAb4-F3 (Cat. 1)	(1) = CH ₂ (2) = Fab	71.4±0.1	79.1±0.0	390±0.7	456±2.1	471±7.1	967±3.5	1.3	0.6	1.0	0.3	0.05	0.2	
mAb5-Cit (Cat. 1)	(1) = CH ₂ (2) = Fab	51.1±0.1	77.6±0.0	346±0.7	435±0.7	524±7.8	688±1.4							
mAb5-F1 (Cat. 1)	(1) = CH ₂ (2) = Fab	48.9±0.0	80.1±0.0	321±11	439±6.4	497±11	650±40	9.9	9.4	0.4	0.02	0.02	0.02	
mAb5-F2 (Cat. 1)	(1) = CH ₂ (2) = Fab	50.5±0.1	77.6±0.1	346±0.7	449±1.4	531±0.0	650±3.5	3.8	3.4	0.4	0.3	0.3	0.2	
mAb5-F3 (Cat. 1)	(1) = CH ₂ (2) = Fab	50.9±0.1	81.3±0.0	341±3.5	438±5.7	504±1.4	667±0.7	3.6	3.2	0.4	0.3	0.2	0.1	
mAb6-Cit (Cat. 4)	(1) = CH ₂ (2) = Fab (3) = CH ₃	66.8±0.1	72.9±0.0	81.8±0.0										
mAb6-F1 (Cat. 4)	(1) = CH ₂ (2) = Fab (3) = CH ₃	67.5±0.1	73.8±0.0	81.3±0.1										
mAb6-F2 (Cat. 4)	(1) = CH ₂ (2) = Fab (3) = CH ₃	65.0±0.2	71.4±0.1	80.1±0.0										
mAb6-F3 (Cat. 4)	(1) = CH ₂ (2) = Fab (3) = CH ₃	69.0±0.1	75.1±0.0	82.8±0.0										
mAb7-Cit (Cat. 2)	(1) = Fab (2) = CH ₃	69.1±0.1	82.7±0.1											
mAb7-F1 (Cat. 2)	(1) = Fab (2) = CH ₃	73.2±0.0	82.8±0.1											
mAb7-F2 (Cat. 2)	(1) = Fab (2) = CH ₃	66.3±0.0	76.8±0.0											

mAb7-F3 (Cat. 2)	(1) = Fab (2) = CH ₃	74.5±0.1	85.1±0.6										
mAb8-Cit (Cat. 4)	(1) = CH ₂ (2) = Fab (3) = CH ₃	68.2±0.1	74.3±0.1	83.1±0.3									
mAb8-F1 (Cat. 4)	(1) = CH ₂ (2) = Fab (3) = CH ₃	68.9±0.1	76.0±0.0	82.6±0.1									
mAb8-F2 (Cat. 4)	(1) = CH ₂ (2) = Fab (3) = CH ₃	65.8±0.1	72.7±0.0	81.1±0.4									
mAb8-F3 (Cat. 4)	(1) = CH ₂ (2) = Fab (3) = CH ₃	70.3±0.1	77.2±0.1	83.6±0.0									
mAb9-Cit (Cat. 4)	(1) = Fab (2) = CH ₃	67.3±0.1	80.8±1.5										
mAb9-F1 (Cat. 4)	(1) = Fab (2) = CH ₃	67.8±0.1	81.8±0.1										
mAb9-F2 (Cat. 4)	(1) = Fab (2) = CH ₃	65.6±0.1	80.3±0.2										
mAb9-F3 (Cat. 4)	(1) = Fab (2) = CH ₃	69.1±0.1	83.0±0.1										
mAb9a-Cit (Cat. 2)	(1) = Fab (2) = CH ₃	68.6±0.0	81.3±0.1		298±0.0	344±29	355±6.4	781±47					
mAb9a-F1 (Cat. 4)	(1) = Fab (2) = CH ₃	66.4±0.0	81.5±0.0										
mAb9a-F2 (Cat. 4)	(1) = Fab (2) = CH ₃	63.3±0.0	79.9±0.1										
mAb9a-F3 (Cat. 4)	(1) = Fab (2) = CH ₃	67.5±0.0	82.5±0.0										
mAb9b-Cit (Cat. 2)	(1) = Fab (2) = CH ₃	70.9±0.0	81.4±0.3		270±0.0	566±27	568±1.4	918±84					
mAb9b-F1 (Cat. 2)	(1) = Fab (2) = CH ₃	71.6±0.3	81.9±0.0		246±2.8	379±0.0	397±1.4	1091±55					
mAb9b-F2 (Cat. 2) with shoulder in front of (1)	(1) = Fab (2) = CH ₃	69.8±0.0	80.6±0.1										
mAb9b-F3 (Cat. 2)	(1) = Fab (2) = CH ₃	72.7±0.2	82.9±0.3		260±9.9	301±51	420±7.8	1098±6.4					
mAb10-Cit (Cat. 3)	(1) = CH ₂ (2) = CH ₃ (3) = Fab	69.6±0.0	81.6±0.0	88.2±0.1	361±2.8	389±27	472±33	545±4.9	576±20	882±91	4.4	1.3	3.4
mAb10a- Cit (Cat. 1)	(1) = CH ₂ (2) = Fab	69.6±0.1	86.1±0.1		323±0.7	602±1.4	468±11	1023±11		6.8	4.0	3.2	
mAb10b- Cit (Cat. 1)	(1) = CH ₂ (2) = Fab	69.7±0.1	85.7±0.0		175±0.7	585±13	205±1.4	826±6.4		6.3	3.5	2.7	
mAb10c-Cit (Cat. 3)	(1) = CH ₂ (2) = CH ₃ (3) = Fab	68.7±0.1	80.4±0.6	87.2±0.0	228±4.9	298±16	497±3.5	317±7.8	540±43	685±1.4	10	5.8	4.4
mAb10d- Cit (Cat. 1)	(1) = CH ₂ (2) = Fab	69.3±0.0	86.3±0.1		271±2.8	495±16	508±13	848±11		7.1	1.8	4.0	
mAb10e- Cit (Cat. 3)	(1) = CH ₂ (2) = CH ₃ (3) = Fab	69.7±0.1	81.8±0.0	87.8±0.0	363±0.7	315±17	547±7.1	527±17	521±40	891±50	4.2	1.4	2.8
mAb10f-Cit (Cat. 3)	(1) = CH ₂ (2) = CH ₃ (3) = Fab	69.5±0.0	82.0±0.1	88.3±0.1	357±17	373±38	485±14	561±24	564±48	925±177	4.6	1.0	3.2

mAb10g-Cit (Cat. 3)	(1) = CH ₂ (2) = CH ₃ (3) = Fab	69.7±0.1	81.8±0.5	87.9±0.1	382±3.5	318±21	515±24	556±8.5	512±57	941±50	3.2	1.2	2.7			
mAb10h-Cit (Cat. 1)	(1) = CH ₂ (2) = Fab	69.5±0.1	86.5±0.0		271±0.0	669±43		352±2.8	1012±0.0		5.7	3.1	2.6			
mAb10i-Cit (Cat. 3)	(1) = CH ₂ (2) = CH ₃ (3) = Fab	69.7±0.0	81.9±0.3	88.2±0.1	346±0.0	366±17	474±2.8	499±4.9	575±29	872±35	6.4	1.2	5.2			
mAba-Cit (Cat. 1)	(1) = CH ₂ (2) = Fab	70.2±0.1	81.2±0.1		300±6.4	495±2.1		389±59	780±27							
mAba-F1 (Cat. 1)	(1) = CH ₂ (2) = Fab	69.0±0.0	82.0±0.0		329±0.7	415±1.4		424±3.5	726±0.7		4.0	0.9	3.0	0.6	0.3	0.3
mAba-F2 (Cat. 1)	(1) = CH ₂ (2) = Fab	66.8±0.1	79.4±0.0		308±0.0	452±2.8		398±6.4	736±4.2		4.5	1.7	2.7	1.0	0.7	0.3
mAba-F3 (Cat. 1)	(1) = CH ₂ (2) = Fab	70.5±0.0	83.1±0.1		339±5.7	428±8.5		426±4.9	737±4.9		3.8	0.6	3.2	0.7	0.3	0.4
mAbb-Cit (Cat. 3)	(1) = CH ₂ (2) = CH ₃ (3) = Fab	69.7±0.1	83.0±0.0	88.2±0.0	345±6.4	253±44	547±9.2	428±4.9	466±52	818±3.5						
mAbb-F1 (Cat. 3)	(1) = CH ₂ (2) = CH ₃ (3) = Fab	68.8±0.0	82.0±0.1	89.6±0.0	382±5.7	313±43	523±4.9	542±17	441±8.1	748±9.9	5.0	1.2	3.8	0.8	0.4	0.4
mAbb-F2 (Cat. 3)	(1) = CH ₂ (2) = CH ₃ (3) = Fab	66.5±0.1	80.1±0.1	87.8±0.0	359±1.4	299±34	526±3.5	514±7.8	427±31	823±15	5.2	1.9	3.3	1.0	0.7	0.4
mAbb-F3 (Cat. 3)	(1) = CH ₂ (2) = CH ₃ (3) = Fab	70.4±0.0	83.3±0.3	90.9±0.0	389±4.9	312±37	535±2.8	537±16	428±38	860±7.8	4.6	0.8	3.8	0.7	0.3	0.4
mAbc-Cit (Cat. 1)	(1) = CH ₂ (2) = Fab	70.6±0.1	77.1±0.0		269±3.5	589±2.1		368±7.1	954±5.7							
mAbc-F1 (Cat. 1)	(1) = CH ₂ (2) = Fab	69.5±0.3	76.8±0.0		247±0.7	442±3.5		366±0.0	727±18		8.3	3.0	4.6	1.7	1.0	0.7
mAbc-F2 (Cat. 1)	(1) = CH ₂ (2) = Fab	67.6±0.3	75.9±0.1		256±2.1	310±2.1		329±1.4	855±0.7		7.4	3.5	3.8	2.1	0.9	1.1
mAbc-F3 (Cat. 1)	(1) = CH ₂ (2) = Fab	71.5±0.4	78.3±0.1		258±0.0	444±1.4		371±2.8	768±2.1		7.6	3.1	4.5	1.6	0.9	0.8
mAbd-Cit (Cat. 1)	(1) = CH ₂ (2) = Fab	69.8±0.1	80.9±0.0		251±3.5	965±2.8		330±3.5	1459±4.2							
mAbd-F1 (Cat. 1)	(1) = CH ₂ (2) = Fab	68.9±0.1	80.7±0.1		264±4.2	906±11		366±6.4	1304±11		6.3	2.0	4.3	1.5	1.1	0.4
mAbd-F2 (Cat. 1)	(1) = CH ₂ (2) = Fab	67.0±0.2	79.8±0.0		218±5.7	959±7.8		302±1.4	1357±9.2		5.9	2.0	3.9	1.5	1.0	0.5
mAbd-F3 (Cat. 1)	(1) = CH ₂ (2) = Fab	70.2±0.2	81.6±0.0		293±8.5	899±0.0		401±4.2	1310±1.4		5.7	1.4	4.2	0.9	0.5	0.4
mAbe-Cit (Cat. 1)	(1) = CH ₂ (2) = Fab															
mAbe-F1 (Cat. 1)	(1) = CH ₂ (2) = Fab	64.4±0.2	80.7±0.0		185±0.7	703±6.4		234±2.1	1027±0.7		8.7	3.9	4.8	2.5	1.8	0.7
mAbe-F2 (Cat. 1)	(1) = CH ₂ (2) = Fab	62.6±0.2	79.5±0.0		206±23	736±27		218±2.8	1155±7.8		7.3	3.7	3.6	1.9	1.8	0.1
mAbe-F3 (Cat. 1)	(1) = CH ₂ (2) = Fab	66.1±0.1	81.4±0.0		225±4.2	701±5.7		266±12	1037±25		7.1	2.8	4.3	1.3	1.3	0.1
mAbf-Cit (Cat. 1)	(1) = CH ₂ (2) = Fab	69.6±0.1	82.2±0.1		287±4.2	466±0.7		412±0.7	756±7.8							
mAbf-F1 (Cat. 1)	(1) = CH ₂ (2) = Fab	68.9±0.0	84.2±0.1		347±2.1	319±0.7		539±23	476±2.1		4.5	1.5	3.0	0.8	0.5	0.3
mAbf-F2 (Cat. 1)	(1) = CH ₂ (2) = Fab	66.5±0.1	84.6±0.1		329±1.4	310±2.1		514±26	417±1.4		4.9	1.9	2.7	1.1	0.7	0.3
mAbf-F3 (Cat. 1)	(1) = CH ₂ (2) = Fab	70.6±0.0	85.3±0.1		359±7.1	329±2.1		556±13	475±26		4.0	1.2	2.7	0.8	0.3	0.3

mAbg-Cit (Cat. 1)	(1) = CH ₂ (2) = Fab	69.8±0.2	82.4±0.1	393±4.9	636±4.2	541±11	1037±42							
mAbg-F1 (Cat. 1)	(1) = CH ₂ (2) = Fab	69.5±0.1	81.8±0.1	397±2.8	499±1.4	568±2.8	766±11	7.3	1.6	5.7	1.1	0.4	0.7	
mAbg-F2 (Cat. 1)	(1) = CH ₂ (2) = Fab	66.9±0.1	81.4±0.1	429±11	968±2.8	667±9.2	1609±53	6.8	2.3	4.5	1.3	0.8	0.5	
mAbg-F3 (Cat. 1)	(1) = CH ₂ (2) = Fab	70.9±0.0	83.1±0.1	418±5.7	477±2.8	572±12	833±71	6.8	1.2	5.6	0.9	0.3	0.6	
mAbh-Cit (Cat. 2)	(1) = Fab (2) = CH ₃	64.3±0.1	81.4±0.1	444±29.7	921±163	662±2.1	811±12							
mAbh-F1 (Cat. 2)	(1) = Fab (2) = CH ₃	66.3±0.0	81.1±0.1	498±0.7	465±20	738±1.4	423±37							
mAbh-F2 (Cat. 2)	(1) = Fab (2) = CH ₃	64.8±0.1	79.9±0.1	447±2.8	663±47	684±0.7	492±11							
mAbh-F3 (Cat. 2)	(1) = Fab (2) = CH ₃	67.6±0.1	82.3±0.0	497±1.4	457±3.5	756±2.1	450±3.5							

Predicting thermal stability via thermodynamic and kinetic parameters

To investigate if a correlation between predictive parameters and thermal stability exists, a linear regression and an analysis of variance (ANOVA) test were applied. The ANOVA test gives two parameters describing the validity and significance of the slope of the linear function. A higher F-value indicates a higher evidence for the slope being different from zero compared to a lower F-value. The significance of the linear slope being different from zero can be evaluated by expressing a probability of the F-value ($\text{Prob}>F$). For this purpose, a significance level of 95 % was chosen. By doing so, the parameter $\text{Prob}>F$ has to be smaller than 0.05 for a slope, which is significantly different from zero. A correlation between the predictive parameter and thermal stability was assigned if the linear regression shows a significantly negative slope. The parameters deduced from the linear regressions and ANOVA between mAb_a to mAb_g and mAb₄ in F1, F2, F3 and thermal stability at 25 °C are summarized in Tab. A.4.4.

Tab. A.4.4: Parameters derived from the linear regressions for mAb_a to mAb_g and mAb₄ in F1, F2, and F3 at 25 °C. Linear fits were applied to the plots shown in Fig. 4.5 (Chapter IV). An ANOVA test was performed to investigate if the slope of the linear regression is significantly different from zero. If a significantly negative slope is determined, a correlation between predictive parameter and thermal stability was interpreted. Linear regressions showing a correlation are highlighted in bold letters and numbers.

Linear fit	Slope and standard error	R-square	F-value	Prob>F	Correlation (linear slope significantly <, =, or > 0)
E_a(CH₂) vs. monomer	-100 ± 18	0.58	30	1.6·10⁻⁵	yes (<0)
- for F1 only	-99 ± 21	0.79	22	3.3·10⁻³	yes (<0)
- for F2 only	-94 ± 48	0.39	3.8	0.10	no (=0)
- for F3 only	-130 ± 46	0.57	8.0	3.0·10⁻²	yes (<0)
ΔH_{vh}(CH₂) vs. monomer	-136 ± 36	0.40	15	9.0·10⁻⁴	yes (<0)
- for F1 only	-131 ± 42	0.62	10	2.0·10⁻²	yes (<0)
- for F2 only	-169 ± 95	0.34	3.1	0.13	no (=0)
- for F3 only	-148 ± 88	0.32	2.8	0.14	no (=0)
T_m(CH₂) vs. monomer	-2.3 ± 0.74	0.30	9.6	5.2·10⁻³	yes (<0)
- for F1 only	-1.9 ± 0.68	0.56	7.6	3.3·10⁻²	yes (<0)
- for F2 only	-1.0 ± 1.2	0.10	0.68	0.44	no (=0)
- for F3 only	-1.4 ± 1.6	0.11	0.77	0.41	no (=0)
E _a (Fab) vs. monomer	126 ± 77	0.11	2.7	0.12	no (=0)

$\Delta H_{vh}(\text{Fab})$ vs. monomer	172 ± 109	0.10	2.5	0.13	no (=0)
$T_m(\text{Fab})$ vs. monomer	-2.5 ± 1.4	0.12	3.1	$9.3 \cdot 10^{-2}$	no (=0)
$E_a(\text{CH}_2)$ vs. aggregate	-126 ± 17	0.70	52	$3.1 \cdot 10^{-7}$	yes (<0)
- for F1 only	-129 ± 20	0.87	42	$6.4 \cdot 10^{-4}$	yes (<0)
- for F2 only	-117 ± 52	0.46	5.2	$6.3 \cdot 10^{-2}$	no (=0)
- for F3 only	-152 ± 29	0.82	28	$1.9 \cdot 10^{-3}$	yes (<0)
$\Delta H_{vh}(\text{CH}_2)$ vs. aggregate	-184 ± 35	0.56	28	$2.5 \cdot 10^{-5}$	yes (<0)
- for F1 only	-176 ± 44	0.73	16	$7.1 \cdot 10^{-3}$	yes (<0)
- for F2 only	-221 ± 98	0.46	5.1	$6.6 \cdot 10^{-2}$	no (=0)
- for F3 only	-213 ± 58	0.69	13	$1.0 \cdot 10^{-2}$	yes (<0)
$T_m(\text{CH}_2)$ vs. aggregate	-3.5 ± 0.67	0.56	28	$2.6 \cdot 10^{-5}$	yes (<0)
- for F1 only	-2.5 ± 0.75	0.65	11	$1.6 \cdot 10^{-2}$	yes (<0)
- for F2 only	-3.0 ± 0.80	0.70	14	$9.8 \cdot 10^{-3}$	yes (<0)
- for F3 only	-3.1 ± 1.1	0.55	7.3	$3.6 \cdot 10^{-2}$	yes (<0)
$E_a(\text{Fab})$ vs. aggregate	204 ± 83	0.22	6.0	$2.2 \cdot 10^{-2}$	yes (>0, inverse correlation)
$\Delta H_{vh}(\text{Fab})$ vs. aggregate	241 ± 122	0.15	3.9	$6.0 \cdot 10^{-2}$	no (=0)
$T_m(\text{Fab})$ vs. aggregate	-2.3 ± 1.7	0.078	1.9	0.19	no (=0)
$E_a(\text{CH}_2)$ vs. fragment	-34 ± 63	$1.3 \cdot 10^{-2}$	0.29	0.59	no (=0)
$\Delta H_{vh}(\text{CH}_2)$ vs. fragment	-10 ± 104	$4.4 \cdot 10^{-4}$	$9.6 \cdot 10^{-3}$	0.92	no (=0)
$T_m(\text{CH}_2)$ vs. fragment	1.9 ± 2.0	$4.2 \cdot 10^{-2}$	0.97	0.34	no (=0)
$E_a(\text{Fab})$ vs. fragment	-93 ± 186	$1.1 \cdot 10^{-2}$	0.25	0.62	no (=0)
$\Delta H_{vh}(\text{Fab})$ vs. fragment	24 ± 263	$3.7 \cdot 10^{-4}$	$8.2 \cdot 10^{-3}$	0.93	no (=0)
$T_m(\text{Fab})$ vs. fragment	-4.6 ± 3.3	$7.9 \cdot 10^{-2}$	1.9	0.18	no (=0)

For thermal stability at 40 °C, the parameters from the linear regression and ANOVA for mAb_a to mAb_g and mAb₄ in formulation F1, F2, and F3 are depicted in Tab. A.4.5.

Tab. A.4.5: Parameters derived from the linear regressions for mAb_a to mAb_g and mAb₄ in F1, F2, and F3 at 40 °C. Linear fits were applied to the plots shown in Fig. 4.6 (Chapter IV). For description, see caption of Tab. A.4.4.

Linear fit	Slope and standard error	R-square	F-value	Prob>F	Correlation (linear slope significantly <, =, or > 0)
E_a(CH₂) vs. monomer	-18 ± 6.1	0.28	8.5	7.9·10⁻³	yes (<0)
- for F1 only	-20 ± 9.4	0.43	4.4	8.0·10 ⁻²	no (=0)
- for F2 only	-13 ± 15	0.12	0.82	0.40	no (=0)
- for F3 only	-18 ± 11	0.31	2.7	0.15	no (=0)
ΔH _{vh} (CH ₂) vs. monomer	-21 ± 11	0.15	3.7	6.6·10 ⁻²	no (=0)
T _m (CH ₂) vs. monomer	-0.35 ± 0.21	0.11	2.6	0.12	no (=0)
E _a (Fab) vs. monomer	35 ± 20	0.13	3.2	8.6·10 ⁻²	no (=0)
ΔH _{vh} (Fab) vs. monomer	42 ± 28	9.0·10 ⁻²	2.2	0.15	no (=0)
T _m (Fab) vs. monomer	-0.18 ± 0.39	9.3·10 ⁻³	0.21	0.65	no (=0)
E_a(CH₂) vs. aggregate	-49 ± 9.5	0.55	27	3.3·10⁻⁵	yes (<0)
- for F1 only	-57 ± 13	0.75	18	5.6·10⁻³	yes (<0)
- for F2 only	-38 ± 25	0.27	2.2	0.19	no (=0)
- for F3 only	-56 ± 16	0.68	12	1.2·10⁻²	yes (<0)
ΔH _{vh} (CH ₂) vs. aggregate	-66 ± 18	0.37	13	1.5·10⁻³	yes (<0)
- for F1 only	-71 ± 27	0.52	6.6	4.2·10⁻²	yes (<0)
- for F2 only	-71 ± 49	0.26	2.1	0.20	no (=0)
- for F3 only	-68 ± 32	0.43	4.6	7.6·10 ⁻²	no (=0)
T _m (CH ₂) vs. aggregate	-1.2 ± 0.36	0.35	12	2.4·10⁻³	yes (<0)
- for F1 only	-1.1 ± 0.41	0.52	6.6	4.2·10⁻²	yes (<0)
- for F2 only	-0.78 ± 0.53	0.26	2.2	0.19	no (=0)
- for F3 only	-0.76 ± 0.62	0.20	1.5	0.26	no (=0)
E _a (Fab) vs. aggregate	53 ± 40	7.5·10 ⁻²	1.8	0.20	no (=0)
ΔH _{vh} (Fab) vs. aggregate	72 ± 56	6.9·10 ⁻²	1.6	0.22	no (=0)
T _m (Fab) vs. aggregate	-1.1 ± 0.73	0.10	2.3	0.14	no (=0)

E _a (CH ₂) vs. fragment	-13 ± 12	5.1·10 ⁻²	1.2	0.29	no (=0)
ΔH _{vh} (CH ₂) vs. fragment	-9.8 ± 19	1.0·10 ⁻²	0.25	0.62	no (=0)
T _m (CH ₂) vs. fragment	-8.9·10 ⁻² ±0.38	2.6·10 ⁻³	5.6·10 ⁻²	0.81	no (=0)
E _a (Fab) vs. fragment	64 ± 32	0.16	4.0	5.7·10 ⁻²	no (=0)
ΔH _{vh} (Fab) vs. fragment	72 ± 47	0.10	2.4	0.14	no (=0)
T _m (Fab) vs. fragment	0.39 ± 0.64	1.6·10 ⁻²	0.37	0.55	no (=0)

The parameters from linear regression and ANOVA for the ten mAb10 variants formulated in citrate buffer are shown in Tab. A.4.6.

Tab. A.4.6: Parameters derived from the linear regressions of the mAb10 variants in citrate buffer at 40 °C. Linear fits were applied to the plots shown in Fig. 4.7 (Chapter IV). For description, see caption of Tab. A.4.4.

Linear fit	Slope and standard error	R-square	F-value	Prob>F	Correlation (linear slope significantly <, =, or > 0)
E_a(CH₂) vs. monomer	-24 ± 9.0	0.46	7.0	3.0·10⁻²	yes (<0)
ΔH _{vh} (CH ₂) vs. monomer	-35 ± 18	0.33	3.9	8.4·10 ⁻²	no (=0)
T_m(CH₂) vs. monomer	-0.13 ± 3.4·10⁻²	0.66	16	4.3·10⁻³	yes (<0)
E _a (Fab) vs. monomer	-0.19 ± 12	3.4·10 ⁻⁵	2.7·10 ⁻⁴	0.99	no (=0)
ΔH _{vh} (Fab) vs. monomer	-30 ± 14	0.37	4.7	6.1·10 ⁻²	no (=0)
T _m (Fab) vs. monomer	-0.21 ± 0.16	0.18	1.8	0.22	no (=0)
E_a(CH₂) vs. aggregate	-31 ± 10	0.53	9.0	1.7·10⁻²	yes (<0)
ΔH_{vh}(CH₂) vs. aggregate	-57 ± 17	0.58	11	1.0·10⁻²	yes (<0)
T_m(CH₂) vs. aggregate	-0.14 ± 4.8·10⁻²	0.51	8.2	2.1·10⁻²	yes (<0)
E _a (Fab) vs. aggregate	16 ± 13	0.16	1.5	0.26	no (=0)
ΔH _{vh} (Fab) vs. aggregate	-23 ± 20	0.14	1.3	0.28	no (=0)
T _m (Fab) vs. aggregate	-0.37 ± 0.17	0.36	4.6	6.5·10 ⁻²	no (=0)
E _a (CH ₂) vs. fragment	-0.16 ± 28	4.2·10 ⁻⁶	3.3·10 ⁻⁵	1.0	no (=0)

$\Delta H_{vh}(\text{CH}_2)$ vs. fragment	15 ± 50	$1.2 \cdot 10^{-2}$	$9.6 \cdot 10^{-2}$	0.76	no (=0)
$T_m(\text{CH}_2)$ vs. fragment	-0.13 ± 0.12	0.13	1.2	0.30	no (=0)
$E_a(\text{Fab})$ vs. fragment	-48 ± 21	0.39	5.0	$5.5 \cdot 10^{-2}$	no (=0)
$\Delta H_{vh}(\text{Fab})$ vs. fragment	-58 ± 34	0.27	2.9	0.13	no (=0)
$T_m(\text{Fab})$ vs. fragment	0.32 ± 0.39	$8.0 \cdot 10^{-2}$	0.70	0.43	no (=0)

Determination of activation energies at fast heating rates

To compare the different outcomes of E_a values determined at a slower or faster heating rate, values of E_a for the CH_2 -domain and the Fab of mAba to mAbg, mAb4 and mAb5 are shown in Fig. A.4.16.

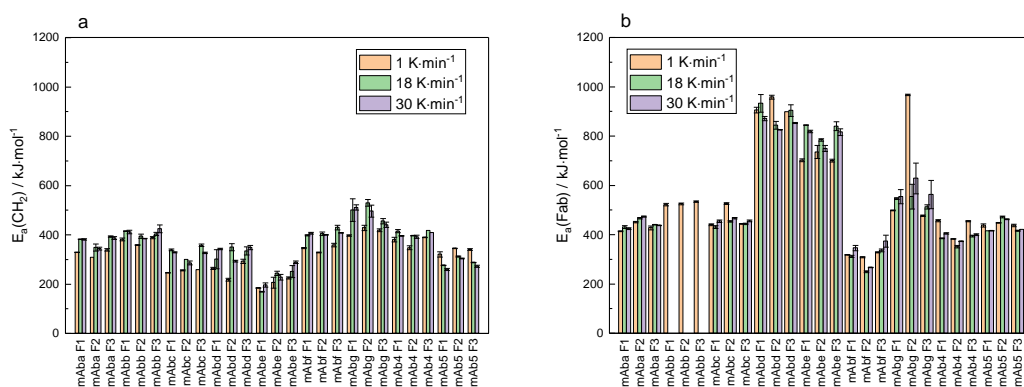


Fig. A.4.16: Activation energies of mAb a to mAb g, mAb 4 and mAb 5 in F1, F2, and F3. The determined E_a values at $1 \text{ K} \cdot \text{min}^{-1}$, $18 \text{ K} \cdot \text{min}^{-1}$, and $30 \text{ K} \cdot \text{min}^{-1}$ are summarized for the CH_2 -domain (a) and the Fab transition (b).

By analyzing the different E_a values of all mAbs in Fig. A.4.16, an average deviation of 14 % between the values at $1 \text{ K} \cdot \text{min}^{-1}$ and $30 \text{ K} \cdot \text{min}^{-1}$ can be determined for the CH_2 -domain, while for the Fab a deviation of 9 % can be calculated. Therefore, the Fab shows lower deviation between E_a values at $1 \text{ K} \cdot \text{min}^{-1}$ and $30 \text{ K} \cdot \text{min}^{-1}$ than the CH_2 -domain, which could be explained by the overlay of reversible and irreversible reactions during unfolding. Thus, the larger deviations of the CH_2 -domain compared to the Fab substantiate the discussed remarks in the main part.

The investigated ANOVA parameters to investigate correlations between E_a values determined at slow and fast heating rates with thermal stability are summarized in Tab. A.4.7 for mAba to mAbg and mAb4 and in Tab. A.4.8 for the mAb10 variants.

Tab. A.4.7: Parameters derived from the linear regressions for mAba to mAbg and mAb4 in F1, F2, and F3 at 25 °C at slow and fast heating. Linear fits were applied to the plots shown in Fig. 4.9 (Chapter IV). For description, see caption of Tab. A.4.4.

Linear fit	Slope and standard error	R-square	F-value	Prob>F	Correlation (linear slope significantly <, =, or > 0)
$E_a(\text{CH}_2)$ vs. monomer (25 °C)					
- at 1 K·min ⁻¹	-100 ± 18	0.58	30	1.6·10⁻⁵	yes (<0)
- at 18 K·min ⁻¹	-96 ± 24	0.43	17	5.0·10⁻⁴	yes (<0)
- at 30 K·min ⁻¹	-95 ± 21	0.48	20	1.7·10⁻⁴	yes (<0)
$E_a(\text{CH}_2)$ vs. aggregate (25 °C)					
- at 1 K·min ⁻¹	-126 ± 17	0.70	52	3.1·10⁻⁷	yes (<0)
- at 18 K·min ⁻¹	-132 ± 22	0.61	35	6.4·10⁻⁶	yes (<0)
- at 30 K·min ⁻¹	-124 ± 20	0.63	37	3.7·10⁻⁶	yes (<0)
$E_a(\text{CH}_2)$ vs. monomer (40 °C)					
- at 1 K·min ⁻¹	-18 ± 6.1	0.28	8.5	7.9·10⁻³	yes (<0)
- at 18 K·min ⁻¹	-15 ± 7.4	0.16	4.2	5.2·10 ⁻²	no (=0)
- at 30 K·min ⁻¹	-14 ± 6.9	0.16	4.1	5.5·10 ⁻²	no (=0)
$E_a(\text{CH}_2)$ vs. aggregate (40 °C)					
- at 1 K·min ⁻¹	-49 ± 9.5	0.55	27	3.3·10⁻⁵	yes (<0)
- at 18 K·min ⁻¹	-48 ± 12	0.41	15	7.9·10⁻⁴	yes (<0)
- at 30 K·min ⁻¹	-47 ± 11	0.46	19	2.9·10⁻⁴	yes (<0)

Tab. A.4.8: Parameters derived from the linear regressions of the mAb10 variants in citrate buffer at 40 °C at slow and fast heating. Linear fits were applied to the plots shown in Fig. 4.10 (Chapter IV). For description, see caption of Tab. A.4.4.

Linear fit	Slope and standard error	R-square	F-value	Prob>F	Correlation (linear slope significantly <, =, or > 0)
E _a (CH ₂) vs. monomer (40 °C)					
- at 1 K·min ⁻¹	-24 ± 9.0	0.46	7.0	3.0·10⁻²	yes (<0)
- at 18 K·min ⁻¹	-29 ± 14	0.36	4.6	6.5·10 ⁻²	no (=0)
- at 30 K·min ⁻¹	-27 ± 13	0.36	4.5	6.6·10 ⁻²	no (=0)
E _a (CH ₂) vs. aggregate (40 °C)					
- at 1 K·min ⁻¹	-31 ± 10	0.53	9.0	1.7·10⁻²	yes (<0)
- at 18 K·min ⁻¹	-36 ± 17	0.36	4.6	6.5·10 ⁻²	no (=0)
- at 30 K·min ⁻¹	-35 ± 15	0.42	5.8	4.2·10⁻²	yes (<0)

Appendix of Chapter V

A.5.4 Results

For mAb1a, mAb1c, mAb1d, and mAb1e in citrate buffer, the remaining IF asymmetry plots and DSC thermograms as control are depicted in Fig. A.5.1.

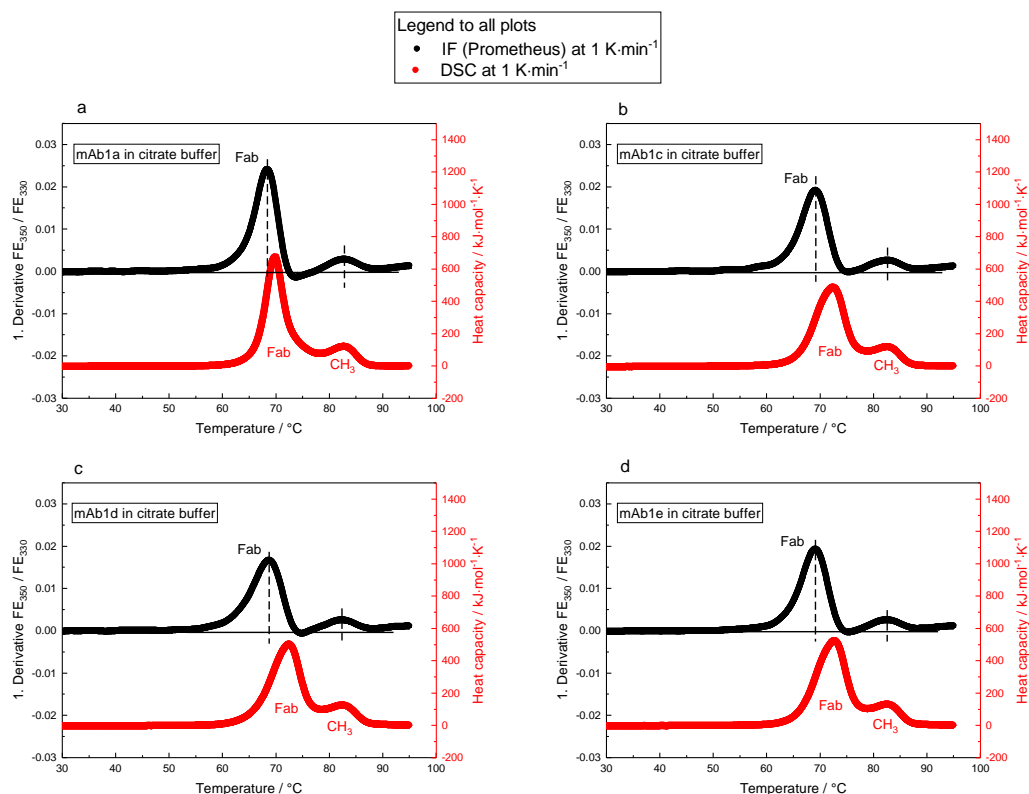


Fig. A.5.1: First derivative IF thermograms and DSC for mAb1a (a), mAb1c (b), mAb1d (c), and mAb1e (d) in citrate buffer. Mean and standard deviation of the first derivative of the FE_{350}/FE_{330} ratio as triplicate measurement is plotted against the temperature. The respective DSC thermogram as a duplicate is depicted as control. IF (Prometheus) and DSC thermograms are shown as an envelope-curve including the standard deviations. Asymmetries of the signals were determined according to the described procedure in Chapter V and is illustrated by a black solid line (baseline) and dashed line (signal maximum).

The heating rate dependent first derivative IF thermograms for mAb1a, mAb1c, mAb1d, and mAb1e in citrate buffer are shown in Fig. A.5.2.

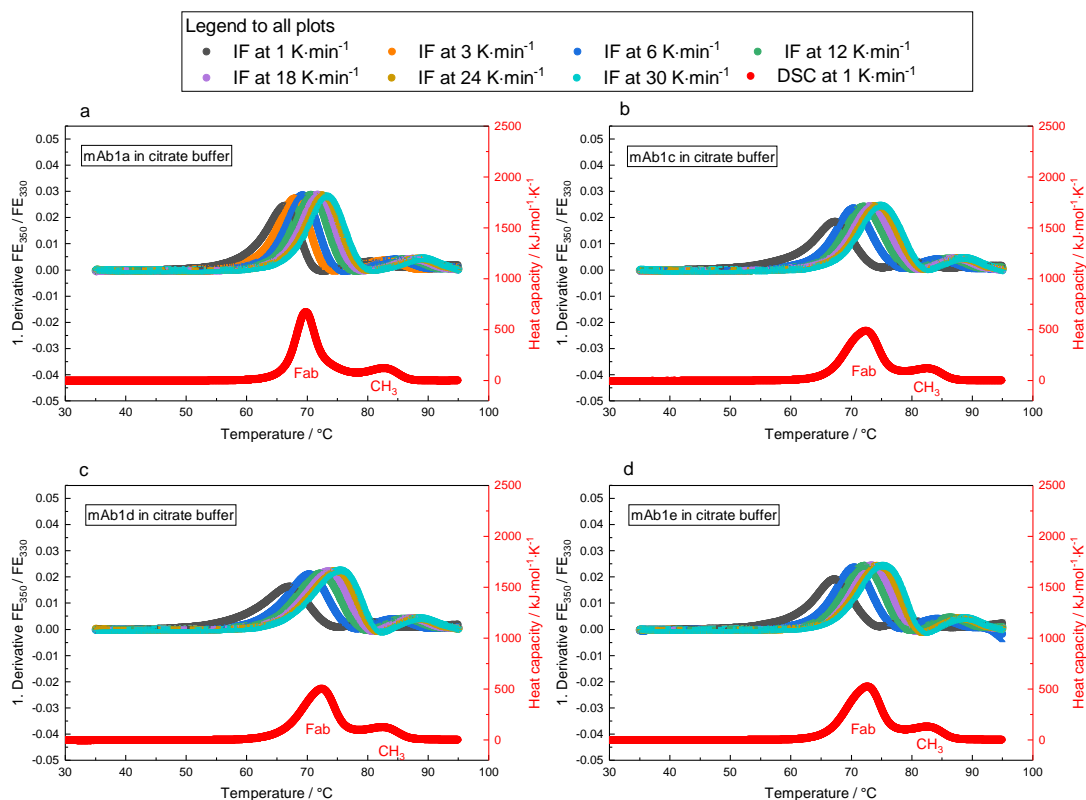


Fig. A.5.2: Heating rate dependent first derivative IF thermograms for mAb1a (a), mAb1c (b), mAb1d (c), and mAb1e (d) in citrate buffer. Heating rate dependent IF thermograms as mean and standard deviation of a duplicate spanning from 1 K·min⁻¹ to 30 K·min⁻¹ were recorded using the NES. The respective DSC thermogram as a duplicate is depicted as control. IF (NES) and DSC thermograms are shown as an envelope-curve including the standard deviations. The Fab can be assigned to the signal showing the largest increase in the amplitude, which is in this case the first transition for all four mAbs.

The plots showing the two novel methods to assign a certain IF transition to a mAb domain for all mAbs in formulation F1 can be found in Fig. A.5.3 to Fig. A.5.6.

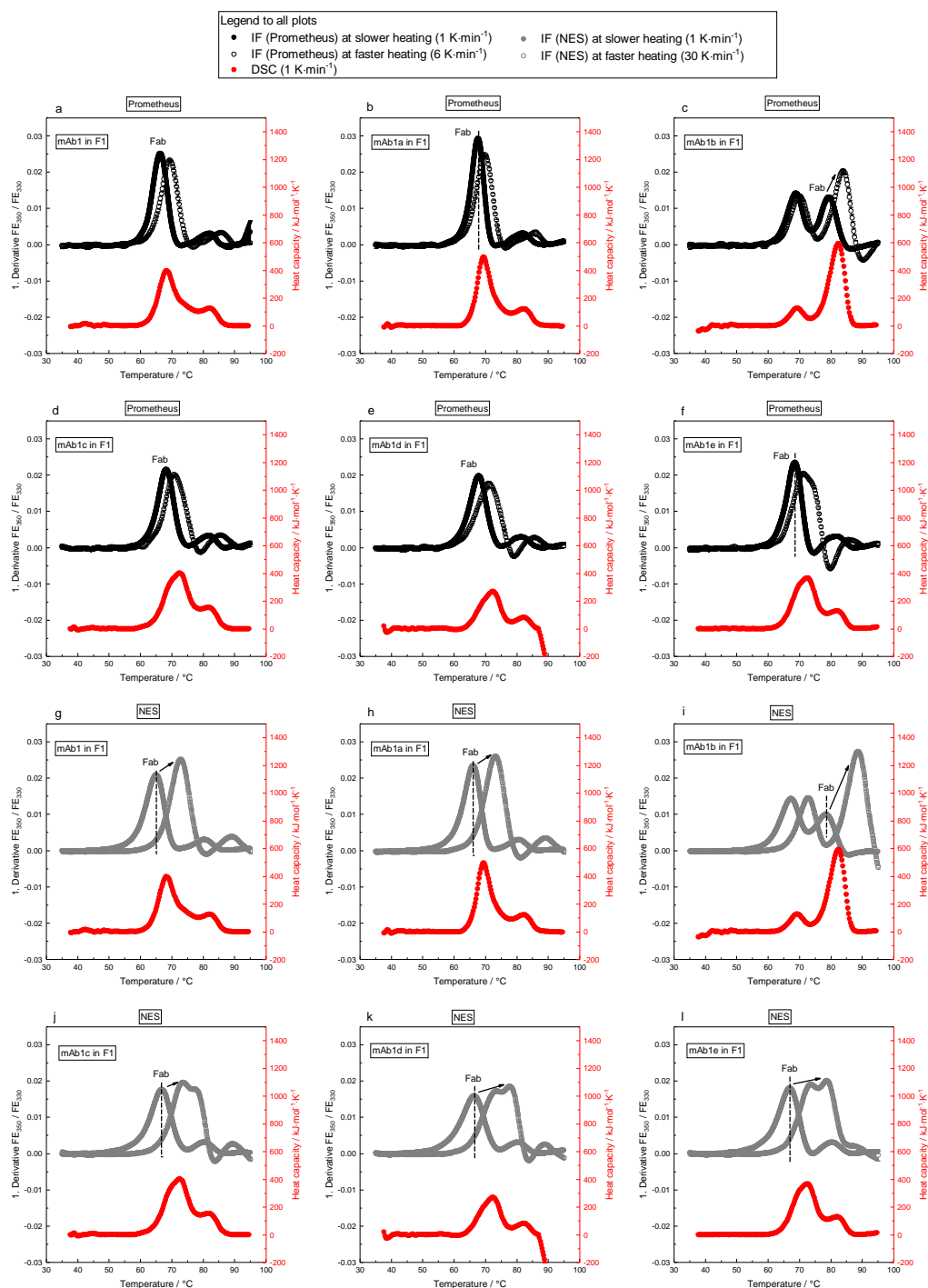


Fig. A.5.3: First derivative IF and DSC thermograms of the mAb1 variants in F1. To assign a certain IF transition to the Fab unfolding, the first derivative of the FE_{350}/FE_{330} ratio as mean and standard deviation of a duplicate is plotted against the temperature. IF thermograms, depicted as envelope-curve, are shown for the Prometheus instrument (black) and the NES (gray). The IF transition which refers to the Fab is marked with “Fab” (assigned by DSC). Asymmetries were determined as described in Chapter V and the transition showing a significantly more asymmetric signal is illustrated by a black dashed line. To assign the Fab according to heating rate dependent changes, a faster heating rate (open symbols) is plotted and compared to a slower rate (closed symbols). The signal showing a significantly increase in the amplitude to a faster heating rate is depicted by a black arrow. DSC thermograms as single measurement (red) are shown to verify the correct assignment according to the two novel established methods.

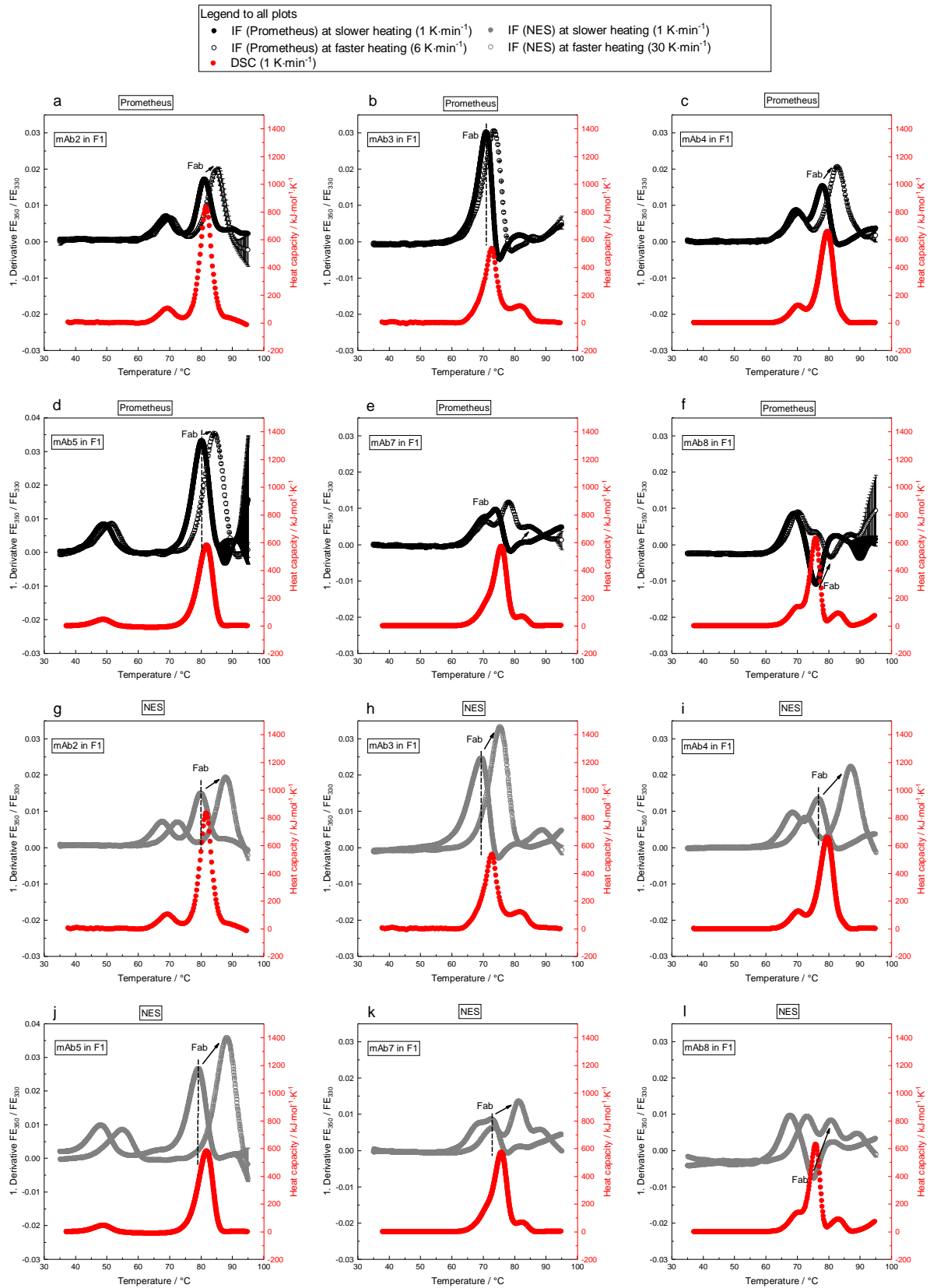


Fig. A.5.4: First derivative IF and DSC thermograms of mAb2 to mAb8 in F1. Description according to the caption of Fig. A.5.3.

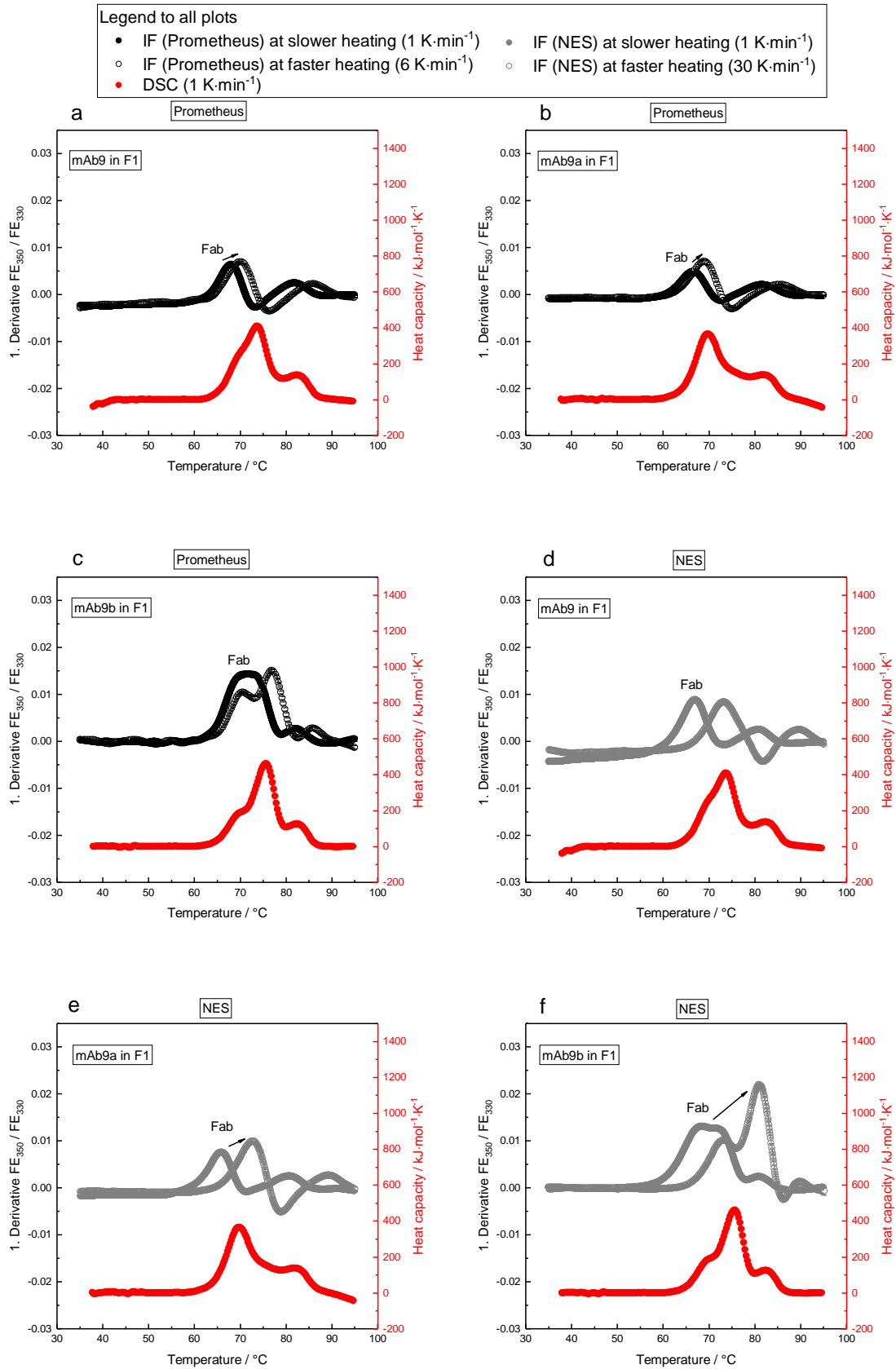


Fig. A.5.5: First derivative IF and DSC thermograms of the mAb9 variants in F1. Description according to the caption of Fig. A.5.3.

Legends to all plots

- IF (Prometheus) at slower heating (1 K·min⁻¹)
- IF (Prometheus) at faster heating (6 K·min⁻¹)
- IF (NES) at slower heating (1 K·min⁻¹)
- IF (NES) at faster heating (30 K·min⁻¹)
- DSC (1 K·min⁻¹)

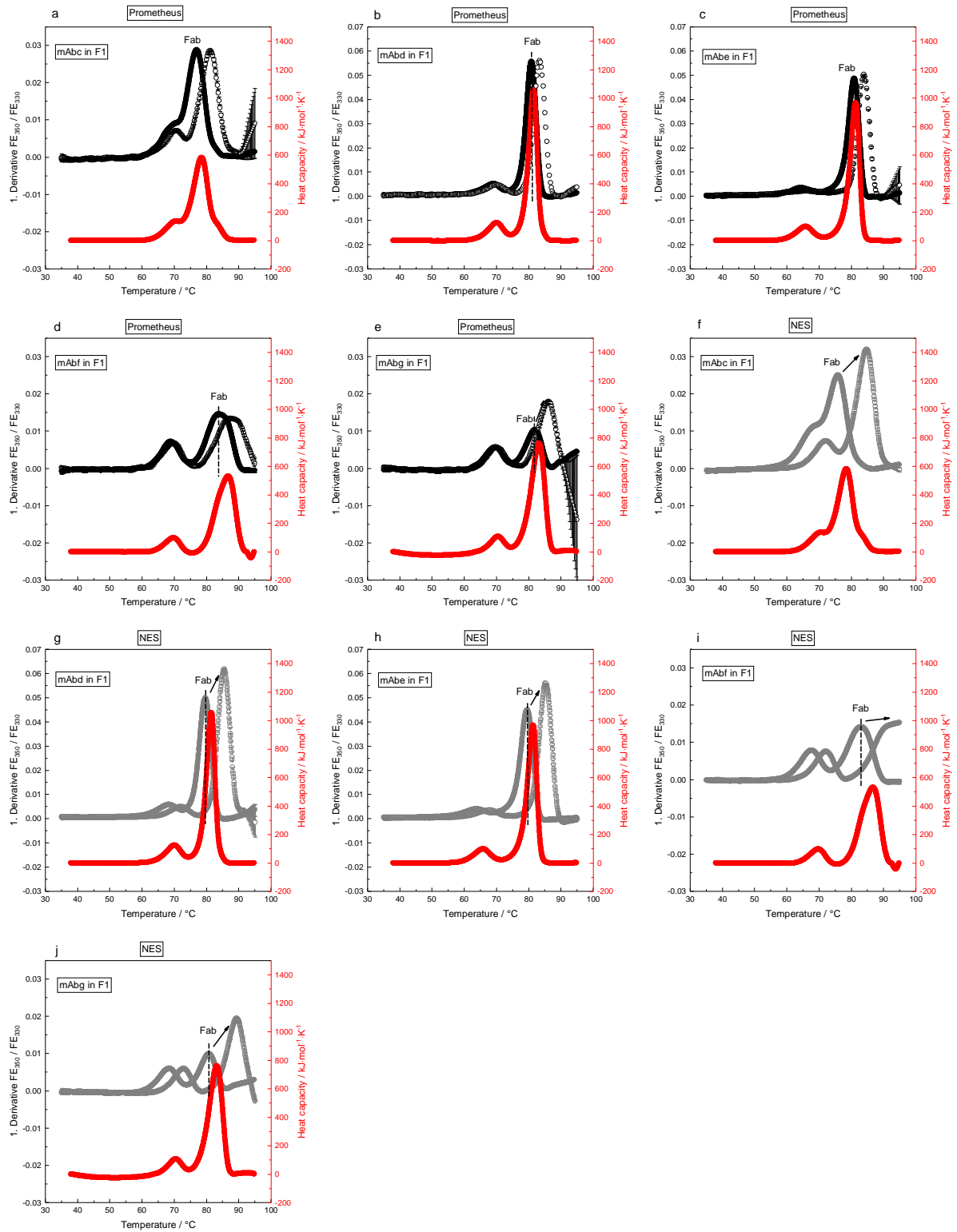


Fig. A.5.6: First derivative IF and DSC thermograms of mAbc to mAbg in F1. Description according to the caption of Fig. A.5.3.

Lebenslauf

Persönliche Daten:

Name: Richard Melien (geb. Weber)
Geburtsdatum/Ort: 27.07.1990, Fulda
Staatszugehörigkeit: Deutsch
Familienstatus: Verheiratet

Studium:

11.06.2021 Verteidigung der Doktorarbeit
27.01.2021 Einreichung der Doktorarbeit
06/2017 – 11/2020 Doktorand der Martin-Luther-Universität Halle-Wittenberg mit Vor-Ort-Einsatz bei Boehringer Ingelheim am Standort Biberach in der Abteilung „Pharmaceutical Development Biologicals“
04/2014 – 08/2016 Master of Science Biomedizinische Chemie an der Johannes-Gutenberg-Universität Mainz
10/2010 – 09/2014 Bachelor of Science Biomedizinische Chemie an der Johannes-Gutenberg-Universität Mainz

Schule:

2001 – 2010 Allgemeine Hochschulreife an der Rabanus-Maurus Schule Fulda

Publikationen:

Submitted for publication: R. Melien, N. Tschammer, D. Hinderberger, P. Garidel, M. Blech „Thermodynamics and Kinetics: Expansion of the Toolbox for predictive Parameters describing Antibody Stability“.

R. Melien, P. Garidel, D. Hinderberger, M. Blech "Thermodynamic Unfolding and Aggregation Fingerprints of Monoclonal Antibodies Using Thermal Profiling." *Pharmaceutical research* 37.4 (2020): 78.

Konferenzen:

Vortrag: Engineering Conferences International (ECI): Biological and Pharmaceutical Complex Fluids III (2019)

Poster: Jahrestagung der dt. Gesellschaft für Physikalische Chemie (2018, 2019)

Poster: Jahrestagung der dt. Pharmazeutischen Gesellschaft (2018)

Preise:

GDCh-Abiturientenpreis für die jahrgangsbesten Leistungen im Fach Chemie

Physikschulpreis der Deutschen Physikalischen Gesellschaft

(Ort, Datum)

(Unterschrift)